Constrained and Spectral-Spatial RF Pulse Design for Magnetic Resonance Imaging

by

Sydney Nicole Williams

A dissertation submitted in partial fulfillment
of the requirements for the degree of
Doctor of Philosophy
(Biomedical Engineering)
in the University of Michigan
2018

Doctoral Committee:

Professor Jeffrey A. Fessler, Co-Chair
Professor Douglas C. Noll, Co-Chair
Professor Thomas L. Chenevert
Associate Research Scientist Jon-Fredrik Nielsen
Associate Research Scientist Scott D. Swanson

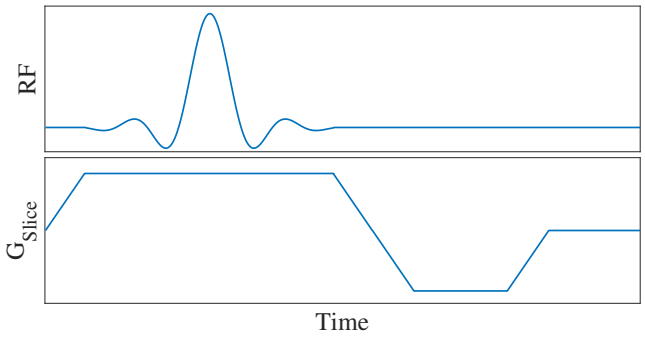
RF
G
Slice
Time

Sydney Nicole Williams

sydneynw@umich.edu

ORCID iD: 0000-0001-9979-6245

To Mom, Dad, Taylor, and Adal.

Acknowledgments

I am eternally grateful of the support I have received from my Ph.D. advisors Doug Noll and Jeff Fessler. I feel very lucky, not only did I have one, but *two* great mentors that pair perfectly in advising styles. I admire Jeff's analytical mind, attention to detail, and need to understand the mechanism of any quanderies I've encountered with my work. I think this mentality of taking time to do things well (instead of quickly, with mistakes) has been a very important lesson that I've been taught and continue to learn from him. Meanwhile, I know that any MRI physics question is no match for Doug's expertise. He has a very eloquent way of describing concepts and has excellent intution in the field. As I keep learning and researching, I hope some day to have even half the amount of vast MRI knowledge Doug has. Both Jeff and Doug have challenged me and guided me during my time in the Ph.D. program. They were never overbearing, always understanding and supportive. They shaped me into the researcher I am today and I cannot thank them enough. I look forward to remaining close colleagues with them throughout my career.

I also need to thank my other committee members who have helped make this dissertation possible. Tom Chenevert, from the Radiology Department, provides useful clinical insight to my work that sometimes is overlooked from the engineering perspective. Scott Swanson has incredible knowledge in MRI from a chemistry background and enriches my own understanding of my work through his thoughtful comments and questions. Jon-Fredrik Nielsen has been a key person in my Ph.D.; I work with him very closely on all experiments and he was the one who taught me how to use and program the lab MRI scanner. I feel like I can go to him for advice on everything from experimental, technical, to big-picture questions with my work. In my mind, I always think Jon is somewhat of an unofficial "third" advisor for me and I am so glad for that. In general I would say that not only am I fortunate to have great working relationships with all of my committee, but outside of that they are just good, kind people.

Other members of the fMRI lab have also shaped my Ph.D. dramatically. Scott Peltier is very helpful with scanning and lab protocol questions and has a approachable demeanor. Luis Hernandez-Garcia has an inquisitive personality and is a good listener. Many weekends I've been in lab struggling with something and Luis is often around to listen and help troubleshoot. Outside of lab work, Luis is also a great running mate and friend. The fMRI lab graduate students have made my research possible. Older members (Yash Shah, Dan Weller, Hao Sun, Alan Chu, Steven Allen, Matt Muckley, Gopal Nataraj, Mai Le, Kathleen Ropella) have been super encouraging and set foundations for my work. Hao Sun was particularly helpful with getting me started with research on RF pulse design and I based a lot of my work on his. My current labmates (Jonas Schollenberger, Tianrui Luo, Michelle Karker, Anish Lahiri, Shouchang Guo, Amos Cao) and I always provide help to one another and make the lab environment fun. In the fMRI Lab we have additional staff that help support the work that we do, and would also like to give special thanks to Ryan Smith, Barb Hibbard, Krisanne Litinas, and Chuck Nicholas.

The biomedical engineering (BME) department has been a welcoming home for me throughout my Ph.D. I have had a great time serving on the Graduate Student Council (GSC) and have made good friends with fellow organization members. Maria Steele, our BME Graduate Program Coordinator and GSC staff mentor, is incredibly organized, warm, and eager to help with all things department related. I am going to miss the sense of community the BME department has given me.

Quoting Ringo Starr, my Ph.D. could only be possible "with a little help from my friends." I've been fortunate to foster lifelong friendships from my youth in the small town of Morro Bay, California and maintain great relationships from undergrad at the Illinois Institute of Technology in Chicago. Moreover, I am especially grateful for the friends I've made in Ann Arbor, who have kept me sane through the challenges of my PhD. Rachel Surowiec, Fede Cuomo, Mariana Masteling, Jack Benson, Dan Clough, Nidhi Maley, Paige Castle, Matt Muckley, John Pitre, Sriram Vaidyanathan, Janki Patel, Jonas Schollenberger, Diana Dillstrom, Buke Hiziroglu, and many more...thank you all so much for your friendship and I am looking forward to future years knowing you ahead.

And of course, at the end of the day, I will always be thankful to my family. My parents have been incredibly supportive throughout my academic pursuit and are still my number one fans. My younger brother, Taylor, has such a pure and noble personality and is truly my role model. I can't wait to see him marry his high school sweetheart, Erika. My aunts, uncles, cousins, and grandparents always have provided me with love and encouragement that I could never take for granted. My husband's family brought me in immediately as one of their own, giving me a profound feeling of acceptance and love. Finally, my husband,

Adalberto, has been there through every single step of grad school. He's praised me through my triumphs and been the pillow to catch me when I've fallen to missteps. It has been a *hard* five years living apart from him. It's a beautiful thing to celebrate this accomplishment with him and to know we will finally be together.

Thank you all, from the bottom of my heart.

TABLE OF CONTENTS

LIST OF FIGURES

LIST OF TABLES

LIST OF APPENDICES

LIST OF ALGORITHMS

LIST OF ABBREVIATIONS

MRI Magnetic Resonance Imaging

RF Radio Frequency

STA Small-Tip Angle

LTA Large-Tip Angle

QPWLS Quadratic Penalized Weighted Least-Squares

FISTA Fast Iterative Shrinkage-Thresholding Algorithm

SMS Simultaneous Multislice

MB Multiband

RMSE Root Mean Squared Error

NRMSE Normalized Root Mean Squared Error

SLR Shinnar Le-Roux

OC Optimal Control

STFR Small-Tip Fast Recovery

SPGR Spoiled Gradient Recalled Acquisition

bSSFP Balanced Steady-State Free Precession

FOV Field of View

pTx Parallel Transmit

SAR Specific Absorption Rate

ABSTRACT

Magnetic Resonance Imaging (MRI) provides a non-invasive glimpse inside the human body, generates excellent soft tissue contrast, uses non-ionizing radiation, and has become a critical tool in diagnosis of disease in medicine. Radio Frequency (RF) pulses are an integral component of MRI pulse sequences and can be tailored to particular applications. This dissertation explores the MRI physics, convex optimization problems, and experimental methodologies required for the design of tailored RF pulses

First, we introduce constrained RF pulse design, a process that incorporates meaningful, physical constraints, such as peak RF amplitude and integrated RF power, and enables efficient RF pulse design. With this process we explore simultaneous multislice (SMS) imaging, a method used to accelerate MRI and combat notoriously long acquisition times. Compared to an SMS pulse designed without constraints, our constrained pulses achieved lower magnitude normalized root mean squared error (NRMSE) for an equivalent RF pulse length, or alternatively, the same NRMSE for a shorter pulse length. Constrained RF pulse design forms a basis for the rest of the dissertation.

Second, we show that prewinding pulses, a special class of RF pulses, help reduce signal loss due to intravoxel dephasing generated by magnetic field inhomogeneities. We propose a spectral-spatial prewinding pulse that leverages a larger effective recovery bandwidth than equivalent, purely spectral pulses. In an in vivo experiment imaging the brain of a human volunteer, we designed spectral-spatial pulses with a complex NRMSE of 0.18, which is significantly improved from the complex NRMSE of 0.54 in the purely spectral pulse for the same experiment.

Finally, we consider a slab-selective prewinding pulse, that extends spectral and spectral-spatial prewinding pulses to a common 3D imaging method. Here we integrate optimal control optimization to further improve the slab-selective spectral pulse design and see an in vivo improvement of excitation NRMSE from 0.40 to 0.37. In the context of a steady-state sequence small-tip fast recovery (STFR), we also show a major reduction in mean residual transverse magnetization magnitude after the STFR "tip-up" recovery pulse from 0.18 to 0.02 when adding optimal control. This method has the potential to connect prewinding pulse design from the MRI physicist engineering workspace to a clinical application.

In summary, we show that constrained RF pulse design provides an efficient way of improving MRI in terms of acquisition speed (via multislice imaging) and image quality (via signal recovery).

CHAPTER 1

Introduction

1.1 Motivation

MRI is a powerful medical diagnostic tool offering a noninvasive glimpse inside the human body. The excitation component during an MRI pulse sequence is comprised of RF pulses and sometimes excitation gradients. RF excitation plays a critical role in the contrast and quality of the image acquired. Tailored RF pulse design schemes can compensate for magnetic field (B0) inhomogeneity, avoiding signal loss at highly off-resonant locations [1], [2], [3], [4] [5], and the pulses can also be incorporated into steady-state sequences for fast imaging [6], [7], [8], [9] such as Balanced Steady-State Free Precession (bSSFP) and Small-Tip Fast Recovery (STFR). These techniques provide fast, high signal images with combined T2/T1 contrast and have have important clinical applications including cardiac MRI [10], abdominal MRI [11], and even recently functional MRI (fMRI) [12]. This dissertation presents tailored RF pulse design with explicit individual patient and hardware constraints of the MRI scanner. The pulse designs looked at simultaneous multislice imaging as well as multidimensional, spectral and spectral-spatial pulses for steady-state imaging in STFR.

1.2 Outline and Contributions

The rest of this dissertation is divided as follows: the Background Chapter 2 that reviews important MRI and optimization concepts for this thesis, the Constrained RF Pulse Design Applied to Simultaneous Multislice (SMS) Imaging Chapter 3, the 2D Spectral-Spatial Prewinding Pulse Chapter 4, the Spectral Slab-Selective Prewinding Pulse Chapter 5, and a Future Works Chapter 6. There are also four appendices, Appendix A providing additional info for Chapter 4, Appendix B providing additional info for Chapter 5, Appendix C providing an extension of both Chapters 4 and 5, and Appendix D providing the reader with

step-by-step instructions for reproducing work in this thesis both in terms of programming and running experiments on the MRI scanner.

Each of the Body Chapters (3,4, 5) introduce novel contributions to the field. The introduction of constrained RF pulses for simultaneous multislice efficiently designed pulses with physically meaningful constraints (peak RF amplitude and integrated RF power). Chapter 3 also re-framed the pulse design problem to minimize out-of-slice excitation with set in-slice error constraints. This work was presented at two international conferences (ISMRM 2017, ESMRMB) [13], [14]. Chapter 4 expands spectral prewinding pulses [15] to a 2D spectral-spatial pulse that acheives better rephasing of intravoxel spins. This work was published in *Magnetic Resonance in Medicine* [9] and stemmed from an abstract receiving the Magna Cum Laude Presenter's Award at the 2015 ISMSRM meeting [16]. Chapter 5 expands spectral prewinding pulses to slab-selection, was a part of work presented as an oral presentation at the 2018 ISMRM meeting [17], and is in preparation for submission to *Magnetic Resonance in Medicine*.

CHAPTER 2

Background

2.1 MRI Physics

Magnetic resonance imaging operates on the property of nuclear magnetic resonance, in which atoms with an odd number of protons and/or neutrons, or "spins", exhibit a magnetic moment that can interact with external magnetic fields. For imaging in the body, the high water content of biological tissues gives rise to many hydrogen ^{1}H protons that are well-suited for MRI [18]. This property makes MR an excellent tool for non-invasive, non-ionizing imaging within the body that has notable contrast between soft-tissues.

2.1.1 Three Electromagnetic Fields

MRI uses three major electromagnetic field components that, in conjunction, produce a spatially-localized signal that can be reconstructed and interpreted into an image. Figure 2.1 shows the three field components within a typical MRI scanner.

First, the main magnetic field (B0) aligns the magnetic moment of the hydrogen spins in parallel to the direction of the field at the Larmor resonance frequency, ω. The B0 field direction is often called the longitudinal or z dimension. In modern clinical practice, the B0 field is typically 1.5 or 3 Tesla (in perspective, the earth's magnetic field is 25-65 μT or 0.25-0.65 Gauss [19]), although higher field strengths are becoming more common.

Secondly, an RF transmit pulse ($B1^+$) is applied perpendicularly to B0. The RF pulse tilts the magnetization by a particular flip angle into the xy or transverse plane where it precesses, eventually recovering to its initial direction parallel to B0. This precession induces current in an RF receive coil ($B1^-$) that is recorded as the MR signal. The B1 field is much smaller than B0, typically < 0.2 Gauss.

Finally, linear gradient fields (G_x, G_y, G_z) induce spatially varying field strengths that allow for localization of the MR signal in 3D space. These fields have typical upper lim-

its of 5 G/cm, although for specific applications gradients could be much higher, but still significantly smaller than B0.

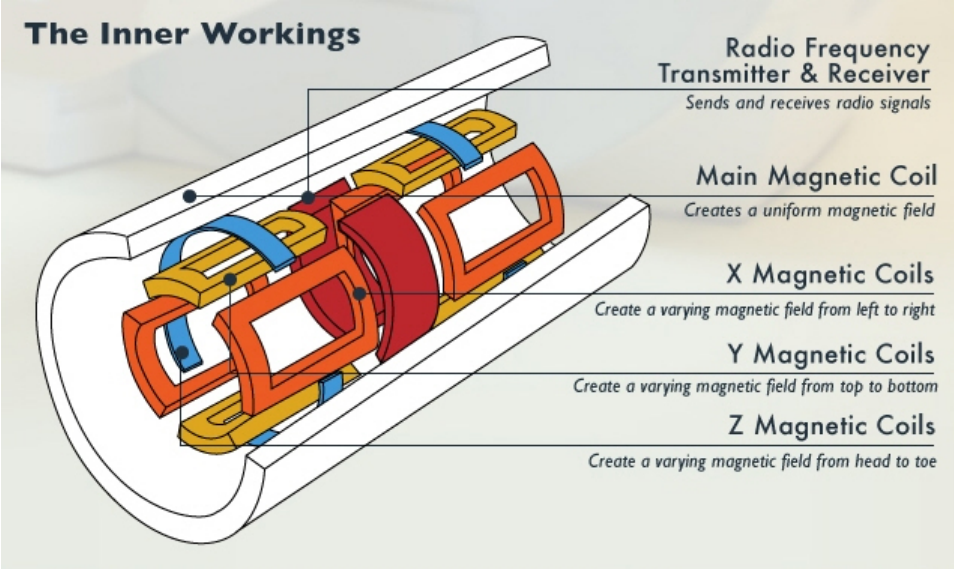

Figure 2.1: The inner electromagnetic components that generate and MR image. The main magnetic field (B0) aligns hydrogen spins. The RF coil excites spins to cause precession. The gradient coils localize the signal in x, y, z space [1].

2.1.2 Relaxation

After spins are excited with an RF pulse, the longitudinal recovery time of the spins towards the z-direction is called the T1 relaxation time constant, while the time in which multiple nuclear spins spread along the xy-plane during precession is known as the T2 relaxation time constant (T2* when considering subvoxel inhomogeneity effects). Different tissues have unique hydrogen environments and associated T1 and T2 constants. By manipulating the pulse delivery in an image acquisition, images can be weighted to emphasize T1 or T2 contrasts [18]. Figure 2.2 shows an example of T1- vs. T2- weighted images in the brain.

1. Electronic Products https://www.electronicproducts.com/

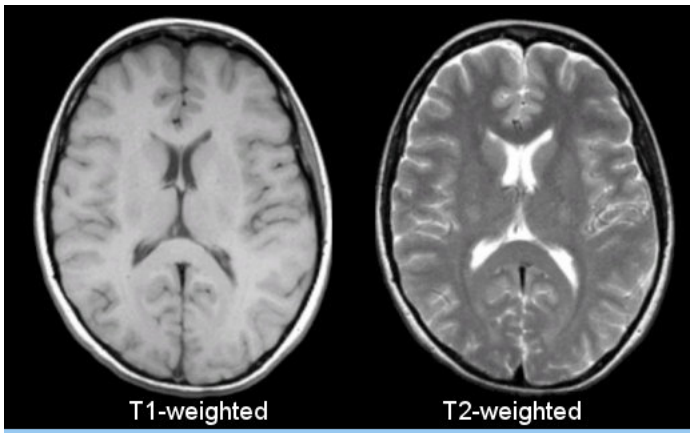

Figure 2.2: Comparison between two standard MR contrasts: T1- and T2- weighted[2].

2.1.3 Bloch Equation

After RF excitation (written in xy components as $B1 = B1_x + iB1_y$), the behavior of the magnetization within the main magnetic field and applied gradients $\mathbf{G} = [G_x \ ; G_y \ ; G_z]^T$, at each spatial location $\mathbf{r} = [x \ ; y \ ; z]^T$ are governed by the Bloch equation [20]:

$$\frac{d}{dt}\begin{pmatrix} M_x \\ M_y \\ M_z \end{pmatrix} = \begin{pmatrix} -\frac{1}{T_2} & \gamma\mathbf{G}\cdot\mathbf{r} + \Delta\omega & -\gamma B1_y \\ -\gamma\mathbf{G}\cdot\mathbf{r} + \Delta\omega & -\frac{1}{T_2} & \gamma B1_x \\ \gamma B1_y & -\gamma B_x & -\frac{1}{T_1} \end{pmatrix} \begin{pmatrix} M_x \\ M_y \\ M_z \end{pmatrix} + \begin{pmatrix} 0 \\ 0 \\ \frac{M_0}{T_1} \end{pmatrix} \tag{2.1}$$

where γ is the gyromagnetic ratio relating the Larmor frequency and magnetic field (ω=γB0), and $\Delta\omega$ is off-resonance attributed to inhomogeneity in B0. In certain circumstances, such as during a short, single RF pulse, it is convenient to ignore T1 and T2 relaxation and $\Delta\omega$, reducing the equation to:

$$\frac{d}{dt}\begin{pmatrix} M_x \\ M_y \\ M_z \end{pmatrix} \approx \begin{pmatrix} 0 & \gamma\mathbf{G}\cdot\mathbf{r} & -\gamma B1_y \\ -\gamma\mathbf{G}\cdot\mathbf{r} & 0 & \gamma B1_x \\ \gamma B1_y & -\gamma B_x & 0 \end{pmatrix} \begin{pmatrix} M_x \\ M_y \\ M_z \end{pmatrix} \tag{2.2}$$

2. Case Western Medicine http://casemed.case.edu/clerkships/neurology/NeurLrngObjectives/MRI.htm

2.2 RF Pulse Design

Radiofrequency pulse excitation is critical to MR imaging because the magnetization signal be detected only if a component lies in the transverse plane, perpendicular to the main magnetic field B0.

2.2.1 Common RF Pulse Types

Many classes of RF pulses exist for different applications, and here we will give a brief overview of these common types. The over-arching theme of this dissertation is RF pulse design, so having a fundamental understanding of various RF pulses is important.

The most generic pulse is the so-called *hard pulse*, that is simply a short, rectangular pulse. Hard pulses do not include any spatial gradients during excitation and globally excite spins within the imaging object over a large bandwidth [21]. Another important RF pulse type is the *slice-selective pulse*, that applies a linear gradient in the slice dimension to solely excite a particular slice (or slab). The classic example of this pulse is a truncated sinc pulse, which roughly excites a rectangular slice within the Fourier domain (where data is acquired). A standard slice-selective RF pulse/gradient waveform is shown on the cover page of this dissertation. A separate RF pulse type is a *refocusing pulse*, that aims to recover dephased spins that have already been excited to the transverse plane. These pulses typically have a flip angle of 180° and are a component of the "Spin Echo" sequence (described in subsequent Section 2.4.2). Similarly, *inversion pulses* also typically have a flip angle of 180° but instead "invert" the magnetization from the initial longitudinal position in z to the negative z axis

Additional, exotic RF pulses are common for MRI. For example, *adiabtic* RF pulses are a unique class of RF pulses that help mitigate effects of inhomogeneity in the $B1^+$ field [21]. Another special RF pulse type are *spectrally selective* pulses which include fat supression pulses and magnetization transfer pulses. This thesis also discusses a spectral and jointly spectral-spatial "prewinding" pulse (Chapters 4,5) that can used to recover signal loss due to T2* dephasing [15].

2.2.2 Small-Tip Angle Approximation

With the need for more sophisticated imaging schemes comes the need for RF pulses that are tailored to their applications. A simple method for modeling RF excitation can enable tailored pulse design, the Small-Tip Angle (STA) approximation [22] In 1989 John Pauly recognized the Fourier relationship between k-space and excitation. This approxima-

tion states, for a relatively small flip angle ($< 30°$, and reasonably $\leq 90°$), we can assume that longitudinal magnetization is roughly constant ($M_z \approx M_0$), and that transverse magnetization can be decoupled from M_z and expressed as $M_{xy} = M_x + iMy$. The STA approximation provides the critical relationship of small-tip angle design,

$$M_{xy}(\mathbf{r}, T) = iM_0(\mathbf{r}) \int_0^T \gamma B_1(t) e^{i\mathbf{k}(t)\cdot\mathbf{r}} dt \tag{2.3}$$

where

$$\mathbf{k}(t) = -\gamma \int_t^T \mathbf{G}(s) ds \tag{2.4}$$

defines the spatial frequency as provided by the gradient waveform during excitation, commonly referred to as "excitation k-space" [22]. With this Fourier relationship, an additional exponential term can be added to relate the frequency shift induced by off-resonance $\Delta\omega$ in space as [23]

$$M_{xy}(\mathbf{r}, T) = iM_0(\mathbf{r}) \int_0^T \gamma B_1(t) e^{i\mathbf{k}(t)\cdot\mathbf{r} + i\Delta\omega(\mathbf{r})[t-T]} dt \quad . \tag{2.5}$$

Here the initial magnetization M_0 is set as unit norm $[0,0,1]^T$ along B0. The small-tip angle approximation allows for discretized RF pulse design $\mathbf{b}$ to be placed into a matrix-vector model,

$$\mathbf{m} \approx M_0 \mathbf{A}\mathbf{b} \tag{2.6}$$

where $\mathbf{m}$ is vector containing the transverse magnetization M_{xy} at each location $\mathbf{r}$ and $\boldsymbol{A}$ is the system matrix derived from STA,

$$a_{i,j} = i\gamma e^{i\mathbf{k}(t_j)\cdot\mathbf{r}_i + i\Delta\omega(\mathbf{r}_i)[t_j - T]} \Delta t \quad . \tag{2.7}$$

The linear STA matrix-vector model is useful for designing RF pulses through least-squares design problems that are outlined in Section 2.3.

2.2.3 Bloch Spin-Domain for Large-Tip Angles

The STA approximation is effective and useful for many RF pulse design problems, although it is insufficient for Large-Tip Angle (LTA) pulses (which are pulses greater than 90°) because the linear Fourier relationship of the transverse magnetization breaks down. One way of addressing LTA design is by casting the standard Bloch equation with ignored

relaxation (2.2) into the "Spin-Domain" [24] which expresses magnetization after exciation as

$$\frac{d}{dt}\begin{pmatrix}\beta\\ \alpha^*\end{pmatrix} = \frac{i\gamma}{2}\begin{pmatrix}\mathbf{G}\cdot\mathbf{r} & B1^*\\ B1 & -\mathbf{G}\cdot\mathbf{r}\end{pmatrix}\begin{pmatrix}\beta\\ \alpha^*\end{pmatrix} \tag{2.8}$$

where α and β are the Cayley-Klein parameters, which characterize an orientation of spins in a 2x2 matrix that has close relation to quarternions [25]. The 3x3 magnetization in terms of Spin-Domain parameters is

$$\begin{pmatrix}M_{xy}^{+}\\ M_{xy}^{+*}\\ M_z^{+}\end{pmatrix} = \begin{pmatrix}(\alpha^*)^2 & -(\beta^*)^2 & -2\alpha^*\beta^*\\ -\beta^2 & \alpha^2 & -2\alpha\beta\\ \alpha^*\beta & \alpha\beta^* & \alpha\alpha^* - \beta\beta^*\end{pmatrix}\begin{pmatrix}M_{xy}^{-}\\ M_{xy}^{-*}\\ M_z^{-}\end{pmatrix} \quad . \tag{2.9}$$

For an axis **n**=[0,-1,0]^T rotated about an angle ϕ the Cayley-Klein parameters are written as [24]

$$\alpha = \cos(\frac{\phi}{2}) - in_z\sin(\frac{\phi}{2}) \tag{2.10}$$

and

$$\beta = -i(n_x + in_y)\sin(\frac{\phi}{2}) \quad . \tag{2.11}$$

These parameters then simplify to $\alpha = \cos(\frac{\phi}{2})$ and $\beta = \sin(\frac{\phi}{2})$ [26]. It can also be useful to consider the case of rotation along a complex plane (excitation with RF phase), for example **n**=[$\cos\psi$, $\sin\psi$, 0]^T which yields $\alpha = \cos(\frac{\phi}{2})$ and $\beta = -ie^{i\psi}\sin(\frac{\phi}{2})$.

The Bloch Spin-Domain helps LTA by providing a quick way of solving for the magnetization compared to the conventional Bloch equation simulation (2.2). This is critical because for large flip angles, the linearity of the STA approximation fails, yet full simulation with the standard Bloch equation would be more expensive for online pulse design. In this thesis (particularly, Chapter 5), we design pulses in the Bloch Spin-Domain through an optimal control approach [27] that interleaves Spin-Domain evaulations and iterative RF perturbation updates, as decribed in Ref. [28].

2.3 Least Squares Optimization

Under the STA regime, the linear Fourier relationship between excitation and transverse magnetization permits the design of RF pulses through least-squares optimization. For a given target magnetization pattern **d** with associated STA matrix **A**, an RF pulse $\widehat{\mathbf{b}}$ is solved

for through the following optimization [1],

$$\widehat{\mathbf{b}} = \underset{\mathbf{b}}{\operatorname{argmin}} \ ||\mathbf{Ab} - \mathbf{d}||_2^2 \ . \tag{2.12}$$

2.3.1 Regularization and Weights

As is common for inverse problems, a regularization or penalty term is typically considered for the RF pulse design problem. The most common type of regularization is Tikhonov Regularization, which balances excitation accuracy in the data fidelty term and RF power via an ℓ_2-norm [1]. Additionally, least-squares RF pulse optimization can be improved by introducing a diagonal weighting matrix $\mathbf{W}$ that seeks to exclude "don't care" regions of the design space. For example, in a 2D spatial excitation pattern within the brain, $\mathbf{W}$ might be zero for all values in the image background outside of the brain, since any spurious RF in this region would not excite anything. Therefore, the classic RF pulse design problem is typically written

$$\widehat{\mathbf{b}} = \underset{\mathbf{b}}{\operatorname{argmin}} \ ||\mathbf{Ab} - \mathbf{d}||_{\mathbf{W}}^2 + \beta||\mathbf{b}||_2^2 \ . \tag{2.13}$$

Here, the term β is the regularization parameter, and must be tuned for each pulse design setup. For small design problems, a closed-form solution exists,

$$\widehat{\mathbf{b}} = (\mathbf{A}^{\mathrm{T}}\mathbf{W}\mathbf{A} + \beta\mathbf{I})^{-1}\mathbf{A}^{\mathrm{T}}\mathbf{W}\mathbf{d} \ . \tag{2.14}$$

For larger problems, iterative algorithms (2.3.3) are used.

2.3.2 Constraints

Constrained least-squares pulse design differs from regularized formulations in that the penalty term is replaced by a set of physical constraints. This problem is written as

$$\begin{aligned} \widehat{\mathbf{b}} = \underset{\mathbf{b}}{\operatorname{argmin}} \ & ||\mathbf{Ab} - \mathbf{d}||_{\mathbf{W}}^2 \\ \text{s.t.} \ & \ g(b) = 0 \\ \text{and} \ & \ h(b) \leq \text{constraints} \end{aligned} \tag{2.15}$$

where $g(b)$ are equality constraints and $h(b)$ are inequality constraints. In this thesis, we pose constrained RF pulse design problems with convex inequality constraints. To solve these problems, there is no analgous closed-form solution, so more sophisticated algorithms

are required. The main advantage to constrained pulse design is that no tuning parameters are required, which is further motivated in Chapter 3.

2.3.3 Algorithms and Solvers

Here we discuss just a few methods for designing the types of RF pulses presented in this disseration, although the list is not exhaustive. Ref [29] Chapter 11 outlines many more algorithms. For Quadratic Penalized Weighted Least-Squares (QPWLS) pulse design problems such as Eq. (2.13), the conjugate-gradient algorithm [30] is an efficient, popular approach for solving. In this technique, the RF pulse is iteratively updated until a stopping criterion has been met (related to norm of design error or gradient) or a certain number of iterations has finished [31].

In the case of a constrained weighted least-squares design problem as in Eq. (2.15), other approaches might be taken. For optimization with a single, convex constraint, the Fast Iterative Shrinkage-Thresholding Algorithm (FISTA) is an effective method [32]. Similar to the conjugate-gradient method, FISTA iteratively updates until the stopping criterion (norm design error, number of iterations) is met. When using FISTA, an informed initialization reduces the number of iterations for convergence. A common way of initializing FISTA is to use a pulse designed with a few iterations of an un-regularized conjugate gradient algorithm. FISTA requires two additional steps for implementation compared to conjugate gradient. First, an estimate of the gradient step size must be chosen. A reasonable step size is less than or equal to the 1 over the Lipschitz constant, or 1 divided by the maximum Eigenvalue of the Hessian matrix [29]. To quickly obtain this estimate, the Power Iteration Method [33] is used. Secondly, the convex constraint must be cast into a proximal operator for the proximal step of FISTA. For example the ℓ_2-norm constraint $||\mathbf{b}||_2 \leq C$, for positive constant C, the proximal operator is

$$\frac{\mathbf{b}}{\max(\frac{||\mathbf{b}||_2}{C}, 1)} \tag{2.16}$$

and for an ℓ_∞-norm constraint, $||\mathbf{b}||_\infty \leq C$, the operator is

$$\min(|\mathbf{b}|, C)\mathrm{e}^{i\angle\mathbf{b}} \quad . \tag{2.17}$$

Combining proximal operators for multiple convex constraints is less clear, although some recent methods exist [34]. For this dissertation, mutliple constraints were handled in Chapter 3 with a readily available convex optimization software, CVX [35]. Although CVX is relatively quick and simple to use, two drawbacks are that it does not support com-

plex numbers and that it cannot handle large, mutlidimensional designs.

This dissertation does not explore many additional iterative algorithms for constrained RF pulse design, although future work could include more specialized techniques. A natural next step would be to use the popular alternating direction method of multipliers algorithm (ADMM) [36] which could handle multiple convex constraints. However, ADMM introduces tuning parameters that affects its convergence rate.

2.4 MRI Pulse Sequences

One final piece of background information for this dissertation is the description of a few relevant MRI pulse sequences. Pulse sequences are sets of RF pulses, gradient waveforms, and data acquisition that enable and MR image to be created.

2.4.1 Standard Gradient Echo

The gradient echo sequence is a fundamental MR imaging sequence comprising of a single RF excitation and a gradient reversal in the frequency encoding direction that generates an echo acquired data readout [21]. Figure 2.3 shows the pulse sequence diagram for a gradient echo. Gradient echoes are widely used for their speed, but are sensitive to T2* (instead of T2) which can cause signal loss to inhomogeneity but also be useful in the case of functional MRI.

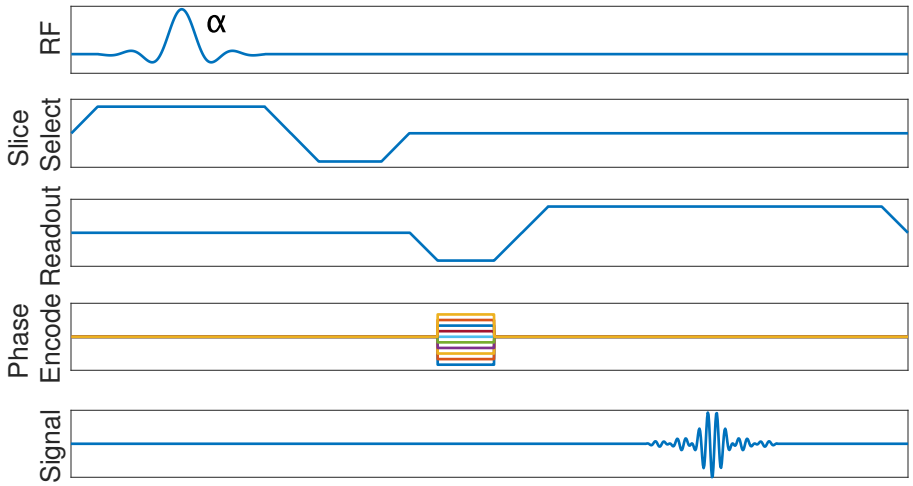

Figure 2.3: Gradient echo pulse sequence diagram

2.4.2 Standard Spin Echo

Spin echo sequences are another common MR sequence. In this case, a 90° excitation-180° refocusing RF pulse pair causes intravoxel spins to rephase at the echo time (showin in Figure 2.4) Spin echoes therefore have less sensitivity to T2* and field inhomogeneity as gradient echoes, but also are generally much slower sequences. A classic use of spin echoes is in diffusion imaging, and advancements in terms of fast spin echo and multi-echo sequences have made spin echo sequences an integral part of clinical practice.

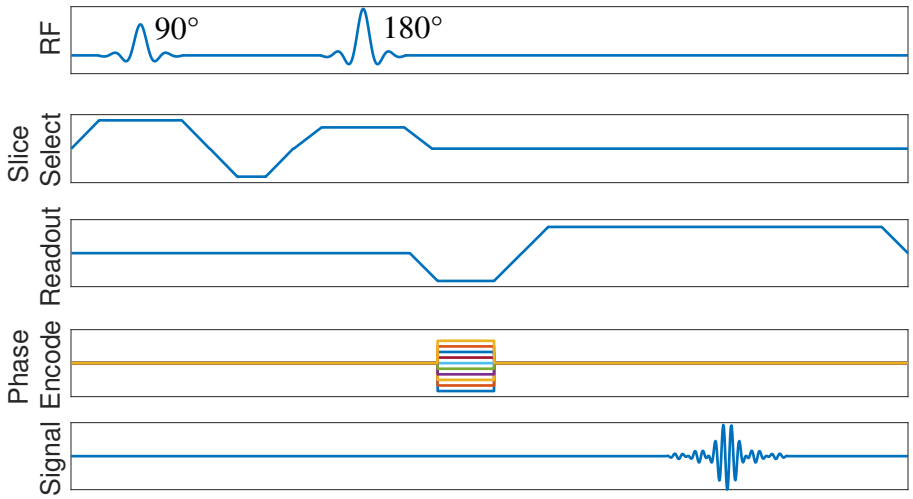

Figure 2.4: Spin echo pulse sequence diagram

2.4.3 Spoiled Gradient Recalled Acquisition in the Steady-State

A special class of gradient echo sequences is steady-state sequences which are most notable for their speed. In these sequences, the longitudinal and transverse magnetization eventually reach a non-zero steady-state after many transient TR's [37]. A simple steady-state sequence is Spoiled Gradient Recalled Acquisition (SPGR) (also known as T1-FFE or FLASH). SPGR is called a "spoiled" sequence, which in this case refers to "RF spoiling" or phase cycling of the RF pulse after each TR to eliminate all residual transverse magnetization before the next TR. This is in contrast to "gradient spoiling" which dephases transverse magnetization with a gradient "crusher". While SPGR is most notable for T1-weighted imaging, it is possible to adjust acquisition parameters for other image contrasts.

2.4.4 Small-tip Fast Recovery

Small-tip Fast Recovery (STFR) is a new, experimental sequence proposed by our group at the University of Michigan [6]. This dissertation discusses the STFR sequence extensively (notably, Chapters 4 and 5). STFR is a steady-state sequence that provides high SNR efficiency with mixed T2/T1 contrast. It is very similar to a common clinical sequence, bSSFP, but without the sensitivity to off-resonance banding artifacts. In STFR, a tip-down RF pulse that is typically much smaller than 90° excited the magnetization onto the transverse plane. Then, a free precession interval $\mathrm{T}_{\mathrm{free}}$ with phase acrual θ_{f} occurs, with the echo time typically occuring halfway through the interval. After $\mathrm{T}_{\mathrm{free}}$, a tip-up RF pulse recovers the magnetization to the longitudinal axis. A final crusher gradient θ_g is applied to remove all residual transverse magnetization. Figure 2.5 shows the STFR sequence diagram. STFR has the potential for including RF spoiling which can permit distinct tip-down and tip-up excitation patterns, for example in Ref. [8] where the tip-down pulse is spatially selective while the tip-up pulse is not and the RF spoiling helps prevent coherent steady-state signal from undesired excitation after the tip-down pulse. Meanwhile, unspoiled STFR requires equivalent, synergistic tip-down and tip-up pulses but is less sensitive to phase mismatch between tip-down and tip-up pulses compared to the spoiled counterparts [38]. In addition to conventional rapid T2/T1 imaging, STFR has also been applied to fMRI [39].

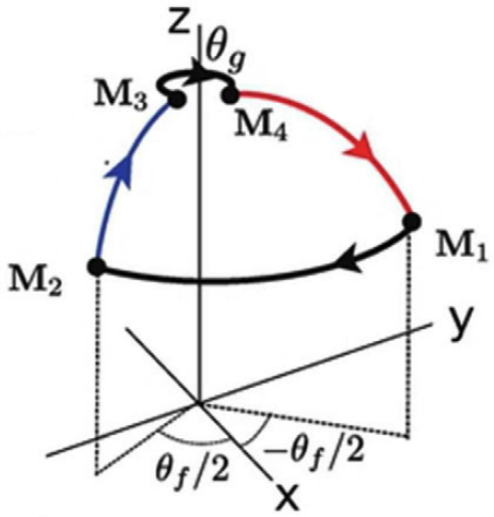

Figure 2.5: Small-tip fast recovery (STFR) sequence diagram [3]. M_1 is the magnetization state after tip-down, M_2 is the state after free precession $\mathrm{T}_{\mathrm{free}}$, M_3 is the state after tip-up and M_4 is the final state of a single TR after the gradient crusher θ_g

CHAPTER 3

Constrained RF Pulse Design

3.1 Introduction

The common regularized weighted least-squares formulation of the RF pulse design (Eq. (2.13)) problem can provide physically realizable pulses, but does not guarantee an optimal solution that also meets experimental constraints because of the "check-and-redesign" parameter tuning. In fact, many RF pulse design techniques such as fast inner-volume imaging and joint RF/gradient waveform design [8], [40], [41], [26] still use this regularized approach today. With more sophisticated and computationally complex designs, parameter tuning becomes a limiting factor. It is difficult to efficiently handle multiple RF constraints with regularized pulses and it is non-ideal to tune parameters in cases where the design occurs on-line with the patient in the scanner.

Contrained RF pulse design methods (Eq. (2.15)) eliminate the need for parameter tuning. This Chapter presents our technique for RF pulses that directly constrain RF peak amplitude, RF integrated power, and even slice selection performance. Here we study constrained RF pulse design for SMS pulses, and RF pulses designed in subsequent Chapters 4-5 also solve the constrained RF pulse design problem. The work in this chapter was presented in [13] and [14].

3.2 Application: Simultaneous Multislice

A specific RF pulse design application where constrained RF pulse design has significant potential is simultaneous multislice imaging, also known as Multiband (MB) imaging. SMS excitation is an effective means of accelerating imaging by exciting multiple slices separated by some distance, reducing the total number of excitations required to obtain a full volume. This speedup is known as the MB factor. SMS is particularly useful for applications where speed is critical such as cardiac imaging, where a time series is collected

such as fMRI and contrast enhanced MRI, and where acquisitions are long such as diffusion tensor imaging [42].

Conventional SMS imaging operates on the principle of the Fourier shift theorem, where multiple slices are excited at different phases [43]. Summing these pulses creates a conventional multiband pulse:

$$b_{MB}(t) = A(t) \cdot \sum_{n=1}^{N} \mathrm{e}^{i\Delta z_n t + \phi_n} \tag{3.1}$$

where $A(t)$ is the slice select envelope, N is the MB factor, and z_n is the slice position at each nth slice with phase offset ϕ_n. $A(t)$ is typically a standard slice-selective RF pulse shape, usually designed with the Shinnar Le-Roux (SLR) algorithm [24]. During excitation, a common slice-select gradient $g_z(t)$ is played.

Due to the summing of many RF pulses, SMS pulses have flip angle and multiband (MB) factor limitations that are usually dictated by either the RF pulse peak amplitude limit or power deposition. These restraining factors are shown pictorally in Figures 3.1 and 3.2, where a single 90° RF pulse is used to generate a MB=5 pulse that exceeds hardware constraints. In general, both the power deposition and peak amplitude of SMS pulses scale roughly linearly with the number of slices [44].

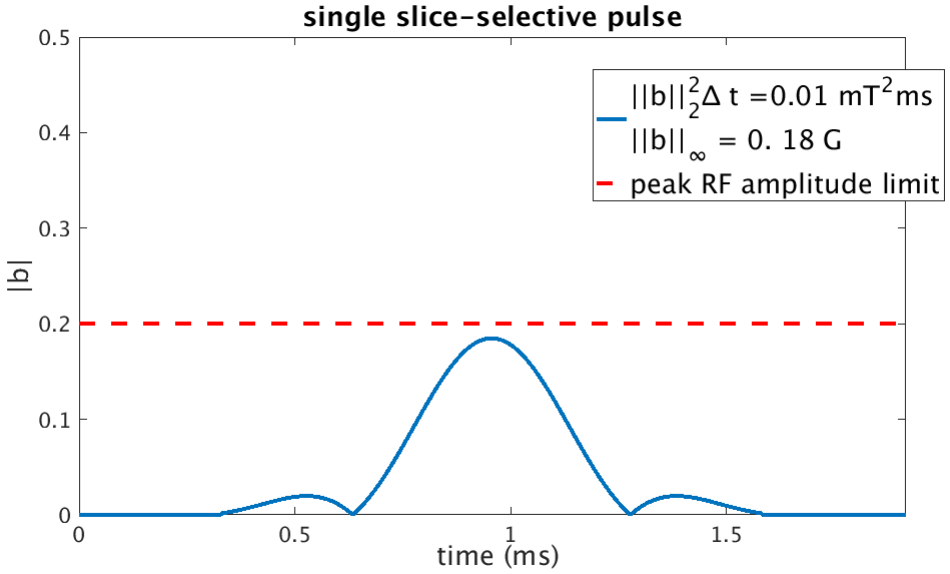

Figure 3.1: Single slice-selective 90° RF pulse. The integrated power deposited and peak amplitude are below hardware limits.

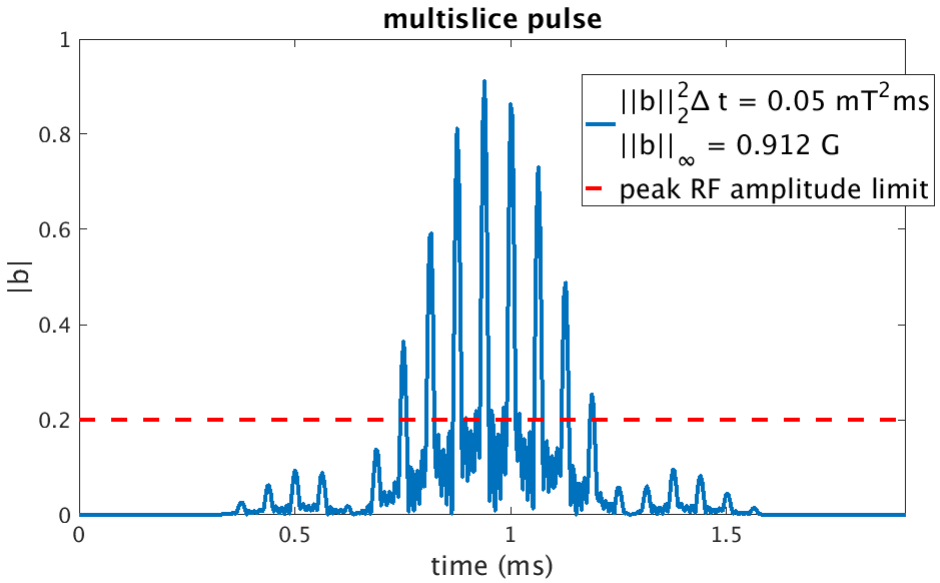

Figure 3.2: Multiband (MB)=5 slice-selective 90° RF pulse. Summing the RF pulses for SMS excitation causes the peak amplitude limit to be exceeded, and likely intergrated power as well.

These power and peak limitations in SMS motivate a constrained RF pulse design that designs pulses with the constraints set directly. Existing methods have been proposed to address peak amplitude or power limits of SMS through indirect means [44], [45], [46], [47]. More recently, a physical constraints Optimal Control (OC) method was introduced [48], but nevertheless still involved some parameter tuning to regularize the controls. This chapter proposes a new SMS RF pulse design method that uses the STA approximation with direct constraints using a least-squares optimization without any parameter tuning. The intended SMS applications are for cases with long TRs such as fMRI, where the main RF limit is peak amplitude, and short TR, low flip angle cases like cardiac imaging, where peak amplitude and Specific Absorption Rate (SAR) are both of interest.

3.3 Methods

In general, these pulse designs follow the general form from Eq. (2.15) in Chapter 2.

3.3.1 Peak-constrained SMS Design

We first begin constrained SMS pulse design by focusing on a design that solely constrains the peak RF amplitude. This is often the case in fMRI where flip angles are modest

(below 90°) and long TR's for maximizing SNR of the Blood Oxygen Level Dependent (BOLD) signal [49]. For peak-constrained SMS pulse design, we solve for RF pulse **b** via the following optimization problem,

$$\begin{aligned} \widehat{\mathbf{b}} = \underset{\mathbf{b}}{\text{argmin}} \ \ & ||\mathbf{Ab} - \mathbf{d}||_{\mathbf{W}}^2 \\ \text{s.t.} \ \ & ||\mathbf{b}||_\infty \leq b_{\max} \end{aligned} \tag{3.2}$$

where **A** is the STA system matrix, **d** is the target mutliband excitation pattern, **W** is a weighting matrix denoting "don't care" transition regions between in-slice and out-of-slice regions, and $b_{\max}$ is the RF amplifier peak amplitude limit in Gauss. The target pattern **d** is not simply a magnitude SMS pattern, but each slice is also "optimized phase-scheduled" for the particular MB factor according to an exhaustive search done in Ref. [44]. This single constraint RF pulse design problem is solved with FISTA [32]

We design these constrained pulses for various MB factors with a target flip angle of α=55°. We compared them to conventional SMS pulses designed by combining SLR pulses (Eq. (3.1)) with optimized phase scheduling [44]. We used magnitude Normalized Root Mean Squared Error (NRMSE) as a simulation metric of comparison for these pulses,

$$\text{Mag. NRMSE} = \frac{||\mathbf{m}_{xy} - \mathbf{d}||_{\mathbf{W}}}{\alpha||\mathbf{1}||_{\mathbf{W}}} \tag{3.3}$$

where **1** is a vector of one's. We also compared % maximum error (relative to the target pattern) within the slice and out of the slice. Finally, we compared the mean standard deviation of in-slice phase, which ideally should be zero.

We implemented these pulses experimentally in the FBIRN phantom [50] using a 2D gradient echo sequence where we set the readout direction along the slice dimension. In this way, the experimental slice profiles could be compared for the magnitude images. To mimic the conditions of an fMRI experiment, we set TE/TR = 4.8 ms/300 ms.

3.3.2 Peak- and Power-constrained SMS Design

We also designed constrained SMS pulses for the purpose of cardiac imaging. In this application the flip angle is still within the STA regime, but imaging is often employed in steady-state sequences like bSSFP where the TR is relatively short. With a higher RF duty cycle, power deposition or SAR is also a design concern in addition to peak RF amplitude. The two-constraint design is written as

$$\begin{aligned} \widehat{\mathbf{b}} = \underset{\mathbf{b}}{\text{argmin}} \ \ & ||\mathbf{Ab} - \mathbf{d}||_{\mathbf{W}}^2 \\ \text{s.t.} \ \ & ||\mathbf{b}||_\infty \leq b_{\max} \\ \text{and} \ \ & C_{\text{SAR}}||\mathbf{b}||_2^2 \Delta t \leq p_{\max} \end{aligned} \tag{3.4}$$

where $p_{\max}$ is a power constraint in $\mathrm{W/kg}$, Δt is the dwell time in ms, and C_{SAR} is a measured constant coverting integrated RF power in units $\mathrm{G}^2 \cdot \mathrm{ms}$ to power units. With two convex constraints, the RF pulse can no longer be easily designed with FISTA. However, the pulse design problem is 1D (target pattern solely defined along slice dimension), and therefore relatively small. This allow us to use the convex programming software CVX [35].

Because CVX does not support complex numbers, some re-arranging of the pulse design problem must be done to divide all terms of the optimization cost function into real and imaginary components. For matrix $\mathbf{A} \in \mathbb{C}^{N_z \times N_t}$, vector $\mathbf{d} \in \mathbb{C}^{N_z}$, and matrix $\mathbf{W} \in \mathbb{R}^{N_z \times N_z}$, we rewrite the CVX-friendly versions as

$$\mathbf{A}_{\text{CVX}} = \begin{bmatrix} \texttt{Real}[\mathbf{A}] & -\texttt{Imag}[\mathbf{A}] \\ \texttt{Imag}[\mathbf{A}] & \texttt{Real}[\mathbf{A}] \end{bmatrix} , \tag{3.5}$$

$$\mathbf{d}_{\text{CVX}} = \begin{bmatrix} \texttt{Real}[\mathbf{d}] \\ \texttt{Imag}[\mathbf{d}] \end{bmatrix} , \tag{3.6}$$

and

$$\mathbf{W}_{\text{CVX}} = \begin{bmatrix} \mathbf{W} & \mathbf{0}_{N_z} \\ \mathbf{0}_{N_z} & \mathbf{W} \end{bmatrix} . \tag{3.7}$$

By applying these specialized matrix/vector forms to Eq. (3.4), we can solve for a real-valued length $2N_t$ RF pulse that is re-combined into complex form.

We compared these peak- and power-constrained SMS pulses to the conventional SLR pulse with phase scheduling. These pulses were evaluated only in simulation.

3.3.3 Minimum Out-of-Slice Error SMS Design

Peak amplitude and integrated power are common RF pulse design parameters of interest for constraints. We use SLR pulses as a comparison to our constrained SMS pulses, which are designed from the filter-design perspective instead [24]. For SLR pulses, quantities like the amplitudes of the passband ripple δ_1 and stopband ripple δ_2 as well as passband

and stopband edges F_p and F_s are considered in the design trade-off. Therefore, we also explored designing a constrained SMS pulse that was better matched to the conventional SLR pulse by considering in-slice and out-of-slice excitation error (analagous to ripple). The RF pulse design problem in this case minimizes out-of-slice error as

$$\begin{aligned} \widehat{\mathbf{b}} = \underset{\mathbf{b}}{\text{argmin}} \ ||\mathbf{Ab}-\mathbf{d}||_{\infty,\mathbf{W}_{\text{out}}} \\ \text{s.t.} \ \ ||\mathbf{b}||_\infty \leq b_{\max} \\ C_{\text{SAR}}||\mathbf{b}||_2^2 \Delta t \leq p_{\max} \\ ||\mathbf{Ab}-\mathbf{d}||_{\infty,\mathbf{W}_{\text{in}}} \leq e_{\max} \end{aligned} \tag{3.8}$$

where $\mathbf{W}_{\text{in}}$ and $\mathbf{W}_{\text{out}}$ are in-slice and out-of-slice regions, respectively, and $e_{\max}$ is an in-slice error constraint. All of these values are based on the equivalent SLR pulse. For example, $\mathbf{W}_{\text{in}}$ and $\mathbf{W}_{\text{out}}$ come from the fractional transition width $\mathbf{W}_{\text{SLR}}$=$D_\infty(\delta_1,\delta_2)/\text{TBW}$ for particular time bandwidth product (TBW) and D_∞ outlined in [24]. The in-slice error constraint is set based on the in-slice error of an SLR pulse with default values of δ_1=0.01 and δ_2=0.01. Figure 3.3 visualizes the minimization of out-of-slice error with in-slice error constraint.

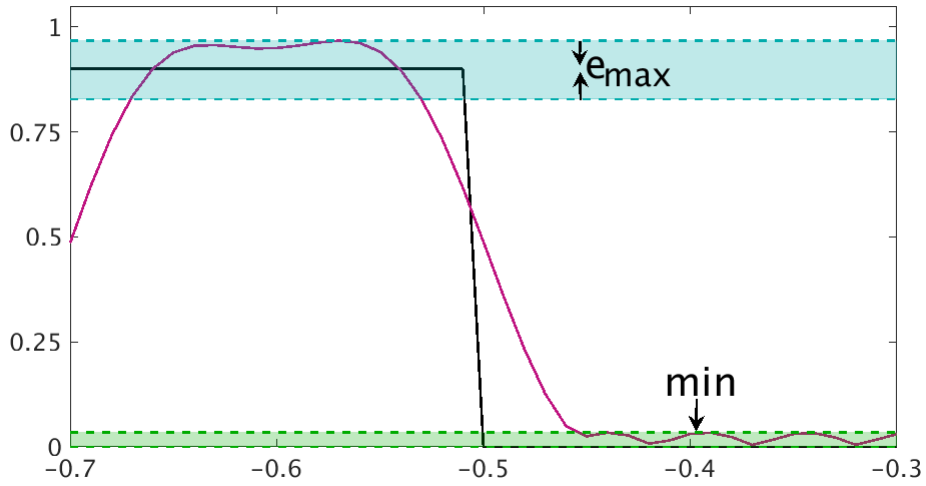

Figure 3.3: With an in-slice error constraint $e_{\max}$ in blue, we minimize the maximum out-of-slice error in green.

We designed these minimum out-of-slice error constrained SMS pulses again in CVX as in Section 3.3.2. We compared constrained designs to SLR-based SMS pulses with the same in-slice and out-of-slice ripple settings, this time with MB=8 and pulse length 0.95

ms. For the SLR, both the default Least-Squares (LS) and classic Parks-McClellan (PM) filters were explored. The pulse designs were compared both in simulation and with the phantom in a 2D SPGR acquisition with FA/TE/TR=23.1°/4.2ms /15.96 ms.

3.3.4 Magnitude Least-Squares Constrained SMS Design

One final variant of SMS design we tried was to take the minimum out-of-slice formulation (Eq. (3.8)) and adjust the design for magnitude least-squares. This concept, adapted from [51], allows the excitation phase to vary smoothly, potentially adding more design freedom in the excitation magnitude. The magnitude least-squares approach is applicable for SMS because the ultimate goal is slice selective MB pulses, and although they have an initial target phase pattern based on an optimized phase schedule [44], the final RF excitation behavior need not have any particular phase. The only true phase requirement is that the phase within each individual slice be relatively constant. The magnitude least-squares approach is done by solving Eq. (3.8) more than once, each time with a phase estimate update to the target pattern $\mathbf{d}$. Algorithm 1 outlines the magnitude least-squares approach for constrained SMS design.

The number of phase update iterates P is somewhat of a heuristic, but typically only a few iterations (up to P=10) are needed. For example, Figure 3.4 shows the target phase $\phi^{p,j}$ for each jth slice at iterations p=1,2, and 10 (initial design from Wong's phase scheduling [44], after one phase update, and at the final update). As you can see in this demonstrative example, little change occurs in the target phase between the initial and final phase update.

Algorithm 1 Pseudocode for designing constrained MB=N SMS pulse with P phase updates via magnitude least-squares

Input: Target pattern $\mathbf{d}$, in-slice and out-of-slice weighting matrices $\mathbf{W}_{in}$ and $\mathbf{W}_{out}$, slice-select excitation trajectory k_z, and constraints (peak amplitude, integrated power, and in-slice error)

Output: RF pulse $\mathbf{b}$ with phase updates

Initialization :

Set $\mathbf{d}^1 = \alpha \mathrm{e}^{i\angle \mathbf{m}_{\mathrm{STA,SLR}}}$

Magnitude least-squares phase updates :

for p=1:P **do**

Design constrained SMS RF pulse to match target pattern $\mathbf{d}^p$

$$\begin{aligned} \widehat{\mathbf{b}}^p = \underset{\mathbf{b}}{\operatorname{argmin}} \ & ||\mathbf{A}\mathbf{b} - \mathbf{d}^p||_{\infty,\mathbf{W}_{out}} \\ \text{s.t.} \ & ||\mathbf{b}^p||_\infty \leq b_{\max} \\ & C_{\mathrm{SAR}}||\mathbf{b}^p||_2^2 \Delta t \leq p_{\max} \\ & ||\mathbf{A}\mathbf{b} - \mathbf{d}^p||_{\infty,\mathbf{W}_{in}} \leq e_{\max} \end{aligned}$$

Use STA approximation to estimate transverse magnetization $\mathbf{m}^p_{\mathrm{STA}} = \mathbf{A}\mathbf{b}^p$

for (n=1:N) **do**

Add perturbation RF pulse to previous designs, $\phi^{p,j}$=mean($\angle \mathbf{m}^{p,j}_{\mathrm{STA}}$)

end for

$\mathbf{d}^{p+1} = |\mathbf{d}^p| \circ \mathrm{e}^{i\phi^{p,j}}$

end for

return $\mathbf{b}^p \in \mathbb{C}^{N_t}$

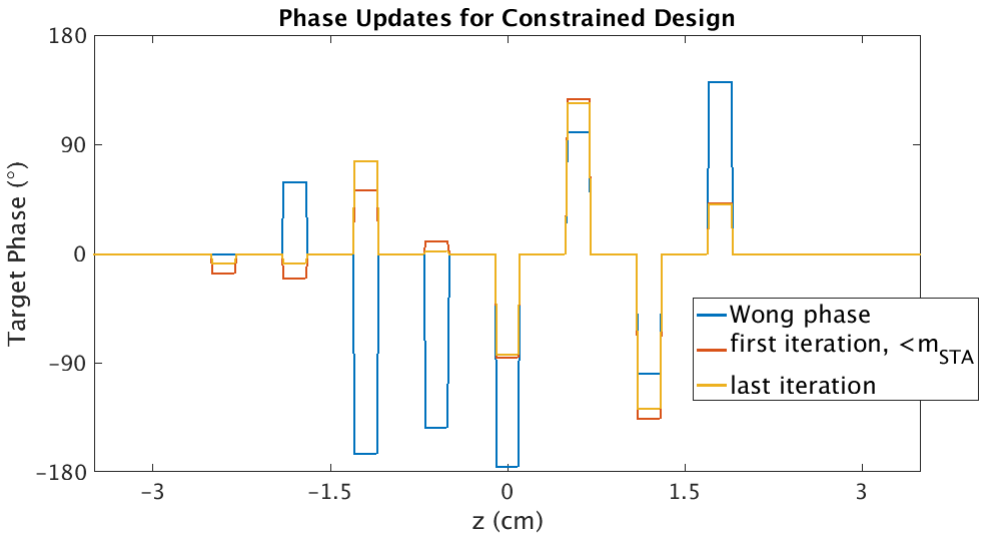

Figure 3.4: Target phase $\phi^{p,j}$ for each jth slice at a few phase update iterations p=1,2, and 10 (the final). The initial phase pattern is defined by Wong's phase scheduling [2].

This magnitude least-squares based design was implemented in the same experimental SPGR sequence described in 3.3.3 for comparison.

3.4 Results

3.4.1 Peak- and Power-Constrained SMS Pulses

3.4.1.1 Simulation

For the solely peak-constrained SMS pulses (Section 3.3.1), we compared the apparent trade-off between RF pulse length and NRMSE with constrained SMS pulses. For varying MB factors, a shorter pulse can be obtained compared to an equivalent SLR-based SMS pulse for the same NRMSE or vice versa, same length pulse with lower NRMSE. Figure 3.5 summarizes these results.

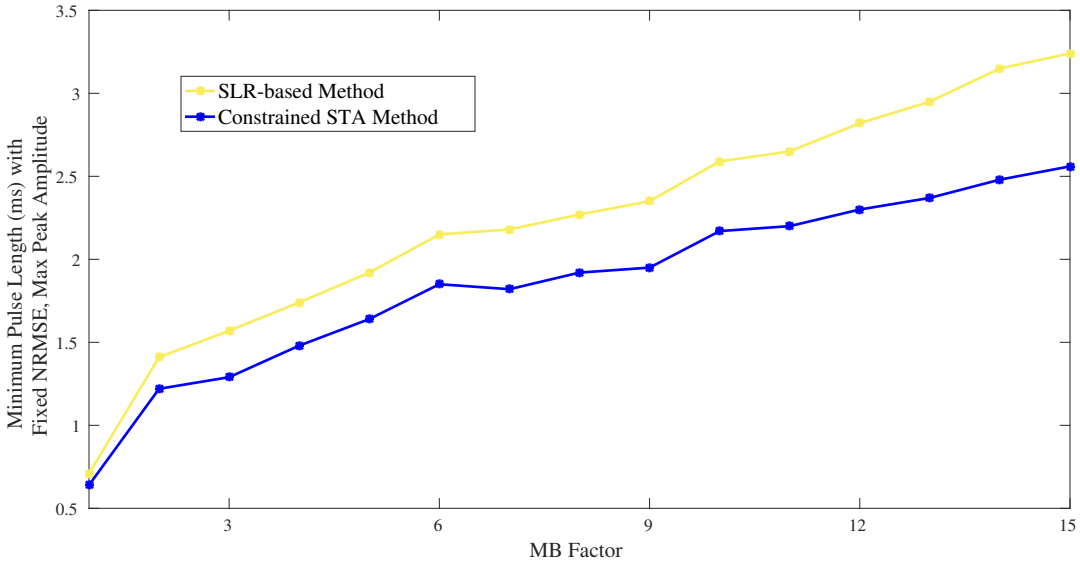

Figure 3.5: Minimum pulse length possible for a fixed peak amplitude and total magnitude NRMSE as a function of MB factor. This plot compares this relationship for both SLR-based designs and the proposed peak-constrained (3.2) method.

We evaluated a MB=9 SMS pulse for further simulation and experimental results. Using the peak-constrained method, we designed constrained pulses with the same error (shorter pulse, 1.95 ms) or same pulse length, 2.35 ms (less error) compared to a MB=9 SLR pulse. Figure 3.6 shows the RF waveforms for the constrained and comparative SLR-based pulses with their simulated (Bloch and STA approximation) slice profiles.

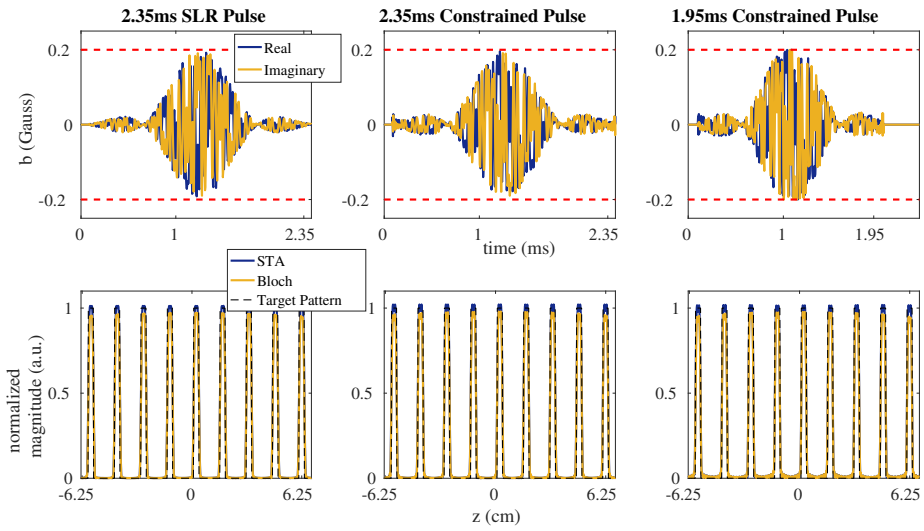

Figure 3.6: RF waveforms (top) and Bloch-simulated magnetization magnitude (bottom) of 9MB SMS pulses for the SLR-based method, the peak-constrained STA method with lower error and same pulse length, and the peak-constrained STA method with same error and shorter pulse length.

Table 3.1 lists performance metrics for the SLR and peak-constrained pulse designs from Bloch simulation. All pulse methods exactly meet the peak amplitude constraint of 0.2 Gauss. Figure 3.7 plots the zoomed-in profile for a single slice with the three simulated MB=9 pulses, both at out-of-slice and in-slice regions. For this profile, the SLR pulse has a flatter slice profile and lower side lobes but is of higher magnitude NRMSE compared to the constrained pulses, perhaps, due to a broader transition region.

Table 3.1: Peak RF amplitude, Bloch simulation total magnitude NRMSE, % max magnitude error in-slice and out-of-slice, mean in-slice phase standard deviation for the MB=9 pulses designs. The best values are **bolded**.

RF SMS Pulse	$\|\|\mathbf{b}\|\|_\infty$ (G)	Total Mag. NRMSE	% Max Mag. Error In-Slice/Out-of-Slice	Mean St. Dev. Phase (°)
SLR, 2.35 ms	0.20	0.03	2.7/12.4	4.4
Peak-Constrained, 2.35 ms	0.20	**0.02**	**1.7/3.6**	3.5
Peak-Constrained, 1.95 ms	0.20	0.03	1.8/4.7	**3.4**

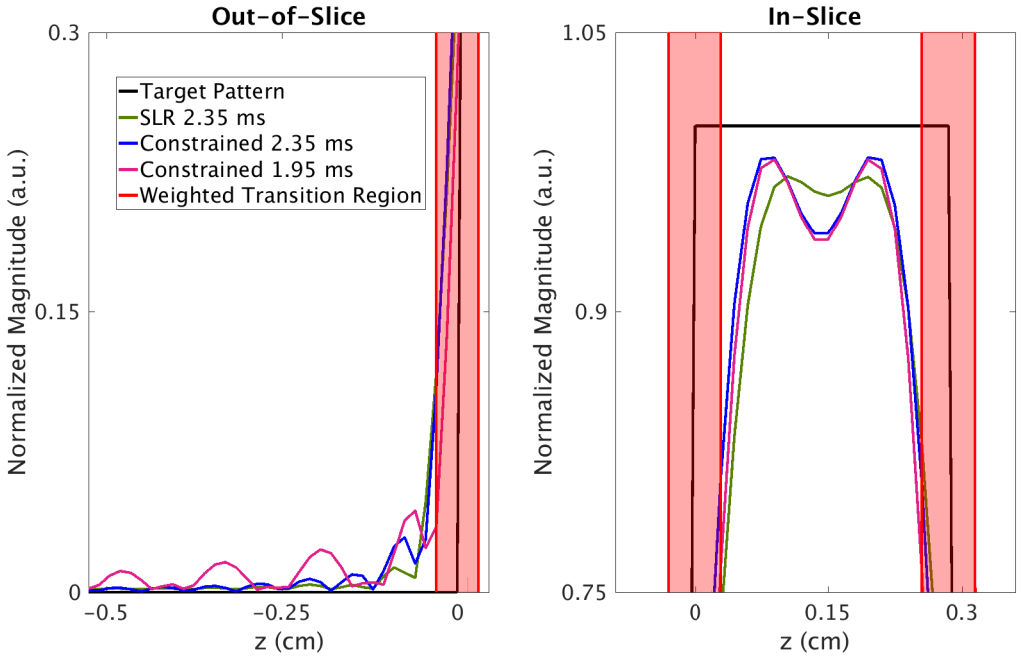

Figure 3.7: Bloch-simulated magnetization magnitude of 9MB SMS pulses for the SLR-based method, the peak-constrained STA method with lower error and same pulse length, and the peak-constrained STA method with same error and shorter pulse length. The left plot zooms in to directly outside a single slice profile and the right plot zooms in to within the same slice profile. The red shading marks the slice transition regions.

We then designed MB=9 SMS pulses using the peak-constrained (Section 3.3.1) and

peak- and power-constrained methods (Section 3.3.2), with the same error as an SLR pulse (shorter pulse, 1.95 ms). The power constraint was set for a conservative 1.2 W/kg. These pulses were compared via Bloch simulation only. Table 3.2 lists performance metrics for the SLR and constrained pulse designs from Bloch simulation. Although all pulse methods exactly meet the peak amplitude constraint, only the power-constrained method meets the lower power constraint. The SLR and peak-constrained pulses meet the same magnitude NRMSE yet exhibit different slice profiles. Figure 3.8 plots the zoomed-in profile for a single slice with the three simulated MB=9 pulses, both at out-of-slice and in-slice regions.

Table 3.2: Peak RF amplitude, deposited power, Bloch simulation total magnitude NRMSE, % max magnitude error in-slice and out-of-slice, mean in-slice phase standard deviation for the MB=9 pulses designs. The best values are **bolded**, and the values exceeding the power constraint (not apart of explicit design) are in red.

RF SMS Pulse	$\|\|\mathbf{b}\|\|_\infty$ (G)	$C_{\mathrm{SAR}}\|\|\mathbf{b}\|\|_2^2\Delta t$ (W/kg)	Total Mag. NRMSE	% Max Mag. Error In-Slice/Out-of-Slice	Mean St. Dev. Phase (°)
SLR, 2.35 ms	0.20	1.3	**0.03**	2.7/12.4	4.4
Peak-Constrained, 1.95 ms	0.20	1.5	**0.03**	**1.8**/4.7	3.4
Peak- and Power-Constrained, 1.95 ms	0.20	**1.2**	0.05	6.2/**4.5**	**2.9**

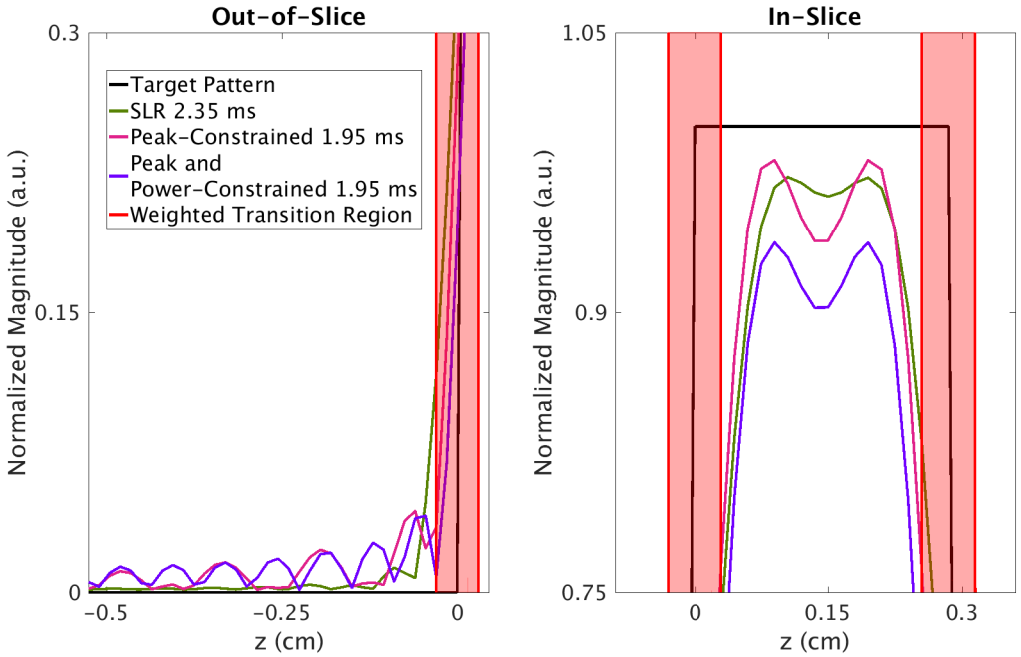

Figure 3.8: Bloch-simulated magnetization magnitude of 9MB SMS pulses for the SLR-based method, and the peak-constrained STA (Eq. (3.2)) and peak- and power-constrained (Eq. (3.4)) methods with same error and shorter pulse length. The left plot zooms in to a single slice profile and the right plot zooms in to directly outside the profile. The red shading marks the slice transition regions.

3.4.1.2 Phantom Data

Figure 3.9 shows the 2D magnitude images from experimental implementation of the SMS pulses designed comparing peak-constrained formulations (Section 3.3.1) in the FBIRN phantom. This figure also show the 1D slice profiles derived from the experimental images.

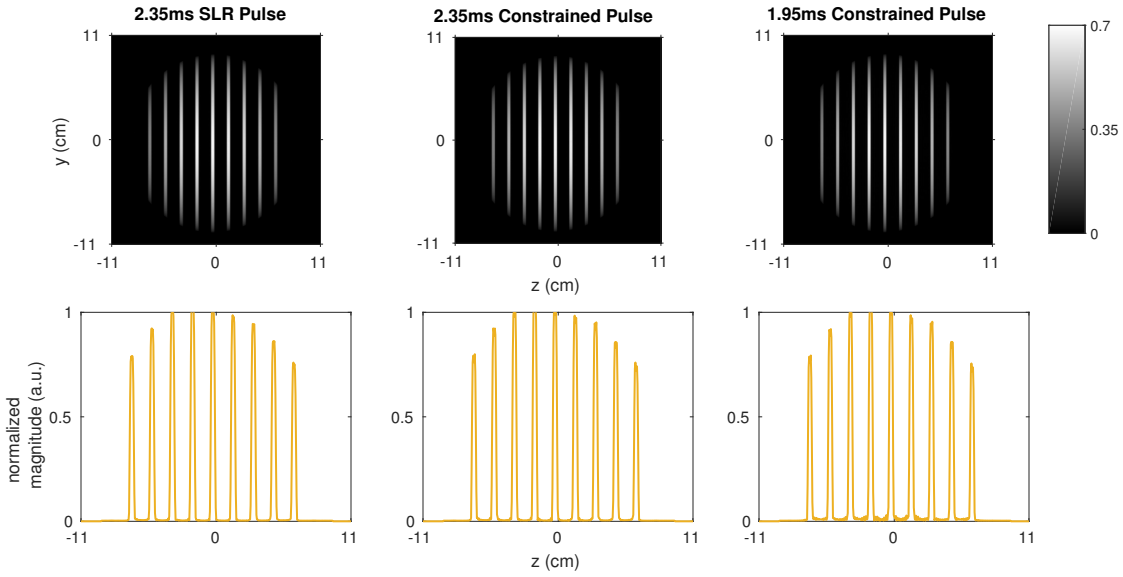

Figure 3.9: Experimental 2D magnitude images and corresponding 1D slice profiles of SLR-based and proposed peak-constrained (Eq. (3.2)) RF pulses.

3.4.2 Minimum Out-of-Slice SMS Pulses

3.4.2.1 Simulation

Figure 3.10 shows four MB=8 SMS RF pulses: the SLR pulse designed with Least-Squares filter, the SLR designed pulse with Parks-McClellan filter, and our proposed minimum out-of-slice error (Eq. (3.8)) method without and with the magnitude least-squares phase updates. These complex RF waveforms are realizable in the MR scanner.

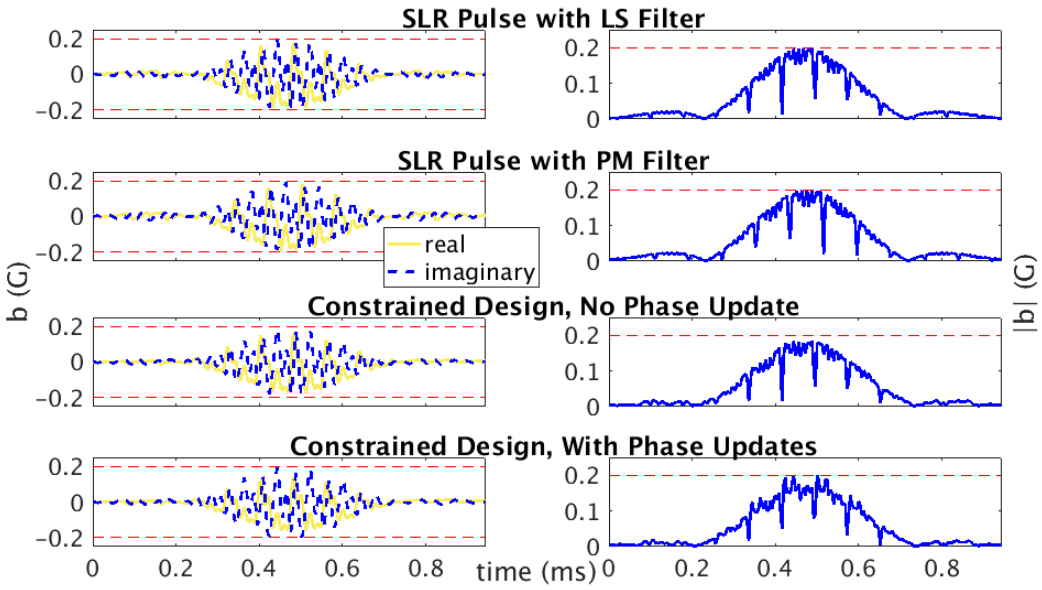

Figure 3.10: RF waveforms of MB=8 SMS pulses for the LS and PM SLR-based methods, and the minimum out-of-slice constrained methods without and with phase updates using magnitude least-squares. The left column shows the real and imaginary components, while the right column shows the magnitude waveform.

Table 3.3 reports the simulated magnetization performance for the same four SMS pulses. It also lists two additional designed pulses, constrained minimum out-of-slice pulses without and with phase updates for a shorter (0.8 ms) pulse that has the same out-of-slice error as the SLR SMS pulse designed with LS filter, which was the better-performing SLR-based pulse. Figure 3.11 show the simulated magnetization performance and magnitude profiles for the original four SMS pulses over the full excitation Field of View (FOV) as well as a zoomed-in profile of a single slice. The constrained SMS pulse designs deposit less power and acheive lower maximum out-of-slice excitation error compared to the SLR pulses.

Table 3.3: Peak RF amplitude, deposited power, and Bloch simulation max magnitude error in-slice and out-of-slice for the MB=8 pulses designs comparing SLR and minimum out-of-slice pulse designs. The top row of values in green list the design constraints, and the best performance values are **bolded**. The red rows show simulated values for constrained pulses that are shorter than the other SMS pulses, but rather designed to obtain the same maximum out-of-slice error as the best performing SLR-based pulse (with LS filter).

RF SMS Pulse	$\|\|\mathbf{b}\|\|_\infty$ (G)	$C_{\mathrm{SAR}}\|\|\mathbf{b}\|\|_2^2\Delta t$ (W/kg)	Max In-Slice Error	Max Out-of-Slice Error
Constraints	0.20	1.3	0.25	N/A
SLR with LS filter	0.20	7.0E-3	0.25	0.4E-2
SLR with PM filter	0.20	7.0E-3	0.25	1.4E-2
Constrained, No Phase Updates	0.18	6.0E-3	0.25	**0.1E-2**
Constrained, With Phase Updates	0.20	6.0E-3	0.25	**0.1E-2**
Shorter Constrained, No Phase Updates	0.20	6.0E-3	0.25	0.4E-2
Shorter Constrained, With Phase Updates	0.20	6.0E-3	0.25	0.4E-2

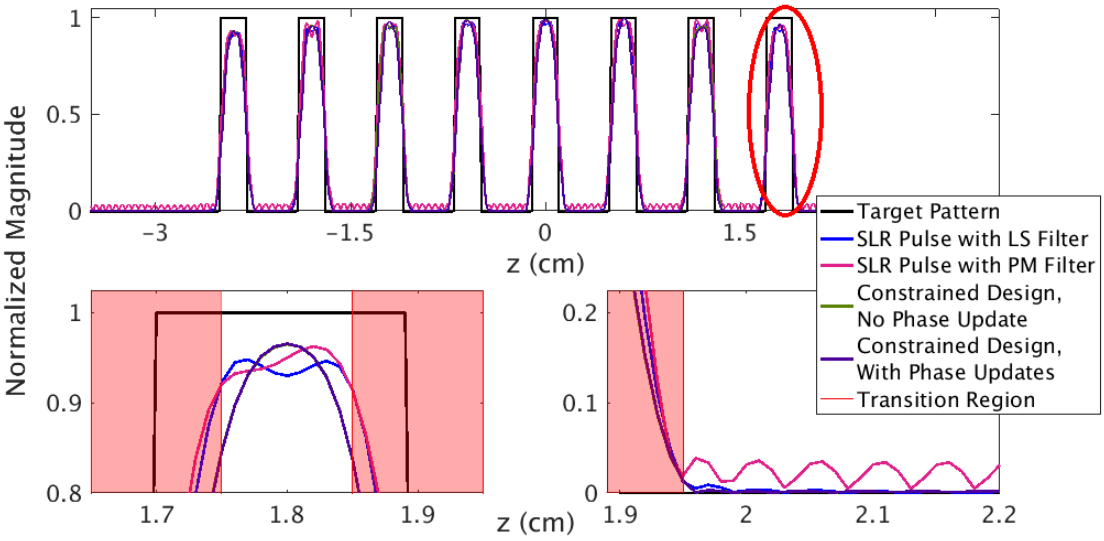

Figure 3.11: Bloch simulated magnetization magnitude of 4 MB=8 RF pulses: SLR with PM and LS filters and constrained minimum out-of-slice error without and with phase updates. The top row shows the full FOV of the design in the slice dimension, while the bottom rows shows zoomed-in profiles of the right-most slice. Here the constrained designs (with and without phase updates) are nearly identical.

3.4.2.2 Phantom

Figure 3.12 shows the 2D magnitude images from experimental implementation of the SMS pulses designed comparing minimum out-of-slice formulations in the FBIRN phantom. This figure also show the 1D slice profiles derived from the experimental images, and a zoomed-in profile from a single-slice (same single slice as shown in simulation).

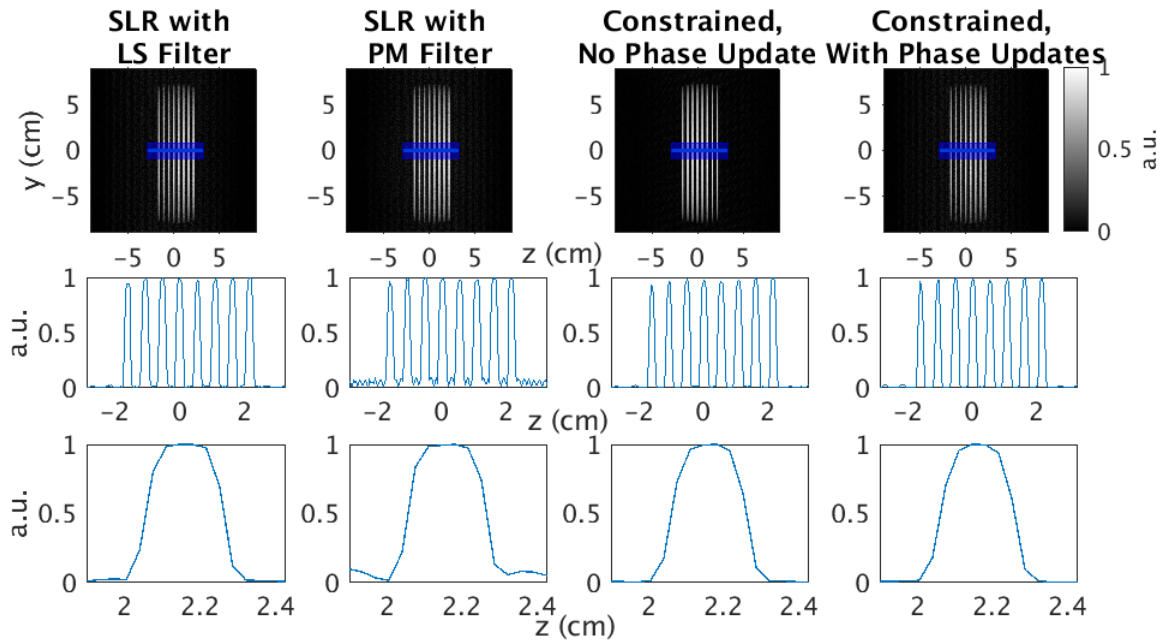

Figure 3.12: 2D images (top) and averaged line profile (middle) with zoomed right-most slice (bottom) for 4 RF pulse designs (SLR with PM and LS filters, constrained minimum out-of-slice error without and with phase updates).

3.5 Discussion

Constraining RF peak amplitude and/or integrated power is a useful approach to RF pulse design because direct physical constraints can be set for a particular problem. This approach eliminates the need for parameter tuning, which can be imperfect and time-consuming. This Chapter explored SMS as an interesting application for constrained RF pulse design because power deposition and RF amplitude limits often dictate the MB factor for image acceleration, with an additional factor being the receive coil sensitivity for signal disentanglement [42]. Depending on the SMS application, RF peak amplitude and/or power might be the dominant constraint. For example, in Section 3.3.1 the fMRI-driven application saw that peak amplitude was dominant. Likewise, in Section 3.3.2 the cardiac imaging saw both peak amplitude and power to be equally important. Although untested, we hypothesize that diffusion tensor imaging applications of SMS might be RF power constraint-driven because of the high flip angle 180° pulses needed for spin echos. This topic could be explored with more advanced LTA designs, which is beyond the context of the STA pulses described in this chapter.

In addition to a more direct design, Figure 3.5 summarizes the additional performance

gains that can be made with a constrained SMS pulse design approach. Compared to the conventional SLR-based SMS pulse, a constrained SMS pulse can have lower exciation error (magnitude NRMSE) for the same length pulse. The inverse relationship applies, in that shorter pulses for the same NRMSE can be obtained, which is useful since shorter pulse lengths are more amenable to faster imaging sequences which furthers the motivation for SMS acceleration.

Figure 3.6 shows that the constrained RF waveforms do not deviate much visually from the conventional SLR pulses. It also shows that the STA approximation is well met for these pulses, since the STA magnetization profiles are in good aggreement with Bloch simulation.

Tables 3.1-3.2 and Figures 3.7-3.8 again emphasize the performance gains for constrained SMS pulse designs compared to conventional SLR-based methods. In every performance metric, the constrained versions performed best. As expected, there was some loss in performance gains for the pulses designed with both peak and power constraints, but it is interesting to note that those pulses acheived the best mean standard deviation of phase within slices. In viewing the simulated magnetization profiles, we notice that there appears to be more out-of-slice excitation for the constrained pulses. It might suggest that the constrained optimization pushes for more ripple, but better adherence to the transition band. It is also possible that the peak out of band error is lower than the other methods, although the ripple is higher. In this work we did not do a full 3D SMS acqusition with slice disentanglement, but it would be interesting to see how the ripple manifests in leakage amongst neighboring slices. This observation was a motivating factor for the minimum out-of-slice error formulation presented in Section 3.3.3.

The experimental images in Figure 3.9 are visually similar; perhaps the shorter constrained pulse exhibits more out-of-slice excitation error in the 1D profile. These 1D profiles are pre-corrected for signal intensity variations in the phantom due to conductivity. The additional roll-off in slice profile intensity at the edge slices is still an open question, but can be seen in other SMS pulse design works such as Ref. [45].

Comparing minimum out-of-slice error constrained SMS pulses provided additional insight. As seen in Fig. 3.6, Figure 3.10 shows that the constrained vs. SLR SMS waveforms are visually similiar. The pulse designed with phase updates is the most distinct in the magnitude waveform. For performance comparison in Table 3.3 and Figure 3.11, we note that the minimum out-of-slice constrained formulations improved performance (for the same pulse length) while depositing less RF power contributing to SAR. However, in all pulse designs, the set power constraint was not exceeded. Unfortunately, there is no notable improvement by adding the magnitude least-squares phase updates in terms of performance

metrics or simulated profiles. The SLR-based pulse with PM filter seems to perform poorly in the out-of-slice regions. Further exploration of weighting/constraining out-of-slice vs in-slice error paired with a 3D SMS acquisition could provide additional insight such as slice leakage due to out-of-slice ripple.

In Fig. 3.12 the SMS pulses designed with SLR and LS filters and the minimum out-of-slice constrained versions again appear similar to the eye. However, as seen in simulation, the SLR with PM filter does much worse in that a lot of out-of-slice excitation occurs.

For this SMS work, we present all experimental data in 2D showing the slice profiles along the readout dimension. However, SMS is ultimately intended for faster imaging over a 3D volume, in which the total volume acquisition time is reduced by the MB factor. To obtain 3D SMS images, a special acquisition-reconstruction method is required, called Controlled Aliasing in Parallel Imaging Results in Higher Acceleration (CAIPIRINHA) [52]. A variant approach called Blipped-CAIPI was introduced and is the standard for SMS imaging [53]. To date, we have not implemented the full Blipped-CAIPI acquisition and reconstruction on our 3T GE scanner but is a potential future work.

3.6 Conclusion

In this Chapter we have explained the rationale for designing RF pulses with direct, meaningful constraints. Although this approach may mean slightly more sophisticated or computationally expensive solvers, the end result are pulses that are guaranteed to be realizable in the MRI scanner without any parameter tuning. We demonstrate the utility of constrained RF pulse design in simultaneous multislice pulse design, because variants of these pulses have different dominant constraints. Constrained RF pulse design is useful for other RF pulse types, and will be re-visited throughout the rest of this dissertation.

CHAPTER 4

2D Spectral-spatial Prewinding Pulses

4.1 Introduction

Inhomogeneity of the B0 field can cause spatially varying phase and signal loss in MRI. Spin-echo (SE) sequences can realign static off-resonance effects, but require a second refocusing RF pulse and may be unsuitable for short TR imaging or applications that are SAR limited [54]. Assländer et al. introduced spectral prewinding pulses to compensate for spin dephasing in rapid gradient echo sequences (GRE), effectively combining the speed of GRE with the off-resonance robustness of SE [15], for a restricted off-resonance bandwidth and limited TE.

Recently, spectrally selective phase prewinding pulses were incorporated into the STFR steady-state sequence [55]. The STFR sequence employs both a traditional "tip-down" pulse and then a "tip-up" pulse that quickly returns the magnetization to the longitudinal axis after free precession [6]. STFR has mixed T2/T1 contrast and provides nearly equal signal level and tissue contrast in the human brain as bSSFP. [56]. One challenge with bSSFP is that banding artifacts may occur [57] that can only be removed with multiple acquisitions and phase cycling [58]. With appropriately designed "tip-up" pulses, STFR can potentially eliminate the banding artifact in a single acquisition [6].

However, purely spectral prewinding pulses can refocus a limited range of frequencies [15]. This Chapter [1] proposes a spectral-spatial pulse that increases the effective prewinding bandwidth and mitigates the limitations of a purely spectral design. The key idea of this Chapter is to vary spatially the pulse design criterion based on voxel-by-voxel bulk off-resonance. The resulting pulse accommodates a wider effective bandwidth, improving signal recovery in inhomogeneous objects. Our proposed application for spectral-spatial STFR is brain imaging, where inhomogeneity in the B0 field is generally smoothly varying

[1] This Chapter has been published in the journal *Magnetic Resonance in Medicine*[9] and was first presented at ISMRM 2015 [16].

with a wide bandwidth.

In the following section we review spectral prewinding pulse design and introduce the extension to spectral-spatial prewinding pulses. We then formulate our constrained pulse design optimization problem under the STA approximation [22]. Next, we outline pulse design validation experiments in a phantom and in vivo human brain. We quantify performance with subsequently defined metrics. Finally, we present simulation and experimental results for the phantom and in vivo pulse designs.

4.2 Theory

4.2.1 Spectral Prewinding Pulse Design

After RF excitation, the phase accumulation of spin isochromats that occurs during a free precession interval of length T_{free} is

$$\theta_{\text{free}} = -2\pi f \mathrm{T}_{\text{free}} \tag{4.1}$$

where f denotes the off-resonance frequency [15]. To compensate for this precession, a spectral design [15],[55] "prewinds" for phase by using the following target excitation pattern:

$$d(f) = \alpha e^{2\pi i \mathrm{TE} f} \quad . \tag{4.2}$$

The spectral target pattern d is a function of flip-angle α and off-resonance frequency f. The phase evolution is set to refocus at TE, which is half of T_{free} in STFR sequences. The target excitation pattern vector $\mathbf{d} = [d(f_1), .., d(f_{N_\mathrm{f}})]^T$ consists of samples of Eq. (4.2) at N_f frequencies over some bandwidth of interest.

Prewinding will be most effective if limited to one half of the unit circle, or a spread of less than or equal to π. In previous experiments, we have noticed this relationship as an empirical off-resonance bandwidth limit. Therefore we use

$$\text{bandwidth} \leq \frac{1}{\mathrm{T}_{\text{free}}} \tag{4.3}$$

as a conservative upper limit for prewinding. Eq. (4.3) suggests that the widest bandwidth (range of f values used in Eq. (4.2)) for refocusing is obtained with a minimal free pre-

cession time. Free precession time is dictated by the data acquisition gradients which for certain applications and resolution might be too long. For example, a plausible $\mathrm{T_{free}}$ of 4 ms would conservatively allow for $\pm$125 Hz of refocusing and in some cases, this range is insufficiently wide to span the entire bandwidth of off-resonance frequencies at highly inhomogeneous regions within the human brain.

4.2.2 Spectral-Spatial Prewinding Pulse Design

To overcome the bandwidth limitations of the purely spectral prewinding design in [55], we propose a spectral-spatial RF pulse design approach that spatially adapts the spectral properties. The addition of spatial information allows the RF pulse to encode spatially varying off-resonance across the object. Even with a narrow design bandwidth, these pulses have the potential to track larger ranges of off-resonance by changing the design center frequency at each spatial location, provided these variations do not change too rapidly in space. Figure 4.1 illustrates this concept.

For the spectral approach, the target magnetization pattern **d** based on Eq. (4.2) for RF pulse design was simply a 1D vector corresponding to a range of off-resonance frequencies. In contrast, for the proposed spectral-spatial RF design approach, the target pattern is a function of two spatial dimensions and a spectral dimension. This feasibility study used a non-slice-selective 2D slice. For fully 3D imaging the spectral spatial pulse design would include three spatial dimensions and a 3D excitation trajectory. The target pattern **d** for spectral-spatial pulses consists of $N_\mathrm{x} \times N_\mathrm{y} \times N_\mathrm{f}$ samples of

$$d(x, y, f) = \alpha e^{2\pi i \mathrm{TE} f} \tag{4.4}$$

where N_x and N_y are the number of samples in the x and y dimensions. The spatial aspect in this design is captured by the diagonal weighting matrix **W** (used in Eq. (4.12) below) that has diagonal elements corresponding to samples of the following 3D weighting function $w(x, y, f)$:

$$w(x, y, f) = \begin{cases} 1, & |f - \Delta f(x, y)| \leq \frac{L}{2} \\ 0, & \text{otherwise} \end{cases} \tag{4.5}$$

where $\Delta f(x, y)$ denotes the measured field map and L is the user-defined local target bandwidth of the spectral-spatial pulse. In other words, L defines the local bandwidth that the spectral-spatial pulse uses to encapsulate the spatially varying off-resonance as illustrated by the shaded red region in the bottom right of Figure 4.1. This combined spatial-spectral

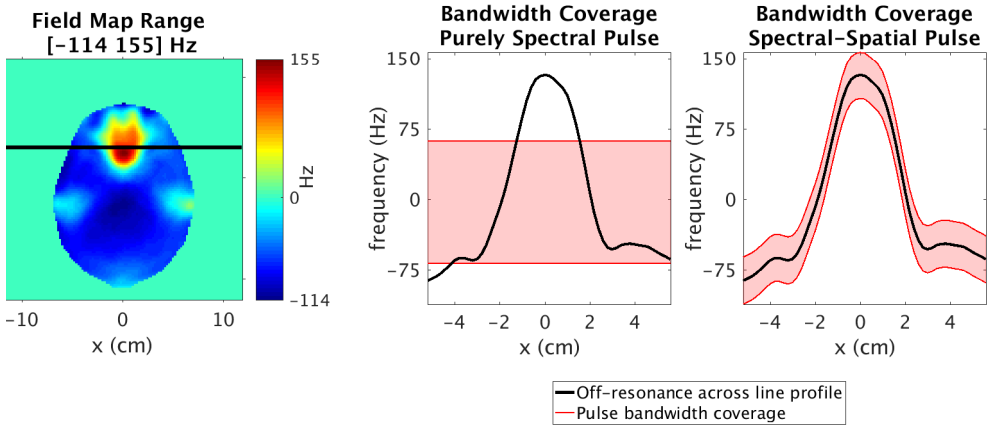

Figure 4.1: 1D conceptual representation of purely spectral and spectral-spatial prewinding pulse design. The left figure shows a typical human brain field map at a slice taken slightly above the sinuses, containing a significant range of off-resonance. A 1D line profile across one y-location of this field map is plotted in black on the right figures. The purely spectral pulse (center) does not vary the target recovery bandwidth spatially, while the spectral-spatial pulse (right) does.

weighting is the unique characteristic of the proposed approach. If the weights were set to unity everywhere, then the spectral-spatial approach would revert to a pure spectral design.

For additional exploration of local bandwidth L and diagonal weighting matrix $\mathbf{W}$ please see Appendix A Section 1

4.3 Methods

4.3.1 RF Pulse Design

Both purely spectral [15] and spectral-spatial pulses were designed using the STA approximation [22] for a target 2D slice. The STA approximation facilitates RF pulse design by establishing a linear Fourier relationship between RF waveform and transverse magnetization [1]. The tip-down pulse design target pattern $\mathbf{d}$ was defined for spectral pulses by Eq. (4.2) and for spectral-spatial pulses by Eq. (4.4), where off-resonance frequencies $\mathbf{f} = [f_1, ..., f_{N_\mathrm{f}}]^T$ were sampled from the off-resonance range measured in a field map. The tip-up pulses used simulated magnetization magnitude and phase at the end of free precession to assign the magnitude and phase of the target tip-up pattern [55]. The spectral-spatial pulse design used gradients played out during the RF pulse that trace out a variable density spiral k-space trajectory repeated multiple times. The speed and resolution of this trajectory permitted time between spirals to be spent at k-space center where we found that large amounts of RF energy are deposited.

We design the RF pulse by solving the STA constrained optimization problem:

$$\begin{aligned} \hat{\mathbf{b}} &= \underset{\mathbf{b}}{\operatorname{argmin}} \ ||\mathbf{Ab} - \mathbf{d}||_{\mathbf{W}}^2 \\ \text{s.t.} \ \ & C_{\mathrm{SAR}}||\mathbf{b}||_2^2 \Delta t \leq p_{\max} \end{aligned} \tag{4.6}$$

where $\hat{\mathbf{b}}$ is the optimized RF pulse, $\mathbf{W}$ is the diagonal weighting matrix composed of samples of weighting function $w(x, y, f)$ (Eq. (4.5)), C_{SAR} is a conversion constant, and $\mathbf{A}$ is the small tip system matrix with elements $a_{j,n} = i\gamma M_0 e^{2\pi i(\mathbf{r}_j \cdot \mathbf{k}_n)} \Delta t$. Here, vector $\mathbf{r}_j = (x_j, y_j, f_j)$ contains spatial location samples (x_j, y_j) and frequency samples f_j. Vector $\mathbf{k}_n$ contains excitation k-space samples ($k_{x,n}, k_{y,n}$,$k_{\mathrm{f},n}$). For prewinding pulses, $k_{\mathrm{f},n}$ is simply the time-reversed vector for pulse length τ: $k_{\mathrm{f},n} = t_n - \tau$. The matrix $\mathbf{A}$ is very large so we use Nonuniform Fast Fourier Transform (NUFFT) operations to perform matrix vector multiplications involving $\mathbf{A}$ [59].

Unlike traditional STA designs that penalize RF power with a regularization parameter [1], optimization problem Eq. (4.12) directly constrains the deposited RF power $p_{\max}$. We

set the constraint $p_{\max}$ to a constant with units W/kg chosen conservatively from SAR estimates from previous experiments using spectral pulses and the STFR sequence with the same TR. C_{SAR} is a measured constant that converts the integrated RF pulse $||\mathbf{b}||_2^2 \Delta t$ from $\mathrm{G}^2 \cdot \mathrm{ms}$ to W/kg for a particular TR. We compute a 2D spectral-spatial pulse efficiently by minimizing Eq. (4.12) using approximately 100 iterations of FISTA [32].

Assuming a smoothly varying field map, we downsampled the x and y dimensions of the field map from 120×120 by a factor of 4 in forming (x_j, y_j), and sampled off-resonance frequencies every 10 Hz. Spatial downsampling has negligible effects on the RF excitation accuracy given the low resolution excitation k-space trajectories chosen for these pulse designs. The NUFFT matrix multiplication in Eq. (4.12) was implemented with the Michigan Image Reconstruction Toolbox, available for download at http://web.eecs.umich.edu/∼fessler/.

4.3.2 Experiments

We performed the following experiments to examine if spectral-spatial prewinding pulses can recover larger off-resonance bandwidths than purely spectral pulses. This was evaluated via simulation and experimentally in a gel phantom and the human brain in vivo. We also simulated a non-prewinding hard pulse and compared to the spectral and spectral-spatial pulses in Appendix A Section 2. Table A2.1 and Figures A2.1-A2.3 show these results.

4.3.2.1 RF Pulse and Pulse Sequences

We performed all experiments with a birdcage single channel T/R head coil on a 3T GE MR750 scanner (GE Healthcare, Waukesha, WI). Using a field map from a 2D slice, we designed 3 ms tip-down and tip-up pulses for the STFR sequence (TE/TR=3.648 ms/14.08 ms), where TE is measured from the end of the RF pulse. For phantom experiments, we used a target flip angle of α=19.6°. For in vivo brain imaging we used target α=15.8° based on previous literature findings showing optimal grey matter signal for STFR [6]. For the gel phantom, we set $p_{\max}$=2.2 W/kg using C_{SAR}=525 W/kg/G^2/ms, and chose a stricter constraint of $p_{\max}$=2.1 W/kg using C_{SAR}=700 W/kg/G^2/ms for the in-vivo brain scan where we assumed increased RF coil loading. These are conservative power constraints below the SAR limitations within the head. The stopping criterion for RF pulse convergence in the FISTA algorithm was set so that the maximum difference between iterations normalized by the initialization pulse was less than 2^{-12} times the peak RF amplitude limit of 0.2 Gauss.

We designed the RF pulses with MATLAB (The MathWorks, Natick, MA). All pulses were designed online after the field map acquisition. The total time to estimate the object

field map, design the RF pulses, and export the files to the scanner was less than 5 min.

4.3.2.2 Phantom Scans

For phantom scans, we taped a small piece of metal from a paperclip to the surface of a homogenous gel ball phantom to induce B0 inhomogeneity. Two GRE scans (TE1/TE2/TR1/TR2/FA= 2.042 ms/4.342 ms/5.58 ms/7.88 ms/8.2°) with distinct echo times (TE1,TE2) were collected using a 3D readout with FOV = 240 mm × 240 mm × 296 mm and matrix size 120 × 120 × 74. We used these two scans to generate a B0 field map that was estimated using the regularized method described in [60]. We then chose a 2D slice with an off-resonance range of just over ±100 Hz.

For the phantom experiment, we designed two types of spectral pulses: one that was designed to cover the full bandwidth of off-resonance frequencies in the 2D field map, and another that centered the design at the mean off-resonance frequency and was restricted to the empirical bandwidth threshold from Eq. (4.3). For a readout FOV = 240 mm, matrix size 256, and ± 31.25 kHz BW, the minimum free precession time was $\mathrm{T}_{\mathrm{free}}$=7.296 ms which gives a spectral prewinding bandwidth cutoff of ±68.5 Hz.

In preliminary simulations (not shown) we explored a variety of excitation k-space trajectories and compared their performance in simulation. We found that revisiting k-space locations multiple times offers more complete coverage of k-space, albeit at lower spatial resolution, which is desirable for pulses with both spectral and spatial profiles. Based on these initial findings, we designed spectral-spatial pulses using two 2D variable density spiral (VDS) excitation k-space trajectories: one with three alternating spirals with $k_{xy,\max}$=0.13 $\frac{\text{cycles}}{\text{cm}}$ and the other with two alternating spirals with $k_{xy,\max}$=0.20 $\frac{\text{cycles}}{\text{cm}}$. For all spectral-spatial pulses we defined the weighting function $w(x, y, f)$ with L =25 Hz (Eq. (4.5)). Therefore in total, two sets of spectral and two sets of spectral-spatial prewinding tip-down/tip-up pulses were designed for the phantom.

Experimental magnitude and phase images are presented using the STFR sequence. Phase images are computed by subtracting the inherent coil phase estimated from the TE1 GRE scan used for field map acquisition.

4.3.2.3 Human Scans

We also designed spectral and spectral-spatial pulses for a human volunteerFLs brain. Again, the first step was to obtain a field map with two GRE scans (using the same TE and TR values used in the phantom experiment) and select for pulse design a 2D slice with a significant range of off-resonance. Here, pulse design characteristics (spectral design

bandwidth and excitation trajectory) were selected from the best spectral and best spectral-spatial pulses used in the phantom experiment, based on their quantitative performance metrics defined in the section below. The best spectral pulse was the pulse designed over the full off-resonance bandwidth, and the best spectral-spatial pulse used a VDS trajectory with two alternating spirals and $L = 25$ Hz. Just two pulses were designed to limit scan time for the human volunteer. We also compare the spectral and spectral-spatial pulses to a simulated non-prewinding "hard" pulse with the same design flip angle α=15.8° and TE=3.648 ms.

4.3.3 Performance Metrics

Quantifying the excitation performance of the spectral-spatial RF pulses is nontrivial because we aim to match a particular phase and magnitude pattern across both spatial and spectral dimensions. Nevertheless the definitions of these metrics are critical for comparing various prewinding pulses. We measured the performance by simulating the magnetization for each voxel within our region of interest (ROI) at each frequency within the design bandwidth at that location. Magnetization values were computed in two ways: using STA approximation of the magnetization $\mathbf{m}_{\mathrm{STA}} \approx \mathbf{Ab}$ and the magnetization obtained from full Bloch simulation, $\mathbf{m}_{\mathrm{Bloch}}$, with relaxation effects ignored (T1 and T2 set to infinity). Our Bloch simulation results agreed with the STA approximation, so we report only the Bloch simulation results here. We conducted the multidimensional Bloch simulation on a voxel-by-voxel basis, accounting for within-voxel spin dephasing. We used a Gaussian model of the intravoxel frequency distribution [61] with a standard deviation of σ=25 Hz (to reflect mean literature R2* values [62], [63]) and a simulation spread of $\pm 3\sigma$. We evaluated the magnetization at the echo time TE.

At TE, ideally all spins within each voxel should rephase and produce uniform excitation at the target flip angle α. To quantify excitation accuracy we calculated the Excitation Normalized Root Mean Squared Error (NRMSE)

$$\text{Excitation NRMSE} = \frac{\sqrt{\frac{1}{N_{\mathrm{xy}}} \sum_{j=1}^{N_{xy}} \left| \sum_{n=1}^{N_{\mathrm{g}}} g_n m_{n,j} - \sin(\alpha) \right|^2}}{\sin(\alpha)} \quad . \tag{4.7}$$

Here the length N_{g} vector $\mathbf{g}$ contains the weights defined by the Gaussian model of intravoxel frequency distribution around the resonance frequency at each voxel; $\mathbf{g}$ is normalized to sum to 1. We compare Bloch simulation magnetization to the unitless target magnitude $\sin(\alpha)$. Under the STA approximation, $\sin(\alpha)$ is roughly equal to α.

Another quality metric for the pulse is transverse magnetization uniformity, or how well

off-resonance spins within the spectral bandwidth come to the same mean magnetization. Using the simulated magnetization, we computed the mean magnitude across frequencies for each voxel, and finally defined the total mean and percent deviation of the magnetization magnitude as

$$\bar{m} = \frac{1}{N_{\text{xy}}} \sum_{j=1}^{N_{\text{xy}}} \left(\sum_{n=1}^{N_{\text{g}}} g_n \left| m_{n,j} \right| \right) \tag{4.8}$$

and

$$\%\sigma = \frac{\sqrt{\frac{1}{N_{\text{xy}}} \sum_{j=1}^{N_{\text{xy}}} (\sum_{n=1}^{N_{\text{g}}} g_n \left| m_{n,j} \right|) - \bar{m})^2}}{\bar{m}} \times 100\% \ . \tag{4.9}$$

We also calculated the NRMSE of the excitation *magnitude* compared to the target transverse magnetization:

$$\text{Magnitude NRMSE} = \frac{\sqrt{\frac{1}{N_{\text{xy}}} \sum_{j=1}^{N_{\text{xy}}} (|\sum_{n=1}^{N_{\text{g}}} g_n m_{n,j}| - \sin(\alpha))^2}}{\sin(\alpha)} \ . \tag{4.10}$$

Finally, we also calculate the phase error to evaluate the effectiveness of "prewinding". The desired phase of the magnetization will be zero at the echo time. The phase Root Mean Squared Error (RMSE) is

$$\text{Phase RMSE} = \sqrt{\frac{1}{N_{\text{xy}}} \sum_{j=1}^{N_{\text{xy}}} \left(\angle \sum_{n=1}^{N_{\text{g}}} g_n m_{n,j} \right)^2} \ . \tag{4.11}$$

In conjunction, these various performance metrics provide insight into prewinding pulse performance in simulation, identifying how well pulses perform and under what conditions they might fail. for supporting information provided with this work that was accepted into *Magnetic Resonance in Medicine* in 2017 [9]. Table A1.1 and Supporting Figure A1.1 explain the supplementary experiments; Table A1.2 and Figures A1.2-A1.3 present the results.

4.4 Methods

4.4.1 RF Pulse Design

Both purely spectral [15] and spectral-spatial pulses were designed using the STA approximation [22] for a target 2D slice. The STA approximation facilitates RF pulse design by establishing a linear Fourier relationship between RF waveform and transverse magnetization [1]. The tip-down pulse design target pattern $\mathbf{d}$ was defined for spectral pulses by Eq. (4.2) and for spectral-spatial pulses by Eq. (4.4), where off-resonance frequencies $\mathbf{f} = [f_1, ..., f_{N_\mathrm{f}}]^T$ were sampled from the off-resonance range measured in a field map. The tip-up pulses used simulated magnetization magnitude and phase at the end of free precession to assign the magnitude and phase of the target tip-up pattern [55]. The spectral-spatial pulse design used gradients played out during the RF pulse that trace out a variable density spiral k-space trajectory repeated multiple times. The speed and resolution of this trajectory permitted time between spirals to be spent at k-space center where we found that large amounts of RF energy are deposited.

We design the RF pulse by solving the STA constrained optimization problem:

$$\begin{aligned} \hat{\mathbf{b}} &= \underset{\mathbf{b}}{\operatorname{argmin}} \ ||\mathbf{Ab} - \mathbf{d}||_{\mathbf{W}}^2 \\ \text{s.t.} \ \ & C_{\mathrm{SAR}}||\mathbf{b}||_2^2 \Delta t \leq p_{\max} \end{aligned} \tag{4.12}$$

where $\hat{\mathbf{b}}$ is the optimized RF pulse, $\mathbf{W}$ is the diagonal weighting matrix composed of samples of weighting function $w(x, y, f)$ (Eq. (4.5)), C_{SAR} is a conversion constant, and $\mathbf{A}$ is the small tip system matrix with elements $a_{j,n} = i\gamma M_0 e^{2\pi i(\mathbf{r}_j \cdot \mathbf{k}_n)} \Delta t$. Here, vector $\mathbf{r}_j = (x_j, y_j, f_j)$ contains spatial location samples (x_j, y_j) and frequency samples f_j. Vector $\mathbf{k}_n$ contains excitation k-space samples $(k_{x,n}, k_{y,n}, k_{\mathrm{f},n})$. For prewinding pulses, $k_{\mathrm{f},n}$ is simply the time-reversed vector for pulse length τ: $k_{\mathrm{f},n} = t_n - \tau$. The matrix $\mathbf{A}$ is very large so we use Nonuniform Fast Fourier Transform (NUFFT) operations to perform matrix vector multiplications involving $\mathbf{A}$ [59].

Unlike traditional STA designs that penalize RF power with a regularization parameter [1], optimization problem Eq. (4.12) directly constrains the deposited RF power $p_{\max}$. We set the constraint $p_{\max}$ to a constant with units W/kg chosen conservatively from SAR estimates from previous experiments using spectral pulses and the STFR sequence with the same TR. C_{SAR} is a measured constant that converts the integrated RF pulse $||\mathbf{b}||_2^2 \Delta t$ from $\mathrm{G}^2 \cdot \mathrm{ms}$ to W/kg for a particular TR. We compute a 2D spectral-spatial pulse efficiently by minimizing Eq. (4.12) using approximately 100 iterations of FISTA [32].

Assuming a smoothly varying field map, we downsampled the x and y dimensions of

the field map from 120×120 by a factor of 4 in forming (x_j, y_j), and sampled off-resonance frequencies every 10 Hz. Spatial downsampling has negligible effects on the RF excitation accuracy given the low resolution excitation k-space trajectories chosen for these pulse designs. The NUFFT matrix multiplication in Eq. (4.12) was implemented with the Michigan Image Reconstruction Toolbox, available for download at http://web.eecs.umich.edu/ fessler/.

4.4.2 Experiments

We performed the following experiments to examine if spectral-spatial prewinding pulses can recover larger off-resonance bandwidths than purely spectral pulses. This was evaluated via simulation and experimentally in a gel phantom and the human brain in vivo. We also simulated a non-prewinding hard pulse and compared to the spectral and spectral-spatial pulses in Appendix A Section 2. Table A2.1 and Figures A2.1-A2.3 show these results.

4.4.2.1 RF Pulse and Pulse Sequences

We performed all experiments with a birdcage single channel T/R head coil on a 3T GE MR750 scanner (GE Healthcare, Waukesha, WI). Using a field map from a 2D slice, we designed 3 ms tip-down and tip-up pulses for the STFR sequence (TE/TR=3.648 ms/14.08 ms), where TE is measured from the end of the RF pulse. For phantom experiments, we used a target flip angle of α=19.6°. For in vivo brain imaging we used target α=15.8° based on previous literature findings showing optimal grey matter signal for STFR [6]. For the gel phantom, we set $p_{\max}$=2.2 W/kg using C_{SAR}=525 W/kg/G^2/ms, and chose a stricter constraint of $p_{\max}$=2.1 W/kg using C_{SAR}=700 W/kg/G^2/ms for the in-vivo brain scan where we assumed increased RF coil loading. These are conservative power constraints below the SAR limitations within the head. The stopping criterion for RF pulse convergence in the FISTA algorithm was set so that the maximum difference between iterations normalized by the initialization pulse was less than 2^{-12} times the peak RF amplitude limit of 0.2 Gauss.

We designed the RF pulses with MATLAB (The MathWorks, Natick, MA). All pulses were designed online after the field map acquisition. The total time to estimate the object field map, design the RF pulses, and export the files to the scanner was less than 5 min.

4.4.2.2 Phantom Scans

For phantom scans, we taped a small piece of metal from a paperclip to the surface of a homogenous gel ball phantom to induce B0 inhomogeneity. Two GRE scans (TE1/TE2/TR1/TR2/FA= 2.042 ms/4.342 ms/5.58 ms/7.88 ms/8.2°) with distinct echo times

(TE1,TE2) were collected using a 3D readout with FOV = 240 mm × 240 mm × 296 mm and matrix size 120 × 120 × 74. We used these two scans to generate a B0 field map that was estimated using the regularized method described in [60]. We then chose a 2D slice with an off-resonance range of just over ±100 Hz.

For the phantom experiment, we designed two types of spectral pulses: one that was designed to cover the full bandwidth of off-resonance frequencies in the 2D field map, and another that centered the design at the mean off-resonance frequency and was restricted to the empirical bandwidth threshold from Eq. (4.3). For a readout FOV = 240 mm, matrix size 256, and ± 31.25 kHz BW, the minimum free precession time was $\mathrm{T}_{\mathrm{free}}$=7.296 ms which gives a spectral prewinding bandwidth cutoff of ±68.5 Hz.

In preliminary simulations (not shown) we explored a variety of excitation k-space trajectories and compared their performance in simulation. We found that revisiting k-space locations multiple times offers more complete coverage of k-space, albeit at lower spatial resolution, which is desirable for pulses with both spectral and spatial profiles. Based on these initial findings, we designed spectral-spatial pulses using two 2D variable density spiral (VDS) excitation k-space trajectories: one with three alternating spirals with $k_{xy,\max}$=0.13 $\frac{\text{cycles}}{\text{cm}}$ and the other with two alternating spirals with $k_{xy,\max}$=0.20 $\frac{\text{cycles}}{\text{cm}}$. For all spectral-spatial pulses we defined the weighting function $w(x, y, f)$ with L =25 Hz (Eq. (4.5)). Therefore in total, two sets of spectral and two sets of spectral-spatial prewinding tip-down/tip-up pulses were designed for the phantom.

Experimental magnitude and phase images are presented using the STFR sequence. Phase images are computed by subtracting the inherent coil phase estimated from the TE1 GRE scan used for field map acquisition.

4.4.2.3 Human Scans

We also designed spectral and spectral-spatial pulses for a human volunteerFLs brain. Again, the first step was to obtain a field map with two GRE scans (using the same TE and TR values used in the phantom experiment) and select for pulse design a 2D slice with a significant range of off-resonance. Here, pulse design characteristics (spectral design bandwidth and excitation trajectory) were selected from the best spectral and best spectral-spatial pulses used in the phantom experiment, based on their quantitative performance metrics defined in the section below. The best spectral pulse was the pulse designed over the full off-resonance bandwidth, and the best spectral-spatial pulse used a VDS trajectory with two alternating spirals and L = 25 Hz. Just two pulses were designed to limit scan time for the human volunteer. We also compare the spectral and spectral-spatial pulses to a simulated non-prewinding "hard" pulse with the same design flip angle α=15.8° and

TE=3.648 ms.

4.4.3 Performance Metrics

Quantifying the excitation performance of the spectral-spatial RF pulses is nontrivial because we aim to match a particular phase and magnitude pattern across both spatial and spectral dimensions. Nevertheless the definitions of these metrics are critical for comparing various prewinding pulses. We measured the performance by simulating the magnetization for each voxel within our region of interest (ROI) at each frequency within the design bandwidth at that location. Magnetization values were computed in two ways: using STA approximation of the magnetization $\mathbf{m}_{\mathrm{STA}} \approx \mathbf{Ab}$ and the magnetization obtained from full Bloch simulation, $\mathbf{m}_{\mathrm{Bloch}}$, with relaxation effects ignored (T1 and T2 set to infinity). Our Bloch simulation results agreed with the STA approximation, so we report only the Bloch simulation results here. We conducted the multidimensional Bloch simulation on a voxel-by-voxel basis, accounting for within-voxel spin dephasing. We used a Gaussian model of the intravoxel frequency distribution [61] with a standard deviation of σ=25 Hz (to reflect mean literature R2* values [62], [63]) and a simulation spread of $\pm 3\sigma$. We evaluated the magnetization at the echo time TE.

At TE, ideally all spins within each voxel should rephase and produce uniform excitation at the target flip angle α. To quantify excitation accuracy we calculated the Excitation Normalized Root Mean Squared Error (NRMSE)

$$\text{Excitation NRMSE} = \frac{\sqrt{\frac{1}{N_{\mathrm{xy}}} \sum_{j=1}^{N_{xy}} \left| \sum_{n=1}^{N_{\mathrm{g}}} g_n m_{n,j} - \sin(\alpha) \right|^2}}{\sin(\alpha)} \quad . \tag{4.13}$$

Here the length N_{g} vector $\mathbf{g}$ contains the weights defined by the Gaussian model of intravoxel frequency distribution around the resonance frequency at each voxel; $\mathbf{g}$ is normalized to sum to 1. We compare Bloch simulation magnetization to the unitless target magnitude $\sin(\alpha)$. Under the STA approximation, $\sin(\alpha)$ is roughly equal to α.

Another quality metric for the pulse is transverse magnetization uniformity, or how well off-resonance spins within the spectral bandwidth come to the same mean magnetization. Using the simulated magnetization, we computed the mean magnitude across frequencies for each voxel, and finally defined the total mean and percent deviation of the magnetization magnitude as

$$\bar{m} = \frac{1}{N_{\mathrm{xy}}} \sum_{j=1}^{N_{\mathrm{xy}}} \left(\sum_{n=1}^{N_{\mathrm{g}}} g_n \left| m_{n,j} \right| \right) \tag{4.14}$$

and

$$\%\sigma = \frac{\sqrt{\frac{1}{N_{\text{xy}}}\sum_{j=1}^{N_{\text{xy}}}(\sum_{n=1}^{N_{\text{g}}} g_n\,|m_{n,j}|) - \bar{m})^2}}{\bar{m}} \times 100\% \quad . \tag{4.15}$$

We also calculated the NRMSE of the excitation *magnitude* compared to the target transverse magnetization:

$$\text{Magnitude NRMSE} = \frac{\sqrt{\frac{1}{N_{\text{xy}}}\sum_{j=1}^{N_{\text{xy}}}(|\sum_{n=1}^{N_{\text{g}}} g_n m_{n,j}| - \sin(\alpha))^2}}{\sin(\alpha)} \quad . \tag{4.16}$$

Finally, we also calculate the phase error to evaluate the effectiveness of "prewinding". The desired phase of the magnetization will be zero at the echo time. The phase RMSE is

$$\text{Phase RMSE} = \sqrt{\frac{1}{N_{\text{xy}}}\sum_{j=1}^{N_{\text{xy}}}\left(\angle\sum_{n=1}^{N_{\text{g}}} g_n m_{n,j}\right)^2} \quad . \tag{4.17}$$

In conjunction, these various performance metrics provide insight into prewinding pulse performance in simulation, identifying how well pulses perform and under what conditions they might fail.

4.5 Results

4.5.1 Phantom Scans

Figure 4.2 shows the experimental field map used for spectral and spectral-spatial RF pulse design for the phantom scans. This figure also shows designed tip-down RF pulse and gradient waveforms for the two spectral (full bandwidth, theoretical bandwidth) and two spectral-spatial (3 spirals, 2 spirals) pulses. The theoretical spectral bandwidth limit is set to $\pm$68.5 Hz by the empirical relationship described in Eq. (4.3) while the entire range of off-resonance in this slice is $\approx$ 218 Hz. All RF pulses designed were limited by the power constraint set in the optimization problem. By simulating on-resonance spins, this led to a median simulated flip angle of α=14.8° and 15.3° for the spectral pulses with full and theoretical bandwidths, respectively, and α=17.1° and 17.9° for the spectral-spatial pulses with 3 and 2 spirals respectively (compared to the target value of 19.6°).

Figure 4.3 shows the Bloch simulated magnetization in the phantom normalized by

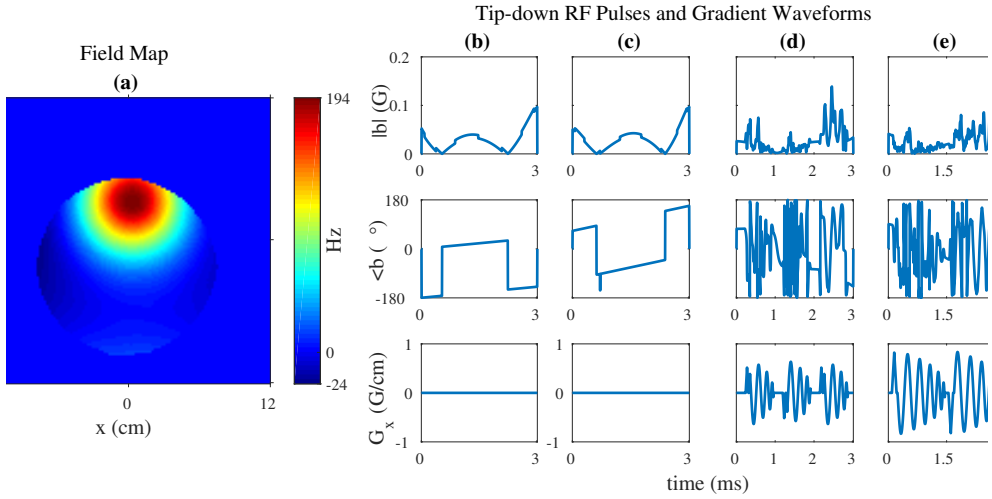

Figure 4.2: (a) Ball phantom field map used to design spectral and spectral-spatial prewinding pulses. (b-e) Tip-down RF pulse magnitude, phase, and excitation gradients for spectral pulses with (b) $\pm$68.5Hz target bandwidth and (c) full field map off-resonance bandwidth, and 2D spectral-spatial pulses with (d) 3VDS excitation trajectory and (e) 2VDS excitation trajectory. Only the G_x waveform is shown. Further description of these VDS trajectories is found in the Methods section.

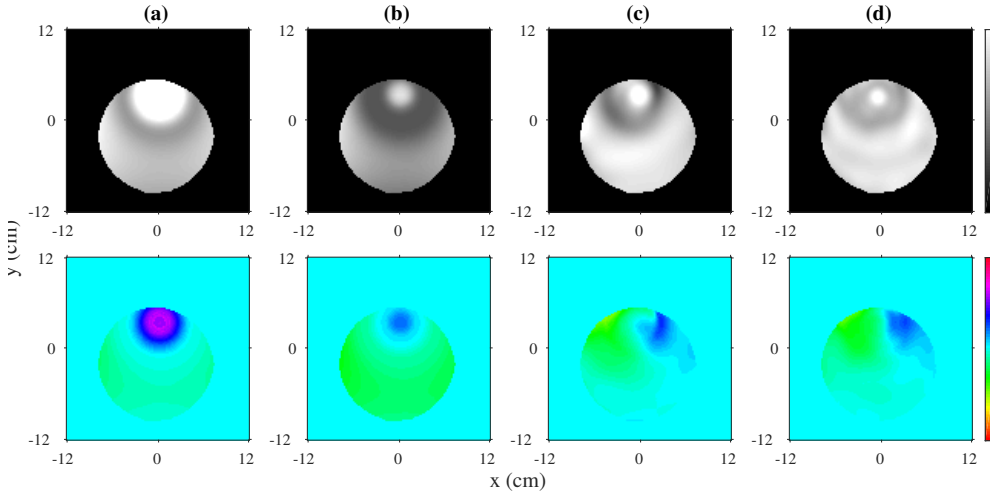

Figure 4.3: Bloch simulated magnetization magnitude (top row) and phase (bottom row) at TE for spectral pulses with (a) $\pm$68.5 Hz target bandwidth and (b) full field map off-resonance bandwidth, and 2D spectral-spatial pulses with (c) 3 variable density spiral (VDS) excitation trajectory and (d) 2VDS excitation trajectory. The magnitude images are more uniform and the phase images are closer to zero in the spectral-spatial simulations (c,d).

the target magnitude. Qualitatively, the simulations show a uniform magnetization magnitude slightly below 1. The RF pulses cannot exactly meet the nominal flip angle due to the active power constraint. In these simulations we also see roughly uniform, zero magnetization phase except for areas of high off-resonance by the paperclip. The phase from the purely spectral pulse designed over the theoretical bandwidth (Fig. 3a) performs particularly poorly, while the other spectral pulse and both spectral-spatial pulses have closer-to-zero phase.

Table 4.1 reports the performance metrics under Bloch simulation for these four designs. The spectral-spatial pulses outperform the purely spectral pulses overall. Spectral pulses suffer from large phase errors seen in the excitation NRMSE (0.81 and 0.66) and phase RMSE (33.3° and 28.5°). The spectral-spatial pulses have lower performance metric error while still maintaining high mean magnitude, especially for the spectral-spatial pulse using a two-spiral variable density spiral excitation trajectory. This pulse produces the lowest error in every case.

Table 4.1: Bloch simulation performance metrics comparing two purely spectral and two spectral-spatial RF pulse designs for a phantom with paper clip susceptibility. The target flip angle α = 19.6° is approximately 0.34 radians. The best results are in bold.

Pulse Design Trajectory	Excitation NRMSE	Phase RMSE (°)	Mean Mag.	% St. Dev.	Magnitude NRMSE
Spectral BW-limited, ±68.5 Hz	0.81	33.3	**0.30**	36.6	0.34
Spectral full BW	0.66	28.5	0.18	26.6	0.48
Spectral-spatial 3 VDS	0.41	23.4	0.28	18.9	0.24
Spectral-spatial 2 VDS	**0.38**	**23.0**	0.29	**10.6**	**0.18**

Figure 4.4 shows the experimental magnitude and phase images of the phantom for the four RF pulses. Just like in simulation, these results demonstrate the improved quality of spectral-spatial pulses compared to spectral pulses. The spectral-spatial magnitude images exhibit less signal loss than the purely spectral magnitude images and the phase images are closer to zero for spectral-spatial pulses, indicating more accurate prephasing.

4.5.2 Human Scans

The field map for the human brain slice used for pulse design had an off-resonance range of about ±85Hz (Fig. 4.5). Figure 4.5 also shows the k-space of phase induced by off-resonance with overlay of excitation k-space trajectory, the RF and gradient waveforms for the spectral and spectral-spatial pulses designed for this slice, and simulated relative complex error ($|\frac{m_{xy}}{\sin\alpha} - 1|$) for the spectral-spatial pulse as a function of one spatial dimension and all frequencies. In this case just one spectral and one spectral-spatial pulse were designed. Again, the RF pulses were limited by the power constraint, and the median simulated on-resonance flip angle was α=8.6° and 14.9° for the spectral and spectral-spatial pulses, respectively. Figure 5b was computed as the 2D Fourier Transform of $\exp(-2\pi i \mathrm{TE}\Delta f(x,y))$. In this subfigure, we see that the 2VDS excitation captures the majority of the field map energy predominantly at the k-space center.

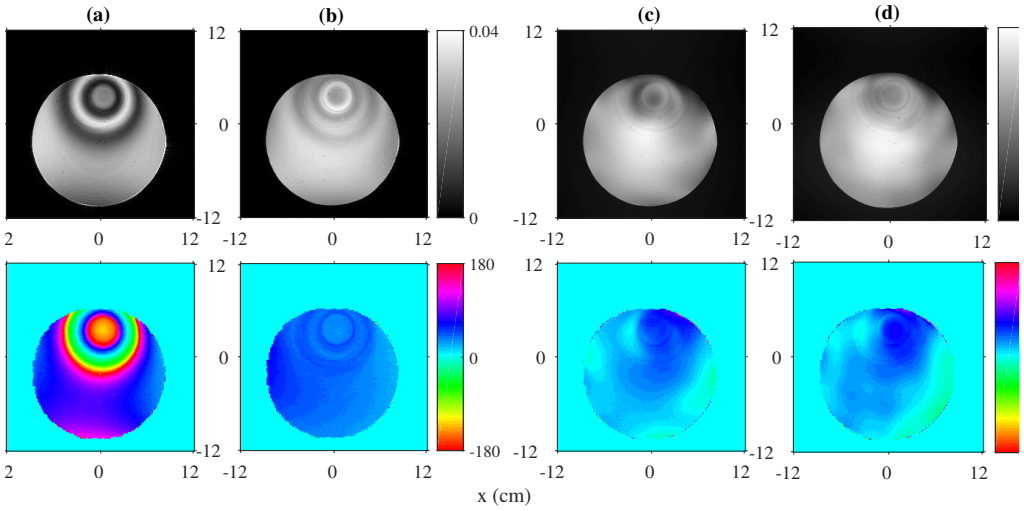

Figure 4.4: Experimental magnitude (top row) and phase (bottom row) STFR images for spectral pulses with (a) $\pm$68.5 Hz target bandwidth and (b) full field map off-resonance bandwidth, and 2D spectral-spatial pulses with (c) 3VDS excitation trajectory and (d) 2VDS excitation trajectory. Magnitude images are scaled differently for the spectral images and the spectral-spatial images to facilitate visual comparison. As in the simulation, the magnitude images are more uniform and the phase images are closer to zero for spectral-spatial pulses.

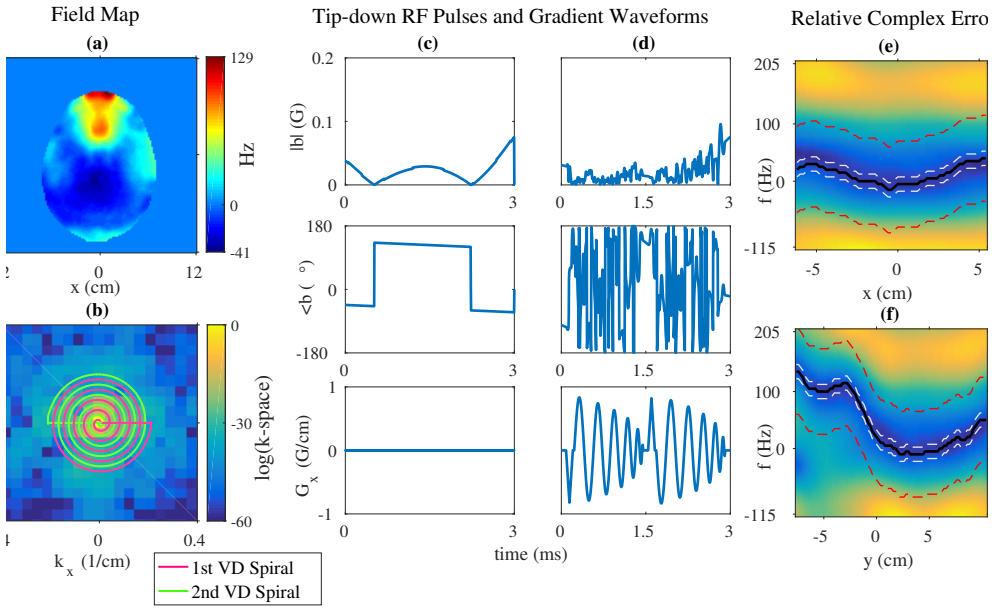

Figure 4.5: (a) Human brain field map used to design spectral and spectral-spatial prewinding pulses and (b) logarithm of zoomed k-space of phase induced by off-resonance with overlay of excitation k-space trajectory, 2VDS. (c-d) Tip-down RF pulse magnitude, phase, and G_x excitation gradients for (c) a spectral pulse designed with full field map off-resonance bandwidth and (d) a 2D spectral-spatial pulse designed with the same 2VDS excitation trajectory used in the phantom experiments. (e-f) Relative complex error $|\frac{m_{xy}}{\sin\alpha} - 1|$ for the spectral-spatial pulse as a function of frequency and 1D line profile across (e) all x at y =2.8 cm and across (f) all y at x =0.2 cm. The dashed white lines represent the L = 25 Hz used as the local bandwidth for the spectral-spatial pulse, and the dashed red lines represent the $\pm 3\sigma$ =75 Hz bandwidth used in Bloch simulation. Further examples of these plots are found in Appendix A Section A.2.

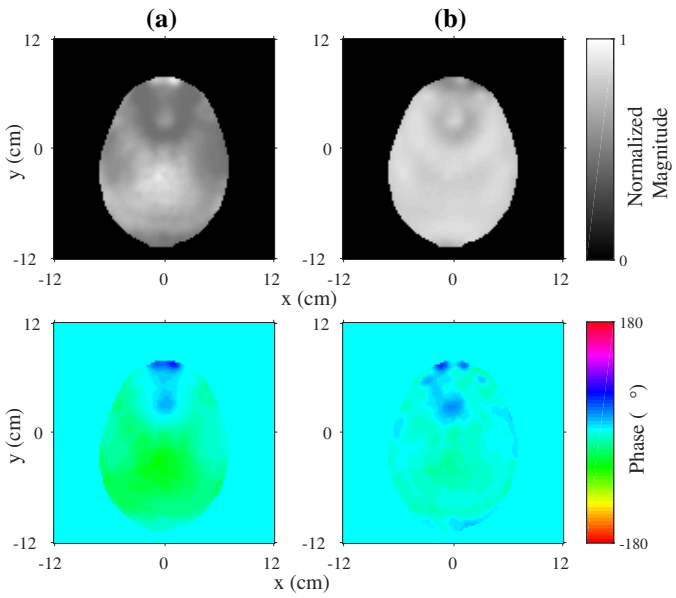

Figure 4.6: Bloch simulated magnitude (top row) and phase (bottom row) at TE for (a) a purely spectral tipdown pulse and (b) a spectral-spatial tipdown pulse designed for the 2D field map in Fig. 4.5(a). The spectral-spatial pulse suffers from less signal loss and obtains a flatter phase closer to zero.

Figure 4.6 displays the Bloch simulated magnetization for the two prewinding RF pulse designs and Table 4.2 reports performance metrics. Again, the spectral-spatial pulse outperforms the purely spectral pulse for all metrics. Notably, the excitation NRMSE and phase RMSE drop from 0.54 and 25.2° in the spectral case to 0.18 and 7.0° in the spectral-spatial case, respectively.

Table 4.2: Bloch simulation performance metrics comparing purely spectral and spectral-spatial RF pulses designed using a 2D slice of a human brain field map. The target flip angle $\alpha = 15.8°$ is approximately 0.28 radians. The best results are in bold.

Pulse Design Trajectory	Excitation NRMSE	Phase RMSE (°)	Mean Mag.	% St. Dev.	Magnitude NRMSE
Spectral full BW	0.54	25.2	0.17	19.6	0.39
Spectral-spatial 2 VDS	**0.18**	**7.0**	**0.24**	**7.7**	**0.15**

Additional intuition about pulse performance can be gained by plotting error as a func-

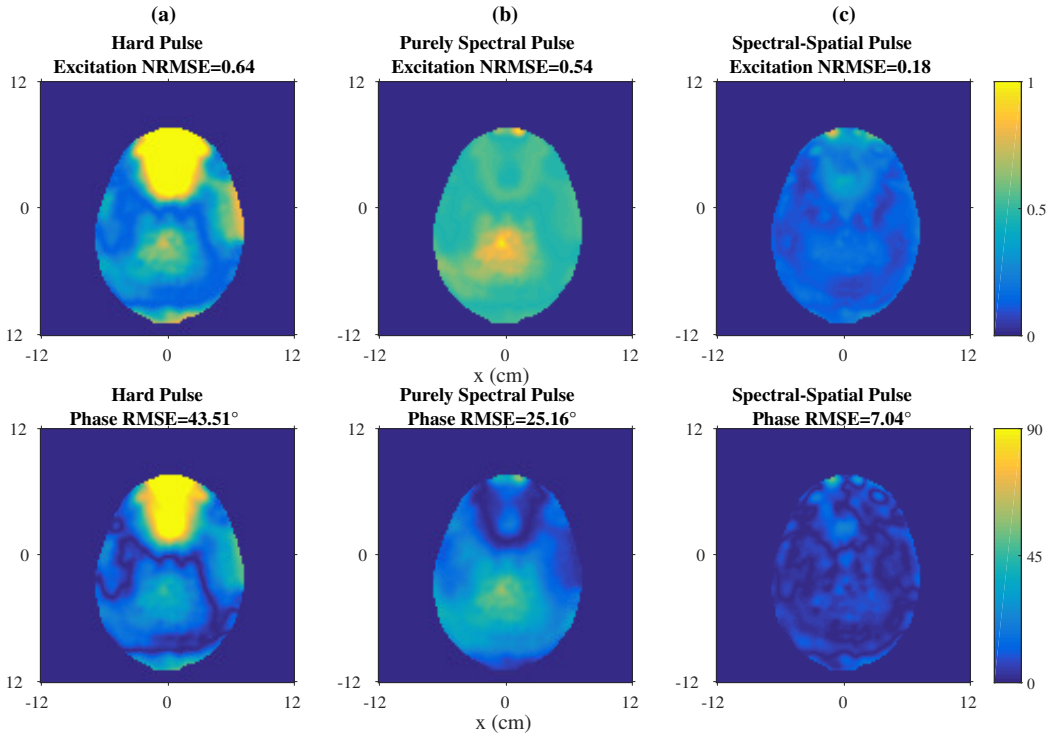

Figure 4.7: Simulated error as a function of space. Excitation root squared error (top row) and phase root squared error (bottom row) across a range of intravoxel frequencies (Gaussian distribution over $[-3\sigma : 3\sigma]$ with σ =25 Hz) over all spatial locations x, y for (a) the hard pulse, (b) the purely spectral pulse, and (c) the spectral-spatial pulse. The excitation and phase errors are lowest in the spectral-spatial case, and the same is true for the overall excitation NRMSE and phase RMSE.

tion of spatial location. Figure 4.7 shows excitation and phase root squared error combined across all simulated frequencies as a function of spatial location for the simulated hard pulse, purely spectral pulse, and spectral-spatial pulse. In this plot, we can see that the hard pulse performs poorly, the spectral pulse performs moderately well, and the spectral-spatial pulse performs best.

Figure 4.8 shows the in vivo experimental magnitude and phase images for the spectral and spectral-spatial RF pulse. The spectral-spatial pulse magnitude image has less signal intensity variation than the purely spectral pulse, while the spectral-spatial phase image is also closer to uniformly zero. Therefore, qualitatively the spectral-spatial pulse has better off-resonance prewinding capability than the spectral pulse.

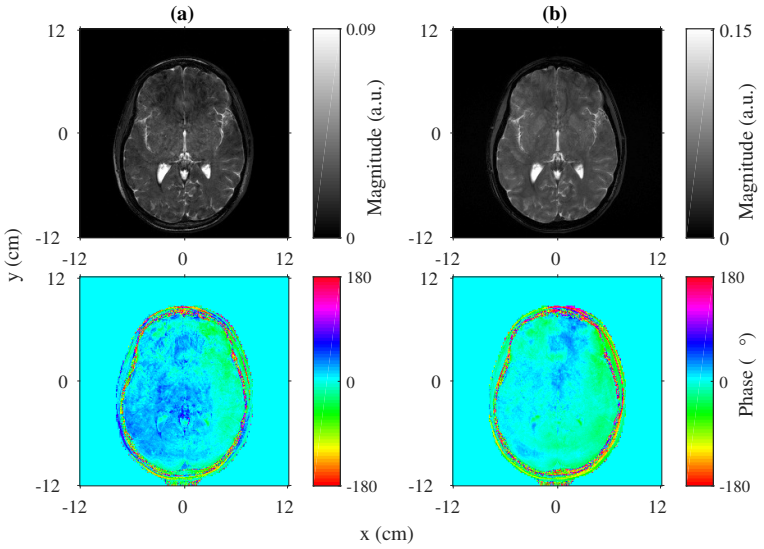

Figure 4.8: Experimental magnitude (top row) and phase (bottom row) images for (a) a spectral pulse designed over full field map off-resonance bandwidth and (b) a 2D spectral-spatial pulse designed with 2VDS excitation trajectory. Again, magnitude images are scaled differently for the spectral images and the spectral-spatial images to help visual comparison. The spectral-spatial pulse yields more uniform magnitude and closer to zero phase.

4.6 Discussion

The principal idea behind spectral-spatial pulses is that the combination of spectral prewinding with spatial encoding of off-resonance patterns using magnetic field gradients allows for improved signal rephasing compared to purely spectral pulses alone, as shown in Fig. 4.1. This is useful because purely spectral pulses are limited in the off-resonance bandwidth that can they can recover, which is related to sometimes non-negotiable pulse sequence parameters such as flip angle and echo time. We believe this new pulse has useful applications in the human brain, where off-resonance can vary smoothly but cover a large range (bandwidth). This Chapter demonstrates the utility of spectral-spatial pulses using a phantom and in vivo brain example with the STFR sequence. The STFR sequence is useful for tailored RF pulses because the unique tip-up pulse helps accommodate any magnetization error between the target pattern and Bloch simulated magnetization of the tip-down pulse. This makes spectral-spatial prewinding pulses a good match to the STFR pulse sequence.

In the phantom experiment, Fig. 4.3 and Table 4.1 show dramatic qualitative and quantitative improvement when comparing spectral-spatial to purely spectral prewinding pulses. In particular, the excitation NRMSE which captures the pulse's ability to rephase intravoxel spin isochromats with spectral prewinding, is roughly halved for both spectral-spatial excitation trajectory designs. Furthermore, the experimental images (Fig. 4.4) confirm the simulation results and the spectral-spatial pulses create more uniform images for the same flip angle design. The presence of slight, darkened signal loss regions in the spectral-spatial phantom images might reflect the limited spatial resolution of the spectral-spatial excitation k-space trajectory.

The in vivo experiments exhibited similar results. Again, the spectral-spatial pulse outperformed the purely spectral pulse as highlighted in Fig. 4.6 and Table 4.2, with excitation NRMSE again reducing to half. There are significant visual differences between the in vivo images (Fig. 4.8). The spectral-spatial pulse produces a brighter, more uniform magnitude image. The spectral-spatial pulse magnitude image does not have notable areas of signal loss, in contrast to the darker rostral region in the spectral magnitude image. In addition to prewinding performance improvements, some of the brightness differences between these two pulses might also be attributed to the active power constraint in the RF pulse design which may inhibit the RF pulse from realizing the nominal flip angle. Both magnitude images exhibit bright cerebrospinal fluid (CSF) that is typical for the mixed T2/T1 contrast of steady-state sequences like STFR andbSSFP [6]. Additionally, the in vivo phase images also illustrate the improved performance of spectral-spatial pulses. The phase at TE is

noticeably more uniform in the spectral-spatial pulse phase image compared to the purely spectral phase image.

Despite their enhanced performance compared to purely spectral pulses, there are a few limitations to spectral-spatial pulse design. First, the excitation k-space trajectory is restricted by the length of the RF pulse and gradient amplitude and slew rate limits. This often means that the excitation trajectories do not extend very far into k_{xy}, resulting in low excitation resolution. In many cases, the off-resonance in the human brain varies slowly enough that with even low resolution the spectral-spatial pulse can encode the spatially varying off-resonance. However, in regions where the field map contains a steep off-resonance gradient, the spectral-spatial pulse will not fully capture this transition and may perform no better than a purely spectral pulse. Furthermore, when moving to 3D spectral-spatial designs, there will be further limitations in resolution, though this limitation can be eased by using parallel excitation.

Although this Chapter explored spiral trajectories to understand how the trajectory affects spectral-spatial pulse performance, by no means was this search exhaustive. There is still a need to better understand the trade-off between k-space extent in k_{xy} and other pulse design parameters such as target bandwidth L. One possible way of addressing this problem is the joint design of optimal k-space trajectories and RF pulses. In recent work by Sun et al. [8] and Davids et al. [41] the joint design problem is considered for the application of inner-volume excitation. Joint optimization of the k-space trajectory/gradient waveform is a natural extension of our RF pulse design problem.

Another important factor for spectral-spatial pulse design is that it must occur online. For the results shown, the pulse design routine increased scan session duration minimally. Nevertheless it is still possible that patients will move between field map scan and acquisition with the designed pulse, compromising the spatially varying pulse design. Therefore reducing motion and time in the scanner is critical. For purely spectral pulses, motion is less problematic because the pulses are not spatially resolved.

The work presented here is a feasibility study that uses 3D readout for a pulse designed to a particular 2D slice. For this concept to become practically useful, we will need to expand our design to three spatial dimensions. One benefit of 3D spectral and spectral-spatial pulse designs is that they can help account for field map variation in the slice dimension, but the higher dimensionality could increase the online pulse design time significantly. An alternative experiment could be constructed for a slice-selective spectral-spatial prewinding pulse. This is challenging because a third gradient dimension, the slice-select gradient, is introduced. We imagine that "fast k-z" [64] or spokes [65] trajectories could be used. Here, we would have to face the competing needs of high k_z extent for selecting relatively thin

slices yet also producing enough spokes for moderate sampling in the k_{xy} plane.

We designed the spectral-spatial pulses using the small-tip angle approximation. Even though the RF pulses may be designed for a certain low flip angle such as $\alpha = 15.8°$ as used in our human experiments, the instantaneous flip during the RF pulse may be higher. In [55], Sun et al. demonstrated that spectral pulses can exceed 90° when the integrated power is relatively high (or Tikhonov regularization term is low). For spectral-spatial pulses, the presence of magnetic field gradients makes the constraining of instantaneous flip angles more difficult; the flip angle is no longer simply proportional to the integral of the RF pulse with time. However, the agreement we observe between the STA model and Bloch simulation suggests that the STA approximation was adequate for these designs, perhaps due in part to our integrated power constrained design. The need for the current RF pulse design approach to satisfy the STA approximation means that spectral and spectral-spatial pulse designs should be monitored for flip angle violations, especially when the target flip angle is high.

Here we designed spectral and spectral-spatial prewinding pulses with fixed constraints on integrated power and found that spectral-spatial pulses performed with lower error for all quantitative metrics. Conversely, we would expect that designing spectral and spectral-spatial pulses for the same error values would result in the spectral-spatial pulses having lower integrated power. This formulation might have useful applications when SAR deposition is the primary concern. Furthermore, we have only reported the equivalent SAR constraints from our RF pulse optimization as reported on the scanner during imaging. In the future, we would like to have an efficient method for estimating SAR deposition during the design of RF pulses so that the constraints are applied directly in terms of W/kg.

Tailored RF pulses such as the spectral-spatial pulses explored in this Chapter depend on the accuracy of the magnetic field gradients. Distortion and timing errors between gradients and RF pulse is a common problem that can degrade excitation accuracy [66]. In our experiments, we pre-measured gradients using the method in [67] and did not notice significant deviation between prescribed and measured excitation trajectories. However, as we design further spectral-spatial pulses with other excitation trajectories it may become necessary to evaluate gradient errors and perhaps adopt novel correction schemes such as that described in Harkins et al. [66].

In the future, we plan to extend our spectral-spatial pulse design to three spatial dimensions. Another plan is to tailor the pulse design to the STFR sequence by adjusting the design for its performance in the steady-state (whereas tip-down/tip-up pairs are currently designed for one cycle of STFR). Finally, we will examine a number of clinical imaging applications such as optic nerve, lung, or bowel imaging where these prewinding pulses

might be particularly useful.

4.7 Conclusion

This chapter introcues a spectral-spatial phase prewinding RF pulse that extends the spectral pulses introduced by Assländer et al. [15]. These pulses can compensate for field inhomogeneity induced phase by prewinding the phase such that, after excitation, spins refocus at the echo time. While purely spectral pulses are limited to a modest off-resonance bandwidth, introducing excitation k-space provides spatially varying off-resonance coverage. This approach can create a wider effective recovery bandwidth that reduces signal loss. We demonstrated this concept by designing spectral-spatial pulses with variable density spiral k-space trajectories. We compared spectral-spatial pulses to their purely spectral counterparts with simulation, phantom studies, and in vivo human brain studies using the STFR steady-state sequence. The results confirm that spectral-spatial pulses do in fact improve recovery of signal loss due to off-resonance when compared to purely spectral prewinding pulses.

CHAPTER 5

Slab-selective Spectral Prewinding Pulses

5.1 Introduction

Spectral prewinding RF pulses provide spin-echo like re-phasing of spins in gradient echo sequences [15]. A small-tip angle purely spectral prewinding pulse recovered a limited bandwidth of off-resonance for imaging in the STFR sequence, a steady state sequence with similar contrast to balanced-SSFP [55]. A spectral-spatial pulse increased the effective prewinding bandwidth by varying the bandwidth spatially using a 2D field map [9]. This Chapter[1] demonstrates for the first time the incorporation of spectral prewinding into slab-selective pulses.

Slab-selective pulses are useful for 3D imaging applications because they can reduce scan time by limiting the FOV in the slab dimension [68]. This allows imaging with various receive coil configurations, as the coil sensitivity in the slab dimension no longer is used to determine FOV. Furthermore, tailored slab-selective pulses can mitigate $B1^+$ inhomogeneity [69], especially in the case of Parallel Transmit (pTx) systems [70]. Slab-selective pulses are a staple of standard protocols, from fMRI to cardiac imaging.

The STFR sequence is an alternative to bSSFP that has similar SNR and contrast with less sensitivity to off-resonance offsets [6]. In STFR, first a tip-down RF pulse is applied, then free precession occurs, then a tip-up RF pulse recovers transverse magnetization to the longitudinal axis and a gradient crusher is applied. STFR is also more amenable than bSSFP to magnetization preparation or fat saturation pulses [71]. Two variants of STFR have been described, unspoiled and spoiled, where spoiled refers to adding RF phase cycling. In practice, unspoiled STFR is less sensitive to RF phase error or phase mismatch between tip-down and tip-up pulses compared to the spoiled counterparts [38]. Without RF spoiling, the tip-up pulse design must "match" the tip-down target pattern to recover

[1]This Chapter is in preparation for the journal *Magnetic Resonance in Medicine* and was presented at ISMRM 2018 [17].

transverse magnetization. STFR has been used in the context of inner volume imaging [8], fMRI [39], and recently, prewinding pulses [55],[9]. This Chapter explores STFR with slab-selective tip-down and tip-up pulses that also incorporate spectral prewinding [15].

5.2 Theory

Prewinding pulses aim to compensate for the phase accumulation of spin isochromats occurring during free precession after an RF pulse is applied, leading to contrast that is more determined by T2 than T2* [15]. The recovery bandwidth of purely spectral prewinding is limited, but can be effectively increased with spatially varying prewinding bands [9]. (See also Chapter 4). That work set the spectral and spectral-spatial target magnetization patterns for RF pulse design with a target magnitude and phase pattern spanning a range of off-resonance frequencies that rephased at echo time TE [15]. In this chapter, we vary the target magnitude along the slab dimension z and the target pattern is written as

$$d(z, f) = p(z)\mathrm{e}^{2\pi i \mathrm{TE} f} \tag{5.1}$$

In this equation, $p(z)$ denotes the slab-select envelope equal to target flip angle $\sin(\theta)$ within the slab, and zero outside of the slab along the z dimension. The target echo time TE is defined as half the free precession interval within the STFR sequence [6] and f is an off-resonance frequency. This version of $d(z, f)$ represents the 2D slab-select spectral case, and Figure 5.1 shows an example 2D target pattern (magnitude and phase).

Reducing the space over which the design is specified (e.g., within **d**) enables more freedom in iterative RF pulse design and can result in more accurate excitation accuracy. We exclude some samples of **d** with a weighting matrix that defines "care" and "don't-care" regions of the design space. For the slab-select spectral pulse design, we define a diagonal weighting matrix **W** along the slab z and frequency f dimensions as samples of the following weighting function:

$$w(z, f) = \begin{cases} 1, & [(\min_{x,y} \Delta f(x, y, z) - \frac{L}{2}) \ \leq \ f \ \leq (\max_{x,y} \Delta f(x, y, z) + \frac{L}{2})] \ \text{ and } \ z \in z_{\text{in}} \bigcup z_{\text{out}} \\ 0, & \text{otherwise} \end{cases} \tag{5.2}$$

where z_{in} is the in-slice region, z_{out} is the out-of-slab region, and $\Delta f(x, y, z)$ denotes the field map. L is an additional bandwidth that accounts for the spread of intravoxel spins centered at the field map frequency for each voxel [9]. Along z, nearly all locations are of interest in the target pattern —we want no excitation outside the slab and uniform excitation within the slab. However, a perfect rectangular slice profile is unattainable (as the Fourier transform is a sinc function with infinite extent). Therefore, the weights include a don't care region along the z dimension as a transition region between in-slab and out-of-slab

regions. Additionally, we vary the weights along the f dimension for each slice location of the in-slab and out-of-slab regions. At every slice z, only frequency locations included over the interval shown in Eq. (5.2) are defined as "care" regions in $w(z, f)$. Figure 5.1b-d illustrates a 2D target pattern **d** and associated weights $w(z, f)$.

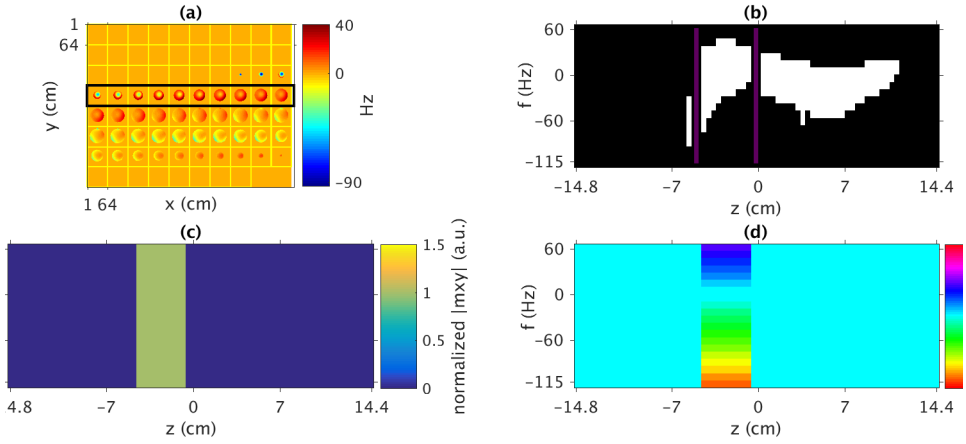

Figure 5.1: 3D field map and associated spectral slab-selective target design and weights.(a) Field map $\Delta f(x, y, z)$ for phantom with susceptibility artifact where the design slab is selected as the region captured by the black rectangle.(b) Weighting function $w(z, f)$ associated with variation in the field map along the slab dimension: for each slice location along the horizontal axis z, the range of frequencies is included in the white "care" region along the vertical axis f. The purple bars indicate the "don't care" transition zones between in-slab and out-of-slab regions. (c) Spectral slab-selective tip-down magnitude target pattern $|d(z, f)|$. (d) Spectral slab-selective tip-down phase pattern $\angle d(z, f)$

5.3 Methods

5.3.1 Excitation K-Space

For slab-selective prewinding, the G_z gradient provides slab-selection, and the extent of k_z is directly related to the sharpness of the slab profile. Ref. [9] (Chap.4) showed empirically that repeating the k-space trajectory pattern a few times during the excitation pulse was beneficial to prewinding performance. This creates competing interests between spectral prewinding (time at k-space center) and time to transverse k_z ($-k_{z,\max}$ to $+k_{z,\max}$). We chose to use repeated, sinusoidal-like sweeps through k_z as a means of meeting the spectral slab-selective needs. Number of sweeps, time spent crossing through k-space center, and overall trajectory design remains an open and challenging problem, especially when

optimized jointly with RF pulse design [8], [41]. This Chapter considers sinusoidal trajectories with additional time spent approaching k-space center. For a 3.576 ms pulse length, we tried trajectory variants with 4, 6, 8, and 10 sweeps with additional samples around each zero-crossing that varied based on the total number of sweeps. Figure 5.2 plots these sweeping excitation trajectories along with their gradient waveforms and an example spectral slab-selective RF pulse waveform.

We designed these trajectories to meet gradient amplitude and slew rate constraints by solving a 2nd-order B-splines basis function parameterization described in [7] with an efficient constrained optimization problem in CVX software [35]. Here, we defined the k-space trajectory as $\mathbf{Hc}$ where $\mathbf{H} \in \mathbb{R}^{N_t \times V}$ contained V basis vector columns with associated $\mathbf{c}$ basis coefficients. We minimized the difference between the desired trajectory $\mathbf{k}_{\text{target}}$ and $\mathbf{Hc}$ using V=50 spline coefficients, yielding our parameterized k-space trajectories. Mathematically, this process is written as

$$\begin{aligned} \hat{\mathbf{c}} = \underset{\mathbf{c}}{\text{argmin}} \ & ||\mathbf{k}_{\text{target}} - \mathbf{Hc}||_2^2 \\ \text{s.t.} \ & ||\mathbf{D}_1\mathbf{Hc}||_\infty \leq \gamma \Delta t g_{\max} \\ & ||\mathbf{D}_2\mathbf{Hc}||_\infty \leq \gamma \Delta t^2 s_{\max} \\ & [\mathbf{Hc}]_{N_t} = 0 \end{aligned} \tag{5.3}$$

where $\mathbf{D}_1$ and $\mathbf{D}_2$ are the first- and second-order finite difference matrices approximating the first and second derivatives defining the maximum gradient amplitude and slew rate constraints, respectively. The last constraint ensures that the final point in the excitation k-space trajectory ends in zero. This optimization step produced a smoothed k-space waveform $\mathbf{k} = \mathbf{H}\hat{\mathbf{c}}$ with additional zero crossing samples, effectively causing a VERSE-like [72] effect of slowing down the trajectory around k-space center.

5.3.2 RF Pulse Design

For spectral slab-selective pulses, we set the RF pulse design target patterns ($\mathbf{d}$) and weight matrix ($\mathbf{W}$) by sampling Eqs. 5.1-5.2. We then designed the RF pulse in the spinor domain [24], using the small-perturbation optimal control method described in Ref. [28]. This approach helped address violations of STA approximation pulse design that we empirically found occurred for this unique type of prewinding pulse. The small-perturbation approximation works by updating an initial baseline RF pulse $\mathbf{b}_{\text{init}}$ that we design first under the STA approximation [22] by solving

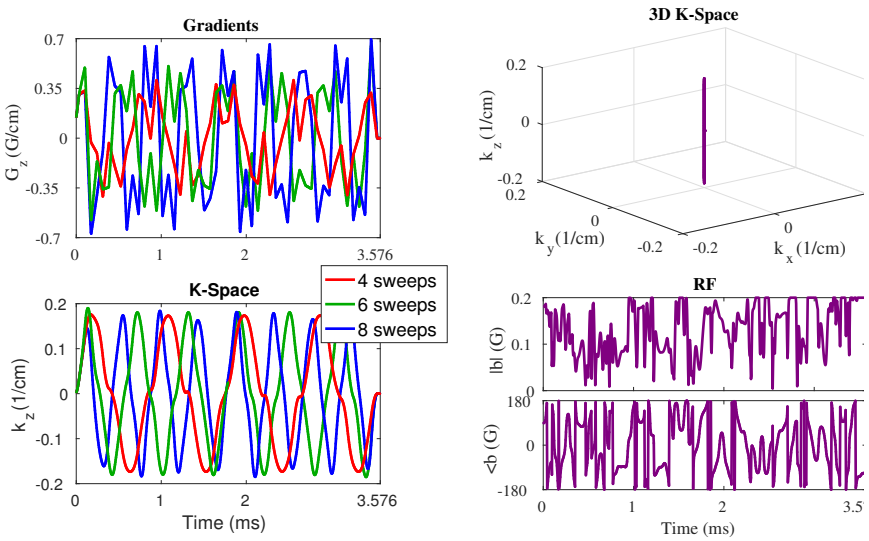

Figure 5.2: Sweeping k_z trajectory variations used during excitation for the spectral slab-selective pulse. The left-hand plots show the gradient (top) and k-space (bottom) waveforms vs time, and the right-hand plots show the 3D k-space trajectory (top) and an example spectral slab-selective pulse (bottom).

$$\begin{aligned} \hat{\mathbf{b}}_{\text{init}} &= \underset{\mathbf{b}}{\text{argmin}} \ ||\mathbf{Ab} - \mathbf{d}||_{\mathbf{W}}^2 \\ &\text{s.t.} \ \ ||\mathbf{b}||_2^2 \Delta t \leq p_{\max} \end{aligned} \tag{5.4}$$

where $\mathbf{A}$ is the STA approximation system matrix [1] and $p_{\max}$ is a conservative, empirical power constraint in Gauss^2·ms. For this RF pulse application in the STFR sequence, we set the power constraint so it approaches roughly half the 6 minute SAR limits for head imaging, or 2.0 W/kg. This ensures our ability to repeat scans without waiting for the 6 minute power monitoring to decrease and also empirically meets peak RF amplitude limits. Setting the power constraint for the RF pulse design in the full context of STFR (i.e., the duty cycle) remains an open challenge. If the flip angle is reduced to smaller values ($\leq 5°$), the problem changes to a peak-constrained pulse design where the RF amplitude is directly controlled and power limitations for scanning are met (See Appendix B Figures B.8-B.9, Table B.1). We solve these convex, constrained cost functions using FISTA [32].

We design these slab-selective prewinding pulses for the small-tip fast recovery steady-state sequence without RF spoiling. For this sequence the target *final* tip-down flip angle is on the order of θ=15-30°. However, these pulses can still exceed the STA approximation (θ $\leq$90°) at intermediate time points during the RF pulse, as shown in Figures B.1 and

B.2. When the linear STA method is violated, we ideally would like to design the RF pulse directly with the non-linear Bloch equation evaluation $\mathrm{Bloch}(\mathbf{b})$,

$$\begin{aligned} \hat{\mathbf{b}} = \underset{\mathbf{b}}{\operatorname{argmin}} \ \ & ||\mathrm{Bloch}(\mathbf{b}) - \mathbf{d}||_{\mathbf{W}}^2 \\ \text{s.t.} \ \ & ||\mathbf{b}||_2^2 \Delta t \leq \ \ p_{\max} \ \ . \end{aligned} \tag{5.5}$$

Following [28] we solve Eq. 5.5 using the spinor domain OC approach. After designing the initial RF pulse, we simulate the RF pulse in the Bloch spinor domain (repeated from Eq. (2.8))

$$\frac{d}{dt}\begin{pmatrix} \beta \\ \alpha^* \end{pmatrix} = \frac{i\gamma}{2}\begin{pmatrix} \mathbf{G}(t)\cdot\mathbf{r} & b(t)^* \\ b(t) & -\mathbf{G}(t)\cdot\mathbf{r} \end{pmatrix}\begin{pmatrix} \beta \\ \alpha^* \end{pmatrix} \tag{5.6}$$

where α and β are the Cayley-Klein parameters [24] (Eq.2.10-2.11), γ is the gyromagnetic ratio, and $\mathbf{G}(t)$ denotes the time-varying excitation gradients in 3D spatial locations $\mathbf{r}$. We then compare the Bloch spinor calculation of magnetization from $\mathbf{b}_{\text{init}}$ to the target pattern $\mathbf{d}$ in terms of transverse and longitudinal components,

$$m_{xy}^d = \sin\left(|\mathbf{d}|\right)\mathrm{e}^{i\angle\mathbf{d}} \tag{5.7}$$

and

$$m_z^d = \cos\left(|\mathbf{d}|\right) \ \ . \tag{5.8}$$

The difference in magnetization performance of $\mathbf{b}_{\text{init}}$ and $\mathbf{d}$ in the magnetization domain, $m_{xy}^i = m_{xy}^d - m_{xy}^{\mathbf{b}_{\text{init}}}$ and $m_z^i = m_z^d - m_z^{\mathbf{b}_{\text{init}}}$, is used to form the optimal control matrix update [28] that improves the RF pulse design by designing a perturbation pulse $\widetilde{\mathbf{b}}$ that we add to the current RF pulse. We repeat these updates iteratively, with each time the RF pulse and target pattern re-simulated and corrected by the spinor domain simulation. For each update, the RF pulse is integrated power constrained as in $Eq.$ (5.4). We stop the small-perturbation updates as soon as the stopping criterion is met, which is based on the RF pulse simulated NRMSE:

$$\mathrm{NRMSE}^i = \sqrt{\frac{\frac{1}{N}\sum_{n=1}^{N}|\mathbf{M}^d - \mathbf{M}^i|^2}{\frac{1}{N}\sum_{n=1}^{N}|\mathbf{M}^d|.^2}} \tag{5.9}$$

where $\mathbf{M} = [m_{xy} \ m_z]^T]$ for either the target pattern (d) or current iterate (i) simulated over N sample locations contained within weighting matrix $\mathbf{W}$. The updates are complete when

the NRMSE stops improving or a max number of iterations is met. Algorithm 2 shows the pseudocode of this process.

For the tip-up pulse of the STFR sequence, we perform the same constrained optimal control design method, but with a different target pattern. In this case, we define $\mathbf{d}^{\mathrm{tip-up}}$ as the Bloch-simulated magnetization after tip-down and free precession within the STFR sequence. This approach allows the tip-up pulse to correct for imperfections in the tip-down pulse [6]. For the slab-selective spectral case this Bloch simulation is conducted along z, f dimensions where $\mathbf{f}$ is the vector of frequencies used in the target tip-down pattern. We then design $\mathbf{b}^{\mathrm{tip-up}}$ per Algorithm 2 over the negative spread of frequencies $\mathbf{f}$, and then negate and reverse the RF pulse for "tipping-up" magnetization [55].

After designing an RF pulse, we evaluate the pulse by 4D Bloch simulation conducted in x, y, z, f space with an intravoxel spread of frequencies assumed to have a Gaussian distribution with σ=25 Hz [61]. We compute these simulations at two critical time points within STFR: after tip-down at the echo time (where magnetization magnitude should be uniform and at the target flip angle θ, and phase should be zero), and after tip-up (where transverse magnetization magnitude should be zero within the slab, and phase is irrelevant).

5.3.3 Imaging Protocol

We conducted all scanning with a 3T GE MR750 scanner using an 8-channel Receive GE MRI Brain Array Coil (GE Healthcare, Waukesha, WI). For both phantom and human volunteer experiments, we used three types of sequences. First, we collected a lower resolution dual-echo SPGR acquisition for field map estimation, with imaging parameters FA/TE1/TE2/TR=10°/1.7 ms/4 ms/6.892 ms, FOV=240×240×336 mm^3, matrix size 64×64×84. We chose the larger FOV in the z dimension to eliminate wrap-around aliasing from the volunteer's shoulders into the top of the head. After a roughly 1.5 min acquisition, we estimated the full 3D field map using the method in Ref. [73] in about 1 additional minute on an eight-core 64 bit processor with 3.60 GHz (Intel(R) Xeon(R) CPU E5-1620) and 7.6 GiB RAM desktop computer. Note, the NUFFT [59] operation used involved in creating the STA approximation and OC perturbation update matrices only operate on a single core.

Next, we acquired two higher resolution single echo SPGR acquisitions with FA/TE/TR =10°/1.7 ms/8.844 ms, FOV=240×240×336 mm^3, matrix size 256×256×84. One of these acquisitions was instead collected with the body coil, while the second one was again acquired using the 8-channel coil for receive. Each SPGR scan was about 6 min. This double acquisition served two purposes: 1) we estimated the 8-channel sensitivity map with a body

Algorithm 2 Pseudocode for designing slab-selective prewinding pulse with optimal control

Input: Target pattern $\mathbf{d}$, weighting matrix $\mathbf{W}$, excitation trajectory $\mathbf{k}$, and RF hardware constraint (in this case, integrated power constraint)

Output: RF pulse $\mathbf{b}$

Initialization :

Using $\mathbf{k}$, construct STA approximation matrix $\mathbf{A}$

Design $\mathbf{b}^1$ by solving STA problem with RF power constraint (Eq. [5.4]) via FISTA

Use $\mathbf{b}^1$ with Bloch simulator to compute $\mathbf{M}^1$ and construct optimal control perturbation matrix $\widetilde{\mathbf{A}}_{OC}^1$ from $\mathbf{b}^1$ and $\mathbf{M}^1$

NRMSE^0=1, NRMSE^1=NRMSE($\mathbf{b}^1$), p=1

Optimal Control Perturbation Updates[28] :

while ($p <$ max no. iter and $\mathrm{NRMSE}^p <= 0.9999 * \mathrm{NRMSE}^{p-1}$) **do**

  Update target perturbation $\widetilde{\mathbf{M}}^{p+1} = \mathbf{M}^d - \mathbf{M}^p$

  Design constrained perturbation RF pulse to match target perturbation (adapting STA problem)

$$\widetilde{\mathbf{b}}^p = \underset{\widetilde{\mathbf{b}}}{\operatorname{argmin}} \; ||\widetilde{\mathbf{A}}_{OC}^p \widetilde{\mathbf{b}} - \widetilde{\mathbf{M}}^{p+1}||_{\mathbf{W}}^2$$
$$\text{s.t.} \;\; ||\widetilde{\mathbf{b}} + \mathbf{b}^p||_2^2 \Delta t \leq p_{\max}$$

  while ($j <$max no. iter.) **do**

    Add perturbation RF pulse to previous designs, $\mathbf{b}^{p+1} = \widetilde{\mathbf{b}}^p + \mathbf{b}^p$

    Simulate $\mathbf{M}^{p+1}$, compute NRMSE^{p+1}, construct OC matrix $\widetilde{\mathbf{A}}_{OC}^{p+1}$

    if ($\mathrm{NRMSE}^{p+1} > 0.9999 * \mathrm{NRMSE}^p$) **then**

      $\widetilde{\mathbf{b}}^p = \frac{1}{2}\widetilde{\mathbf{b}}^p$

      j=j+1

    else

      j=max no. iter.

    end if

  end while

  p=p+1

end while

return $\mathbf{b}^p \in \mathbb{C}^{N_t}$

coil reference using the method in Ref. [74] for complex coil combination, and 2) we used it as a reference scan with known echo time for estimating the inherent object phase without off-resonance effects. The inherent object phase is crucial for recovering the "true" phase image for the spectral slab-selective pulse acquisitions and will be discussed in further detail below.

During the set of two SPGR acquisitions, we performed slab-selective prewinding pulse design using the estimated field map from the first dual echo acquisition. We picked a 4.4 cm slab consisting of eleven 0.4 cm slices from the full 3D field map for slab-selective design. We then designed these pulses on the same eight-core 64 bit processor desktop computer described above with MATLAB R2016a (The MathWorks, Natick, MA) and imported them back to the MRI scanner. We recorded the time to design each pulse (tip-down design, free precession Bloch simulation, tip-up design, and Bloch simulation after tip-up) to compare the conventional STA and OC-based methods. Finally, we used these pulses within the STFR sequence with FA/TE/TR=16°/3.648 ms/16.188 ms, same FOV and matrix size as in the second set of SPGR scans. Each STFR acquisition was also roughly 6 min.

5.3.4 Phantom Experiments

We initially tested our slab-selective pulse design experimentally in an FBIRN gel phantom [50] with an induced susceptibility artifact created by taping a small piece of metal to a pad placed on the phantom. Following the imaging protocol in Section 5.3.3, we designed four spectral slab-selective pulses using the 3.576 ms k_z excitation trajectories (4, 6, 8, or 10 sweeps) described in Section 5.3.1. We used MR parameters T1/T2=510 ms/50 ms, based on previous phantom measurements, for Bloch simulation in pulse design. For each of the four pulses, we designed a tip-down/tip-up STFR pulse pair using the STA approximation and the OC approach (Algorithm 2), making a total of 8 spectral slab-selective pairs. Each set of pulses was used in an STFR acquisition. The total imaging protocol (field map, SPGR, pulse design, and STFR) took about one hour.

5.3.5 In Vivo Experiments

Based on the FBIRN susceptibility artifact phantom experiment, we selected the"best" performing k_z trajectory (in the simulated excitation NRMSE sense) for in vivo brain experiments. We recruited a healthy human volunteer for scanning following the same imaging protocol used with the phantom. This single k_z trajectory was used for slab-selective prewinding pulse design, again with STA (i.e., no OC) and OC-based methods for a total

of 2 STFR acquisitions. In this case, we used literature grey matter values of T1/T2=1300 ms/800 ms [75] during the Bloch simulation component of pulse design. For the human experiments, the total imaging time was roughly 40 min.

5.3.6 Analysis

Using the 4D x, y, z, f Bloch simulations, we evaluate our pulse design with four, scalar performance metrics: excitation NRMSE at TE along the full z-dimension, magnitude NRMSE at TE along the full z-dimension, phase RMSE at TE within the slab, and mean residual transverse magnetization magnitude within the slab after tip-up. Excitation NRMSE describes the complex error of the excitation at TE and is a good summary metric for both slab-selectivity and prewinding. Meanwhile magnitude NRMSE is a better metric to assess just slab-selection and phase RMSE, just phase prewinding. These metrics are described in detail in Ref. [9] (Eq. (4.13)-Eq. (4.17)). In addition to pulse design time, these metrics served as a way to quantitatively compare the spectral slab-selective pulse design variants (e.g., k_z trajectory, STA vs. OC methods).

We compared experimental images in a more qualitative manner. After sensitivity map estimation from the two higher resolution SPGR reference scans, we combined the complex 8-channel STFR data across coils using Roemer's optimal coil combination [76] which is analogous to fully-sampled SENSE reconstruction [77]. This allowed us to create coil-combined phase images, in addition to the conventional sum-of-squares magnitude images. In a successfully designed prewinding pulse, the phase image acquired at TE should be close to the phase of a spin echo image.

We reconstructed magnitude sum-of-squares images to evaluate the slab excitation profile and uniformity for the spectral slab-selective designs in the STFR acquisitions. For both simulated magnetization and experimental images, we also measured the magnitude slab profile within the slab from the center y location (the "X-Profile") and the center x location (the "Y-Profile").

Analyzing STFR phase images required a few additional processing steps. After coil combination of the 8-channel images from the sensitivity map, we estimated the inherent object phase from the coil-combined 8-channel SPGR image. This is computed by removing the image phase accumulation attributed to off-resonance at the known 1.7 ms echo time, effectively creating a TE=0 ms image, where the remaining phase is the inherent phase of the object, including phase from the receive coil, incident phase from excitation, and other sources.

We performed an additional, separate experiment without slab-selective prewinding

pulse design to provide a reference of the residual linear phase and constant offset observed in the phase image with inherent object phase removed. Here, we imaged a dimethyl silicone-gadolinium phantom (3T Head TLT Sphere Phantom Model:2359877 GE Healthcare, Waukesha, WI) with homogeneous field (no susceptibility artifact). This phantom was used to limit the effects of conductivity in the object for linear phase estimation. We began by collecting the first field map and pair of two higher resolution SPGR scans from the imaging protocol. Then we acquired a standard spin echo image with TE/TR=9 ms/250 ms, FOV=240×240×336 mm^3, and matrix size 256×256×11. Appendix B Figure B.3 shows the data from this reference experiment.

Using the silicone phantom reference data set, we fit a weighted least squares line to the residual phase image after complex coil combination and TE=0 ms phase removal. This linear phase slope and constant offset were established as the standard correction terms for all experimental slab-selective prewinding phase images for this particular imaging protocol. Furthermore, we compared this correction to the phase image from the spin echo acquisition, where we know that the phase image should be near zero. Appendix B Figure B.3 shows the TE=0ms phase image from SPGR, the estimated linear phase term, and the spin echo phase image from the silicone phantom reference scan.

5.4 Results

5.4.1 Phantom Experiments

Table 5.1 reports the total design time (tip-down pulse design, Bloch simulation at TE, tip-up pulse design, and Bloch simulation after tip-up) and performance metrics computed from 4D Bloch simulation for the six spectral slab-selective pulse variants in the phantom study. The total design time was less for the designs with just STA method, but the OC-based method still provided designs in less than one minute. Both approaches provided similar magnitude NRMSE (the STA design without OC, slightly better), but the OC method improved the excitation NRMSE, phase RMSE, and especially the mean residual magnetization after tip-up. The designs using the 10 k_z sweeps k-space trajectory produced the best simulation performance metrics.

Table 5.1: Design comparison for slab-selective prewinding pulses designed with and without (just STA) the additional optimal control perturbation updates for the phantom experiment. Metrics shown include: total design time, magnitude NRMSE at TE, phase RMSE

at TE, excitation NRMSE at TE, and mean residual transverse magnetization magnitude after tip-up. The best performance for each measure is in **bold** font.

RF Pulse Design	Design Time (min:sec)	Mag. NRMSE	Phase RMSE (°)	Excitation NRMSE	Residual $\lvert M_{xy,\text{tip-up}}\rvert$
4 k_z sweeps, just STA	0:35	**0.26**	18.4	0.39	0.36
6 k_z sweeps, just STA	**0:34**	**0.26**	13.6	0.34	0.33
8 k_z sweeps, just STA	0:35	**0.26**	12.9	0.33	0.31
10 k_z sweeps, just STA	0:35	**0.26**	12.4	0.32	0.30
4 k_z sweeps, with OC	0:59	0.27	11.3	0.32	**0.02**
6 k_z sweeps, with OC	0:57	0.27	10.2	**0.31**	**0.02**
8 k_z sweeps, with OC	0:57	0.27	9.9	**0.31**	**0.02**
10 k_z sweeps, with OC	0:57	0.27	**9.7**	**0.31**	**0.02**

Figure 5.3 shows the echo time simulated magnetization magnitude, phase, and slab profiles for the best performing 10 k_z sweeps k-space trajectory pulses, both without and with optimal control. There are little noticeable differences between the two approaches in the simulation images and slab profiles, yet these plots only reflect the behavior of the tip-down pulse for a single RF excitation. They are not in the context of the full STFR sequence at steady-state and do not consider the improved tip-up behavior when using optimal control.

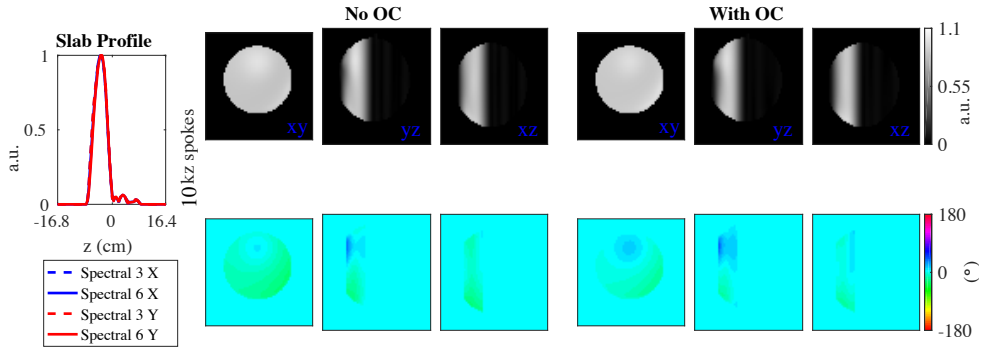

Figure 5.3: Bloch simulation echo time magnetization magnitude (top row), phase (bottom row), and mean slab profile in the x and y dimensions (left plot) for 2 of the 8 spectral slab-selective pulse designs in the phantom, those using a 10 k_z sweep trajectory. For the slab profile plot, the dotted lines indicate pulses designed without OC (just STA approximation), and solid lines indicate with OC. Simulated magnetization is shown for all three imaging planes xy, yz, and xz. The magnetization magnitude images are normalized to the target flip angle, meaning that the target magnitude is uniform and equal to 1. The target phase is zero at TE. The STA-based (left-most columns) and OC-based (right-most columns) perform similarly after just one RF excitation.

Figures 5.4 and 5.5 show the experimental STFR magnitude images and phase phantom images, respectively, for the various spectral slab-selective pulse design variants. The steady-state behavior differs from the single tip-down simulation, where here imperfect excitation accumulates in the out-of-slab region. These figures can be compared and contrasted to their simulated magnetization images and slab profiles, shown in Appendix B Figures B.4-B.6.

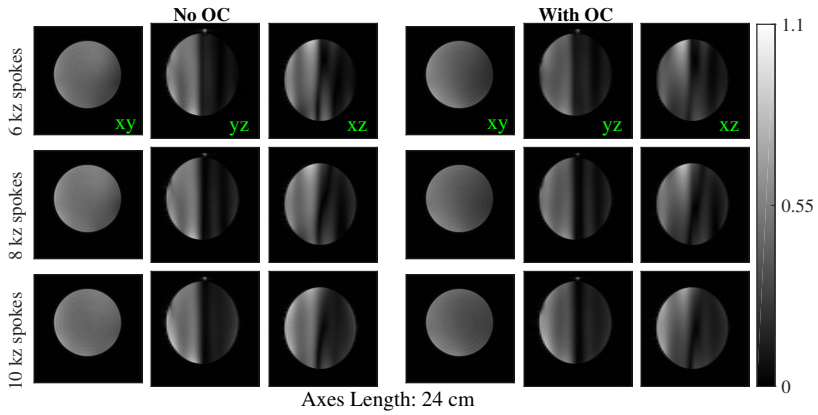

Figure 5.4: Experimental STFR magnitude images of phantom with susceptibility artifact for the spectral slab-selective pulse designs using 6 (top row), 8 (middle row), and 10-sweep (bottom row) k_z trajectories, each with (right-most columns) and without (left-most columns) OC. The STFR images are shown for all three imaging planes xy, yz, and xz.

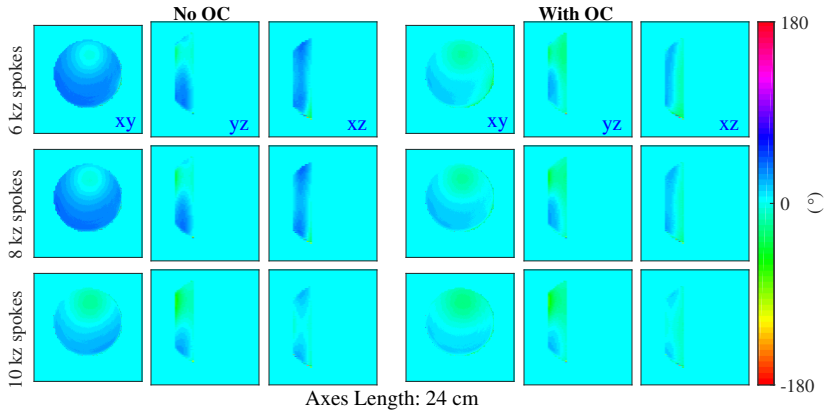

Figure 5.5: Experimental STFR phase images of phantom with susceptibility artifact for the spectral slab-selective pulse designs using 6 (top row), 8 (middle row), and 10-sweep (bottom row) k_z trajectories, each with (right-most columns) and without (left-most columns) OC. The STFR images are shown for all three imaging planes xy, yz, and xz. The phase images are closer to zero for the spectral design with OC.

5.4.2 In Vivo Experiments

Table 5.2 reports the total design time and performance metrics computed from 4D Bloch simulation for the two spectral slab-selective pulse variants in the in vivo study, i.e., the 10 k_z sweeps trajectory with STA and OC methods. As seen in simulation, the non-OC pulse takes less time to design but results in worse performance metrics compared to the

pulse designed with optimal control for all metrics except for magnitude NRMSE, where performance is about the same.

Table 5.2: Design comparison for slab-selective prewinding pulses designed with and without (just STA) the additional optimal control perturbation updates for the human in vivo experiment. Metrics shown include: total design time, magnitude NRMSE at TE, phase RMSE at TE, excitation NRMSE at TE, and mean residual transverse magnetization magnitude after tip-up. The best performance for each measure is in **bold** font.

RF Pulse Design	Design Time (sec)	Mag. NRMSE	Phase RMSE (°)	Excitation NRMSE	Residual $\lvert M_{xy,\text{tip-up}}\rvert$
10 k_z sweeps, just STA	**0:28**	**0.30**	18.2	0.40	0.18
10 k_z sweeps, with OC	0:45	0.31	**13.3**	**0.37**	**0.02**

Figure 5.6 shows the simulated magnetization at TE and after the tip-up pulse for one TR of the STFR sequence (not-steady state). This figure can be used to compare the designs to a successful tip-down and tip-up pulse pair which creates uniform, zero-phase slab excitation at TE and leaves little residual magnetization magnitude after tip-up. Here, the OC-based method comes closer to that goal.

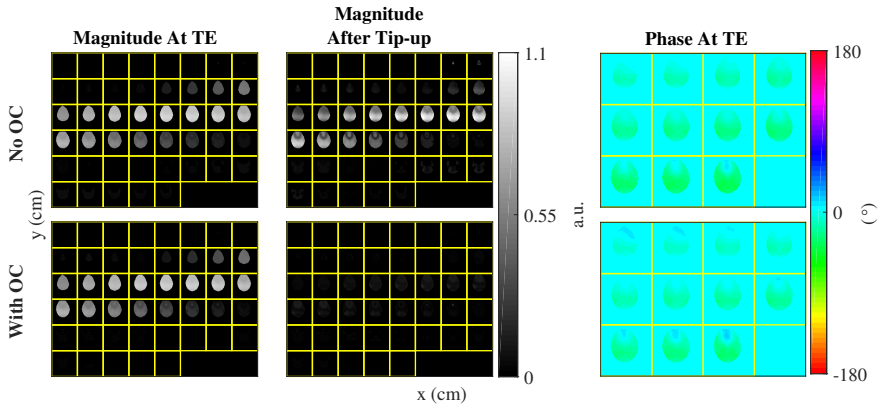

Figure 5.6: Bloch simulation for single TR of the STFR pulse sequence for the two spectral slab-selective pulses for the in vivo experiment. Top row: spectral slab-selective pulses with 10 k_z sweep trajectory using STA without OC. Bottom row: spectral slab-selective pulses with 10 k_z sweep trajectory with OC. Magnetization magnitude at TE (left column), magnetization magnitude after the tip-up pulse (middle column), and magnetization phase at TE (right column). Magnetization magnitude should be uniform within the slab at TE and nearly zero after tip-up. Magnetization phase should be nearly zero at TE and is irrelevant after tip-up.

Figure 5.7 shows the simulated magnitude compared to the target pattern, the simulated phase for the in vivo experiment, and the slab profiles from these simulations. These simulations are in agreement with the performance metrics in Table 5.2 for evaluating a single RF excitation.

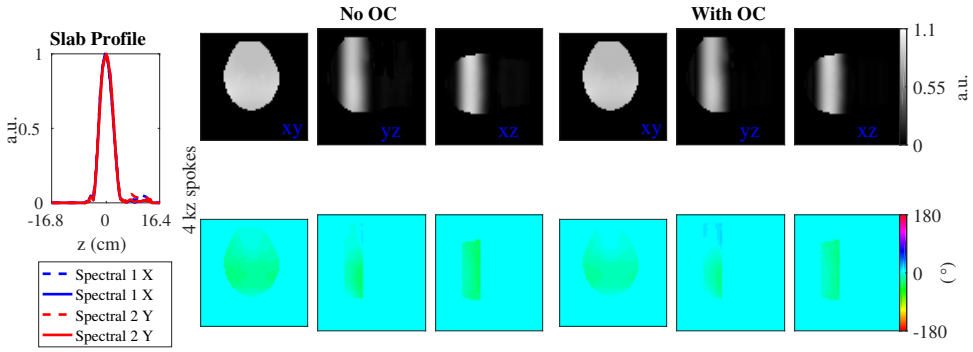

Figure 5.7: In vivo Bloch simulation echo time magnetization magnitude (top row), phase (bottom row), and mean slab profile in the x and y dimensions (left plot) for the two spectral slab-selective pulse designs using an 10 k_z sweep trajectory. For the slab profile plot, the dotted lines indicate pulses designed without OC (just STA approximation), and solid lines indicate with OC. Simulated magnetization is shown for all three imaging planes xy, yz, and xz. The magnetization magnitude images are normalized to the target flip angle, meaning that the target magnitude is uniform and equal to 1. The target phase is zero at TE. The OC-based pulse designs (right-most columns) show less over-tipping in the magnitude image and flatter, near-zero phase in the phase image.

Figure 5.8 shows the experimental magnitude and phase images, and the magnitude slab profiles from the STFR acquisitions. Similar to the phantom experiment, the steady-state behavior of the experimental images varies from the single RF excitation simulation (Fig. 5.7) with the presence of undesirable out-of-slab excitation in the magnitude images.

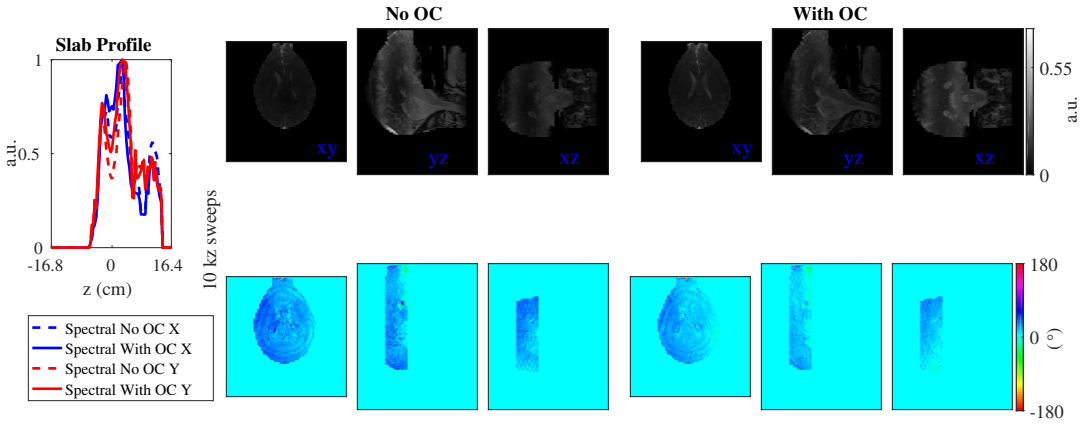

Figure 5.8: In Vivo STFR magnitude images (top row), phase images (bottom row), and mean magnitude slab profiles in the x and y dimensions (left plot) for the two spectral slab-selective pulse designs using an 8 sweep k_z trajectory. For the slab profile plot, the dotted lines indicate pulses designed without OC (just STA approximation), and solid lines indicate with OC. The STFR images are shown for all three imaging planes xy, yz, and xz. The magnitude images are more uniform for the spectral design with OC (right-most columns), along with a sharper slab profile. The phase images are also closer to zero for the spectral design with OC. These STFR images vary from their Bloch simulation images.

5.4.3 Summary of Supporting Information in Appendices

This Chapter has two associated appendices, Appendix B and Appendix C. In addition to the Discussion section, this subsection briefly clarifies the content of each Appendix.

Appendix B provides additional figures and details about spectral slab-selective pulses, and it contains 4 subsections. The first subsection shows an example of a spectral slab-selective RF pulse that is simulated along the entire length of the RF pulse. Here, the intermediate flip angle violates the STA regime which motivates the use of OC for LTA design. The next subsection shows images from the silicone phantom SPGR experiment and describes the details of estimating the inherent and linear coil phase that are removed from our coil-combined STFR images. The next subsection shows additional results from the phantom experiment that did not fit within the Chapter. The final subsection shows an alternative example of a spectral slab-selective pulse designed for a low flip angle and with a peak RF amplitude constraint (rather than an integrated power constraint).

Appendix C shows the results of a spectral-spatial slab-selective extension presented in ISMRM 2018 [17]. These pulses were also designed with a low flip angle and peak RF

amplitude constraint.

5.5 Discussion

The design of spectral slab-selective pulses for the small-tip fast recovery sequence requires consideration of several of details. Here, the magnitude and phase performance of the pulses are equally important: excitation magnitude dictates the slab profile sharpness and uniformity, and excitation phase indicates the spectral prewinding behavior at TE. Additionally, these pulses were used in the STFR sequence, where steady-state behavior is an additional factor that dictates performance. We will first discuss slab-selective prewinding in the context of single RF excitation and then within the steady-state.

Our approach for balancing spectral prewinding and slab selection was to use sweeping k_z sinusodial-like excitation trajectories for pulse design. We tried various number of k_z sweeps empirically and concluded that increased number of sweeps yielded better RF excitation performance in simulation. We reached an upper bound for our number of sweeps with the trajectory design for peripheral nerve stimulation (PNS) concerns. Although we used gradient slew rate limit compatible trajectories, our human volunteer reported moderate PNS stimulation during the in vivo study. The choice of excitation trajectory for spectral slab-selection could be improved in a joint RF-gradient waveform optimization [7],[41],[48], although using that approach for timely on-line pulse design is an unsolved challenge.

We quantitatively evaluated our pulse designs with a 4D Bloch simulation that spanned x,y,z space as well as a Gaussian-weighted spread ([-3σ:3σ], σ=25 Hz) of frequencies associated with the intravoxel spread of spins [61] and typical R2* values within the brain [62]. The performance metrics of interest: magnitude NRMSE and excitation NRMSE over the full volume, phase RMSE within the slab, and mean residual magnetization magnitude after the tip-up served as a means of evaluating RF performance in a single TR (tip-down, free precession, and tip-up). Magnitude NRMSE describes the pulse performance in terms of slab profile and phase RMSE describes the performance in terms of spectral prewinding. Excitation NRMSE balances both of these design requirements. The mean residual magnetization magnitude is important for the context of STFR without RF spoiling, since the tip-up pulse should fully recover magnetization to the longitudinal axis. While the conventional STA pulse design method produced lowest magnitude NRMSE pulses in the phantom, the OC-based approach is better in terms of the other metrics. This is especially true for the residual magnetization, as the non-OC designs leave considerable transverse magnetization after tip-up (Fig. 5.6).

Introducing optimal control perturbations to the pulse design described in Algorithm 2 improved pulse design performance behavior in simulation and in experimental data. This technique provided the RF pulse the flexibility to exceed the small-tip angle regime at intermediate time points along the RF pulse, which occurs for even smaller-tip angles in the STA-based methods (Appendix B Fig. B.1-Fig. B.2). The drawback to OC pulse design is increased computation time. For the spectral slab-selective pulses in this Chapter, the total OC-based pulse design time was slightly less than double the non OC method, but still reasonably short for online pulse design. However, recent extensions to spectral-spatial slab selection [17] (See Appendix C) have faced challenges with the optimal-control pulse design approach, where the increased design dimension to 4D x,y,z, and f leads to pulse designs exceeding 10 minutes, even without OC. Therefore, more efficient programming and refinement of the OC method algorithm could be pursued for feasibility with larger dimensional pulses.

In this Chapter, we designed RF pulses for the STFR sequence with flip angles of θ=16° and found that conservatively constraining RF power made these pulses realizable (in terms of hardware and safety requirements) for phantom and in vivo scans. However in additional experiments, lower flip angles no longer contributed significantly to SAR and could be constrained directly by the peak RF amplitude (Appendix B Fig. B.8-Fig. B.9 and Table B.1). In this case, the simulation performance metrics of a single RF excitation significantly improved from non OC to OC-based methods. However, the lower flip angles (in this case, θ=3.5°) also yielded lower overall signal for STFR. Nevertheless, it is important to consider that there is a subtlety between formulating the pulse design optimization problem with peak RF power or peak RF amplitude constraints. Although we have not found an instance where both RF constraints are active and/or needed, it could be possible that certain circumstances would require both explicit constraints. In this case, a convex optimization algorithm other than FISTA [32] would be required for a more complicated optimization problem.

It is also helpful to evaluate these RF pulses qualitatively from their experimental images acquired with the small-tip fast recovery sequence. Here, we chose to use STFR without RF spoiling which makes it less sensitive to phase mismatch between tip-down and tip-up pulses which can contribute to signal decay [38]. However, without RF spoiling to suppress out-of-slab excitation, imperfections with the RF pulse designs arise in some undesirable magnetization in the steady-state signal (Figs 5.4 and 5.8). This discrepancy between single RF excitation and steady-state behavior is a limitation to our method, and future works would seek to directly design the RF pulse in the full context of STFR at steady-state. An analytical model has been formulated for non-prewinding RF pulses in

terms of flip angle, phase offset between tip-down and tip-up RF pulses, off-resonance, free precession time, gradient crusher time, and T1/T2 times of the object [38]. Future work in slab-selective prewinding pulse design could seek to optimize the pulse for the analytical STFR model.

The spectral prewinding pulses in this paper were only designed to address off-resonance from field inhomogeneity in the object. Fat molecules have a spectrum peak that is 3.5 ppm away from the water spectrum, creating a chemical shift between water and fat signal [78]. While many fat suppression methods exist, including saturation RF pulses, no such techniques were employed in this work. Therefore, it is possible that some unwanted out-of-slab signal seen in experimental in vivo data is attributed to fat signal. Previous work has show that fat saturation preparation pulses can be included successfully in STFR [79], creating an avenue for future work with spectral slab-selective pulses.

Another possible contributor to undesirable out-of-slab excitation in the magnitude images could be imperfections in the excitation gradients. Although the sweeping trajectories were designed to meet the gradient hardware limits in terms of maximum gradient amplitude and slew rate, it is still possible that the trajectory realized by the scanner deviates from the prescribed one. In [Chapter 4], [9] we measured our excitation trajectories using the method of Duyn et al. [67], and the prescribed trajectories matched the measured ones pretty well. However, these trajectories were for a 2D excitation in k_{xy}. Due to the distinct configuration of the G_z gradient coil compared to G_x and G_y, it is possible that our current excitation trajectories could be fallible. This is corroborated by recent work showing that optimized slice-select G_z gradients should be corrected to improve slice profiles in SMS pulse designs [80]. Therefore, an additional future work could be to employ some gradient correction technique, either via a gradient impulse response function (GIRF) [81] or an iterative correction method [66].

5.6 Conclusion

This Chapter combines the utility of slab-selection for 3D imaging and the recent introduction of spectral prewinding pulses [15]. These 2D (z and f) were used in the STFR sequence, where the recovery of spin dephasing with prewinding contributes to a T2/T1 contrast that matches that of bSSFP [55]. This Chapter outlined the details for designing spectral slab-selective as well as highlighted the technical challenges for implementing these designs. For many of these challenges we proposed and implemented solutions, yielding promising initial experimental results. Additional work in improving the experimental behavior of these pulses within the STFR sequence will motivate their use even more.

CHAPTER 6

Future Work

6.1 Direct Power Constraints Based on SAR

Chapter 3 motivated the need for RF pulse designed with direct constraints, and the RF power was an important and common constraint we used throughout the entire thesis. In practice, we wish to constrain the SAR of the RF pulse, which for single transmit RF pulses is proportional to the integrated power or ℓ_2-norm of the RF pulse. The expression for deriving average SAR from [82] is

$$\mathrm{SAR}_{av} = \frac{1}{N_t}\sum_{n=1}^{N_t}\frac{1}{V}\int\frac{\sigma(\mathbf{r})}{2\rho(\mathbf{r})}|\mathbf{E}(\mathbf{r}, n\Delta t)|^2 dv \tag{6.1}$$

for N_t time points of an RF pulse over a volume V with spatially-varying conductivity $\sigma(\mathbf{r})$, density $\rho(\mathbf{r})$ and $\mathbf{E}$ is the electic field.

For our power constraints, we estimated the SAR units empirically from reference scans. In other words, we scanned using an RF pulse with known Eulcidean norm (proportional to integrated power) for a test sequence with fixed TR and RF pulse length and recorded the SAR readings (both 10-second and 6-min) from the scanner. We then used this reading to gauge where to set the integrated power constraint for future designs to be used within the same scan. These values were set conservatively, and often the 10-second SAR limits were only roughly half-way reached and the 6-minute limits hardly registered on the scanner monitor. This suggests that our constraints are perhaps too conservative and that the design performance is potentially impeded by these tight limits. *Therefore, a useful future work would be to set power constraints directly based on SAR.*

Using the expression for SAR (Eq. (6.1)), other groups have designed RF pulses with direct SAR constraints, primarily in pTx applications where SAR requirements are more difficult to calculate and enforce compared to single transmit [83],[84],[85]. In these cases, a k_T-point [86] or spokes [51] trajectory is often employed, where SAR constraints are of

the quadractic form [84],

$$\sum_{s=1}^{S} \mathbf{b}_s^H \mathbf{Q}(\mathbf{r}) \mathbf{b}_s \leq \text{SAR Constraint (Local, Global)} \tag{6.2}$$

where S is the number of k_T points or spokes and $\mathbf{Q}$ is the SAR matrix. $\mathbf{Q}$ can only be calculated with known $\mathbf{E}$ fields, which are normally derived from electromagnetic simulation [83]. The additional need for appropriate electromagnetic models increases the computational complexity of direct SAR constraints, even if just with single transmission. Moreover, an active question in the MRI community is whether SAR is an accurate constraint, when ultimately power deposition is controlled to limit temperature change within the body [87].

An additional challenge for setting power constraints for RF pulse design is that there is a deviation between the "predicted" SAR for a given RF pulse, TR, and scan time and the actual "monitored" SAR on the scanner. Each time that an object is placed in the scanner, the initial localizer scan calibrates the transmit and receive gains based on the specific conductivity properties of the object, that vary person to person and also based on the settings for that unique scan session. Even knowing the "predicted" SAR models used by our GE scanner and approximate subject weight, there is a major discrepancy between the SAR that is predicted and what is measured on the monitor. This an open line of work that we have begun exploring with some initial results shown in Figure 6.1 where two, consecutive 90° pulses were played out for increasing TR's. Here we find that the predicted SAR only yields roughly 28% of the measured SAR in both the FBIRN phantom and in a human volunteer. *These results again warrant future work in setting the RF power constraint*.

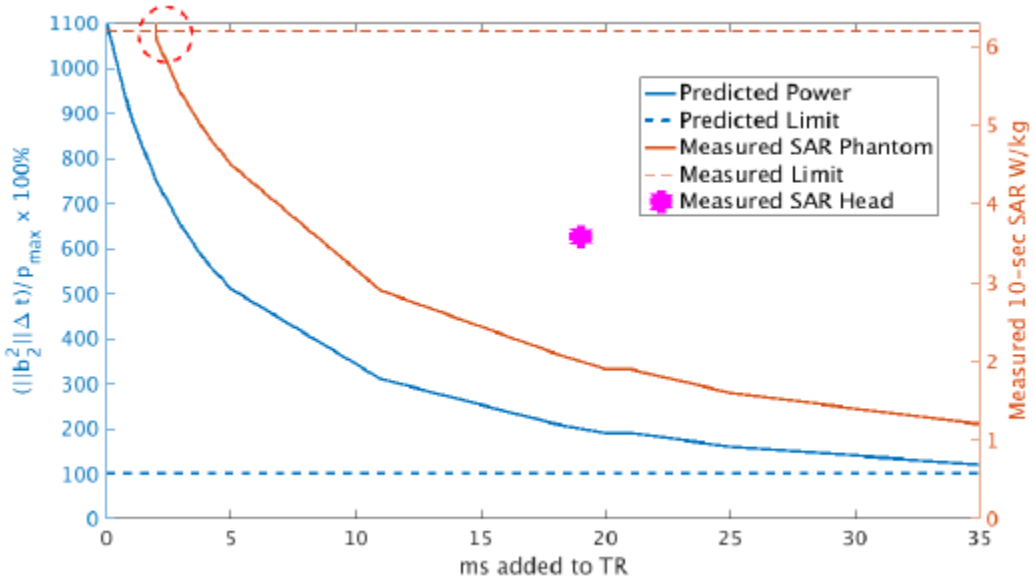

Figure 6.1: On the left hand side (blue plots), we show the percent of the predicted power limit our RF pulse/TR length pair should deposit. For all of these TR's we are above the predicted limit (100%). On the right hand side, we plot the measured SAR deposited as read by the SAR monitoring meter during the scan in the FBIRN phantom. This was read for the 10-sec SAR monitoring only, and as plotted, the majority of values falls below the 6.4 W/kg limit. The circled red region highlights when the sequence has surpassed the monitored shutoff (6.4 W/kg) and no measurements are collected. Here, we also scanned in the human brain as plotted by the pink data point. There, for a 19 ms additional TR the measured SAR in the brain was 3.6 W/kg, and for the same pulse/TR pair was 2.0 W/kg in the phantom.

6.2 Further Work on SMS Constrained RF Pulses and 3D Experimental Acquisition

Chapter 3 Section 3.3.3 explored the idea of minimizing out-of-slice error in SMS pulse designs with set in-slice error constraints, as well as peak amplitude and integrated power physical RF hardware constraints. Compared to the peak- and power-contrained SMS designs (Sections 3.3.1-3.3.2), the minimum out-of-slice error formulations produced less ripple in the out-of-band regions as was expected. However, there appears to be a tradeoff between the in-slice excitation profile and the supression of out-of-slice ripple. An interesting extension of this work could explore this relationship more carefully. Furthermore, the characteristics of the "don't care" transition region was not fully investigated and warrants additional exploration.

To fully implement the SMS pulses in Chapter 3, there is a need for developing a full SMS acquisition scheme to acquire a full 3D volume. This is not a novel endeavor by any means ([52],[53]), and currently the fMRI lab conducts many MB studies for various outside research groups. Unfortunately, the GE vendor-provided SMS methods are currently not open source for research purposes.

To conduct a 3D SMS with custom constrained RF pulses, it would be necessary to implement a Blipped-CAIPI [53] acquisition scheme either directly in the GE pulse sequence programming method, or Dr. Jon-Fredrik Nielsen's TOPPE framework [88]. The reconstruction could then be adapted from code found open source online from many groups, such as Dr. Berkin Bilgic from MGH. *Further investigation of SMS constraints and their tradeoffs, in addition to a 3D acquisition experiment, could provide beneficial gains in a clinical SMS application such as fMRI or cardiac imaging.*

6.3 Spectral and Spectral-Spatial Prewinding Pulse Designs with Multiple RF Constraints

Chapter 3 demonstrates the design of SMS pulses with multiple constraints, although the prewinding pulses handled in Chapters 4 and 5 were only solved with one RF constraint, in most cases an integrated power constraint. In Appendix B, we also explore a peak-constrained formulation for a lower flip-angle design of spectral slab-selective pulses. What we did not explore was the intermediate cases, in which perhaps both a peak amplitude and integrated power constraint could be active. This seems even more likely in the spectral-spatial slab-selective pulse case (Appendix C), because the power deposition of these pulses in experiments was measured lower on the scanner monitor. Therefore, there could be a bigger intersection space between power and peak amplitude constraints.

In discussing prewinding pulse constraints, a few other interesting RF constraints could be explored (in addition to peak amplitude and integrated power). For one, the intermediate flip angle could be constrained based on a STA approximation of transverse magnetization (related to flip angle by $\sin(\alpha)$) at time points along the length of the RF pulse. In Chapter 5 the intermediate flip angle violation of the STA regime was what motivated an OC-based LTA design. Although, if one wanted to keep the pulse design within STA, perhaps to facilitate a least-squares optimization problem with many convex constraints, this intermediate flip angle constraint could be of use.

Another prewinding-pulse constraint could enforce the phase of intravoxel spins to be the same, while allowing for flexibility or variation in phase across different voxels. This

approach would be somewhat similar to a magnitude least-squares approach to pulse design in the prewinding case [51], but so far has not been implemented. This is because we have designed prewinding pulses in the STFR sequence, where the steady-state behavior is dictated by the relationship between tip-down and tip-up pulses. It remains unclear how to allow for intervoxel phase relaxation in a tip-down pulse without complicating or worsening the tip-up design. Possibly, a joint tip-down and tip-up design as described in Ref. [38] could overcome this challenge.

The underlying challenge in designing these prewinding pulses with multiple constraints is that these pulses are multi-dimensional (2D, 3D, 4D) and therefore are too large to be optimized using 2nd-order software such as CVX [35]. Provided that a suitable solver was found to use—that also did not involve parameter tuning—online computation for these pulses is an open problem. *In general, further investigation into multiple constraints for prewinding pulses is required.*

6.4 Joint Design of RF and Excitation K-Space Trajectory

Chapters 4 and 5 both discussed the need for an optimized excitation trajectory to pair with general spectral-spatial and slab-selective prewinding pulses. The joint design of optimal k-space trajectories and RF pulses is an open and challenging problem. Recent work by Sun et al. [7], Malik et al. [40], and Davids et al. [41] have sought to solve the joint design problem for the application of inner-volume excitation. *A future work could focus on the joint optimization of the k-space/gradient trajectory and RF waveforms for prewinding pulses*.

What makes joint RF/gradient particularly challenging for prewinding pulses is that these pulses occur online, tailored to the patient-specific field map. Therefore, the pulse optimization time must be kept minimal as to limit subject motion and general discomfort. To my knowledge, the published joint design methods are too expensive for online pulse design. They also have the potential of falling into local minima and not the optimal solution during alternating minimization schemes. A general idea that could work at addressing this computation problem is to pre-compute a set of "universal" excitation trajectories for prewinding pulses that are derived from jointly optimized RF/gradient waveforms using previously acquired field maps. Ideally, these "universal" pulses would be generalizable enough for use in online prewinding pulse design. This idea originates from the universal pTx pulses introduced in Ref. [89] for calibration-free pTx scanning at 7T.

A final extension would be to consider the joint design of the slice-select gradient for constrained SMS pulse design, a novel approach taken recently by Rund et al. [48].

6.5 Fully 3D Spectral-Spatial Prewinding Pulses

A final future work that has a strong relationship to the joint RF/gradient waveform design (Section 6.4) is 3D spectral-spatial imaging. In essence, this is an extension of Chapter 4 but to the entire 3D x,y,z coverage of the object, not just a select slab as in Chapter 5. To be able to design a spectral-spatial pulse in 3D, the excitation trajectory must be chosen particularly carefully. Natural trajectory choices would be options such as stack of spirals [90], SPINS [91] and k_T points [86] as explored in Ref. [7]. However, as in the 2D and slab-selective spectral-spatial cases, it is likely that a joint RF/gradient design would yield enhanced performance. As shown in Appendix C, these pulse designs face significant computational challenges as their dimension size increases. Combining a 3D spectral-spatial design with a joint excitation gradient design at this point seems especially challenging for online purposes. *Despite the computational challenges, a fully 3D spectral-spatial prewinding pulse could be an interesting area of future work.*

APPENDIX A

Supporting Information for 2D Spectral-spatial Prewinding Pulses

A.1 Local spectral-spatial bandwidth as a model for intravoxel dephasing

A.1.1 Spatially varying bandwidth

Choosing a local bandwidth L to design spectral-spatial pulses faces multiple competing demands. On one hand, a wider bandwidth L might balance the competing needs of spatial resolution and pulse length, allowing the prewinding pulse to capture larger range of off-resonance. On the other hand, a wider L could increase SAR, making the RF optimization problem more challenging and lead to overall worse prewinding performance. This section explores a few design considerations for local bandwidth L and concludes that simply using a uniform L =25 Hz is sufficient for the spectral-spatial pulses designed in Chapter 4.

One possible alternative is to adapt L to changing ΔB_0 offset based on [4], which noted that there is proportionality between off-resonance frequency $f(x, y)$ and through-plane gradient g_z. This can be expressed as

$$g_z = \alpha f(x, y) \tag{A.1}$$

where α is the proportionality constant. In [4], α was estimated from contiguous field maps as -2.03×10^{-4} G/cm/Hz. We therefore chose to explore through-plane contributions to intravoxel bandwidth spread using $\alpha = -2 \times 10^{-4}$ G/cm/Hz. We did this by adapting the local bandwidth spatially considering through-plane gradient effects [4] by applying the following equation:

$$L_{\mathrm{tp}}(x, y) = \gamma \alpha \Delta z |\Delta f(x, y)| \quad . \tag{A.2}$$

Here $L_{\text{tp}}(x, y)$ is the spatially varying local bandwidth attributed to the through-plane gradient, γ is the gyromagnetic ratio, and $\Delta z = 0.4$ cm was the slice thickness used in the 3D field map acquisition. We also centered the field map $\Delta f(x, y)$ to a median value of 0 Hz. Using Eq. (A.2) alone would cause spatial locations at or close to the median field map frequency to have a through-plane local bandwidth value of about 0 Hz. Furthermore, at the farthest field map deviation value of 129 Hz, Eq. (A.2) would yield $L_{\text{tp}} = 44$ Hz. We chose to balance the contribution of through-plane gradient and the original uniform $L = 25$ Hz. We associate the 25 Hz bandwidth with microscopic effects of T2* decay, whereas the through-plane dephasing proportional to ΔB_0 is related to macroscopic effects. These effects are largely independent and thus are treated as orthogonal sources of bandwidth spread. This leads to a quadrature combination, so the final spatially varying $L_{\text{total}}(x, y)$ we investigated is:

$$L_{\text{total}}(x, y) = \sqrt{(\gamma \alpha \Delta z |\Delta f(x, y)|)^2 + 25^2} \quad . \tag{A.3}$$

We then incorporated this spatially varying bandwidth $L_{\text{total}}(x, y)$ into the design through the weighting matrix. To design an RF pulse using Eq. (A.3), the weighting matrix **W** contained samples of

$$w(x, y, f) = \begin{cases} 1, & |f - \Delta f(x, y)| \leq \frac{L_{\text{total}}(x,y)}{2} \\ 0, & \text{otherwise} \quad . \end{cases} \tag{A.4}$$

See Fig. A.1 for an illustration that compares Eq. (A.4) (Fig. A.1 bottom row) to the original fixed bandwidth design in Eq. [5] of [9] (Fig. A.1 top row).

A.1.2 Gaussian weights in the design weighting matrix

These two implementations of **W** (spatially varying and uniform $L_{\text{total}}(x, y)$) are binary weighting matrices, where the only weight values used are 0's and 1's. We also investigated using Gaussian weights instead of binary weights in the design weighting matrix so it matches the Gaussian weight model used in calculating the performance metrics, e.g., Excitation NRMSE. In this case, the values of $w(x, y, f)$ included in the matrix are scaled to normalized Gaussian weights as

$$w(x, y, f) = \begin{cases} \frac{g(f;x,y)}{\max(g(f;x,y))}, & |f - \Delta f(x, y)| \leq 3L_{\text{total}}(x, y) \\ 0, & \text{otherwise} \end{cases} \tag{A.5}$$

where $g(f; x, y)$ is the Gaussian weight at frequency f. We define $g(f; x, y)$ as

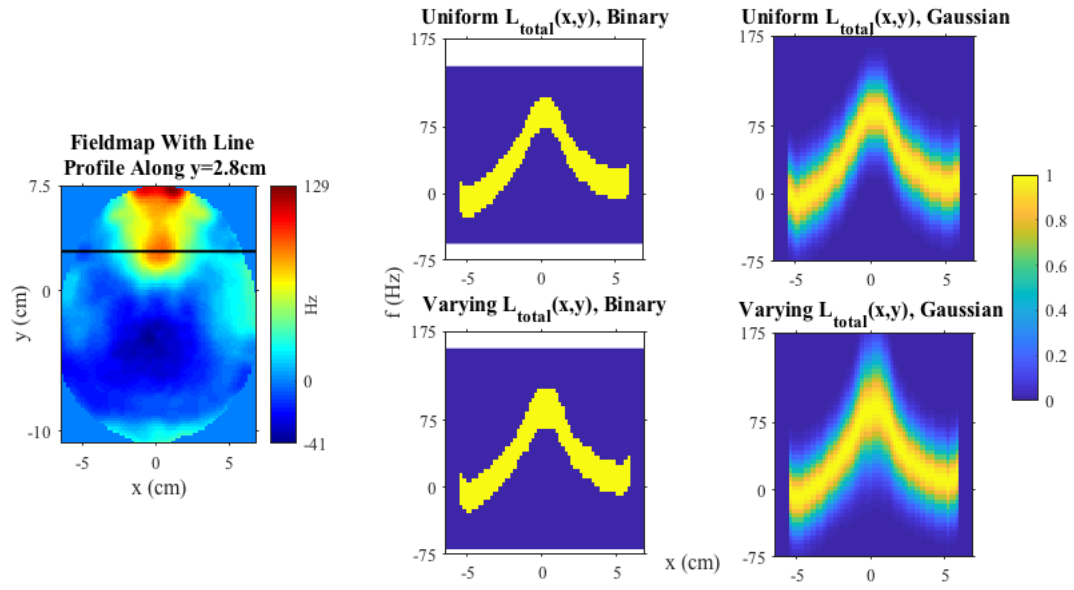

Figure A.1: Four possible design weighting matrices **W** for spectral-spatial pulse prewinding. In the top row, the intravoxel bandwidth spread is universally $L_{\text{total}}(x, y)$ =25 Hz at all locations. In the bottom this value varies spatially with the spread proportional to through-plane gradient. In the left column, the values included in **W** are binary (0's or 1's). In the right column, the values are weighted by a normalized Gaussian distribution. In [3], we used the top left design weighting matrix.

$$g(f; x, y) = \frac{1}{L_{\text{total}}(x, y)\sqrt{2\pi}} \exp\left[-\frac{(\bar{f}(x, y) - f)^2}{2L_{\text{total}}(x, y)^2}\right] \tag{A.6}$$

where $\bar{f}(x, y)$ is the mean frequency within the $L_{\text{total}}(x, y)$ bandwidth region at location (x, y) and the standard deviation $L_{\text{total}}(x, y)$ can also be uniform or spatially varying for the Gaussian weights.

In total, we investigated the design of spectral-spatial pulses with 4 unique weighting matrices **W**: binary entries (Eq. (A.4)) with i) uniform $L_{\text{total}}(x, y)$ =25 Hz intravoxel spread or ii) spatially varying spread $L_{\text{total}}(x, y)$ defined in Eq. (A.3), and Gaussian-weighted entries (Eq. (A.5)) with iii) uniform $L_{\text{total}}(x, y)$ =25 Hz intravoxel spread and 25 Hz standard deviation or iv) spatially varying spread $L_{\text{total}}(x, y)$ and spatially varying standard deviation. Figure A.1 illustrates these distinct design weighting matrices. Each box of Fig. A.1 represents a sampled frequency f and the plots are shown in spatial dimension x, y. To further investigate this approach, all simulation results use a finer spectral sampling rate of Δf =5 Hz (Δf =10 Hz was used in [9]).

A.1.3 Spatially varying standard deviation in Bloch simulation

For completeness, we also considered a refinement of the simulation methods. In [9], we used an intravoxel frequency spread in Bloch simulation spanning a [-3σ:10:3σ] Hz range, where σ =25 Hz defined the standard deviation of normalized Gaussian distribution weights **g** used to combine these simulation results. Just like we considered spatially varying intravoxel widths for **W** of our spectral-spatial pulse design, we could simulate over ranges with spatially varying standard deviation $L_{\text{total}}(x, y)$ similar to Eq. (A.3). Hence, we now have two methods for multi-frequency Bloch simulation: normalized Gaussian weights with a uniform standard deviation and a spatially varying standard deviation.

A.1.4 Results

To facilitate our forthcoming discussion, Table A.1 summarizes these design/simulation combinations and provides shorthand variable naming conventions for each possible combination of design matrix and simulation method.

Table A.1: Possible combinations of design weighting matrices (columns) and simulation methods (rows) for spectral-spatial pulse design. The original method presented in [3] is assigned the naming convention "$\mathbf{BU}_L\mathbf{U}_{\text{std}}$".

		Design Weight Matrix Method			
		Binary **W** with Uniform $L_{\text{total}}(x, y)$	Binary **W** with Varying $L_{\text{total}}(x, y)$	Gaussian **W** with Uniform $L_{\text{total}}(x, y)$	Gaussian **W** with Varying $L_{\text{total}}(x, y)$
Methods	Gaussian with Uniform Standard Deviation	$\mathbf{BU}_L\mathbf{U}_{\text{std}}$	$\mathbf{BV}_L\mathbf{U}_{\text{std}}$	$\mathbf{GU}_L\mathbf{U}_{\text{std}}$	$\mathbf{GV}_L\mathbf{U}_{\text{std}}$4
Simulation	Gaussian with Varying Standard Deviation	$\mathbf{BU}_L\mathbf{V}_{\text{std}}$	$\mathbf{BV}_L\mathbf{V}_{\text{std}}$	$\mathbf{GU}_L\mathbf{V}_{\text{std}}$	$\mathbf{GV}_L\mathbf{V}_{\text{std}}$

We explored designing four sets of spectral-spatial pulses (using four weighting matrix methods) and simulated their performance with both simulation methods for the fieldmap

shown in Fig. A.1. One of these combinations, "$\mathbf{BU}_L\mathbf{U}_{\text{std}}$", is used in [9] (albeit with 10 Hz rather than 5 Hz spacing for the design). Table A.2 lists the performance of all 8 design/simulation combinations with the naming conventions provided in Table A.1.

Table A.2: Possible combinations of design weighting matrices (columns) and simulation methods (rows) for spectral-spatial pulse design. The original method presented in [3] is assigned the naming convention "$\mathbf{BU}_L\mathbf{U}_{\text{std}}$".

Design Simulation Method	Excitation NRMSE	Phase RMSE (°)	Mean Magnitude	% Magnitude St. Dev.	Magnitude NRMSE
$\mathbf{BU}_L\mathbf{U}_{\text{std}}$	**0.18**	7.4	**0.24**	7.8	**0.14**
$\mathbf{BV}_L\mathbf{U}_{\text{std}}$	**0.18**	**7.0**	**0.24**	**7.0**	**0.14**
$\mathbf{GU}_L\mathbf{U}_{\text{std}}$	0.29	8.0	0.20	7.8	0.26
$\mathbf{GV}_L\mathbf{U}_{\text{std}}$	0.32	8.1	0.20	11.1	0.31
$\mathbf{BU}_L\mathbf{V}_{\text{std}}$	0.21	8.8	**0.24**	11.4	0.17
$\mathbf{BV}_L\mathbf{V}_{\text{std}}$	0.21	8.0	**0.24**	9.9	0.17
$\mathbf{GU}_L\mathbf{V}_{\text{std}}$	0.31	9.8	0.20	10.4	0.28
$\mathbf{GV}_L\mathbf{V}_{\text{std}}$	0.33	9.3	0.20	12.5	0.31

We expected the performance metrics, particularly excitation NRMSE and phase RMSE, to worsen when simulation methods went from using a Gaussian spread of intravoxel frequencies with uniform standard deviation σ to a spatially varying spread where σ increased at areas of higher off-resonance due to through-plane effects. Supporting Table A.2 shows where performance drops slightly from design/simulation combinations ending in "$\mathbf{XXU}_{\text{std}}$" to "$\mathbf{XXV}_{\text{std}}$". It was harder to predict how adjusting the design weighting matrix would affect the spectral-spatial pulse performance. Table A.2 reports decreases in performance for design weighting matrices when adjusting from binary to Gaussian weight values ("**BXX**" to "**GXX**"). There are negligible differences when comparing uniform and varying $L_{\text{total}}(x, y)$ in the weight matrix ("$\mathbf{XU}_L\mathbf{X}$" to "$\mathbf{XV}_L\mathbf{X}$"). This is likely because changing the design weight matrix from binary to Gaussian weights increases the support of $\mathbf{W}$ in the frequency dimension, resulting in a more challenging RF design. The magnitude simulation images (Fig. A.2) and phase simulation images (Fig. A.3) are visually consistent with the fact that the various design alternatives yield similar results but with a slight decline for some explored methods for this particular slice.

In conclusion, we explored modifying the weighting matrix used in designing spectral-spatial pulses by i) varying the design target bandwidth $L_{\text{total}}(x, y)$ to reflect the propor-

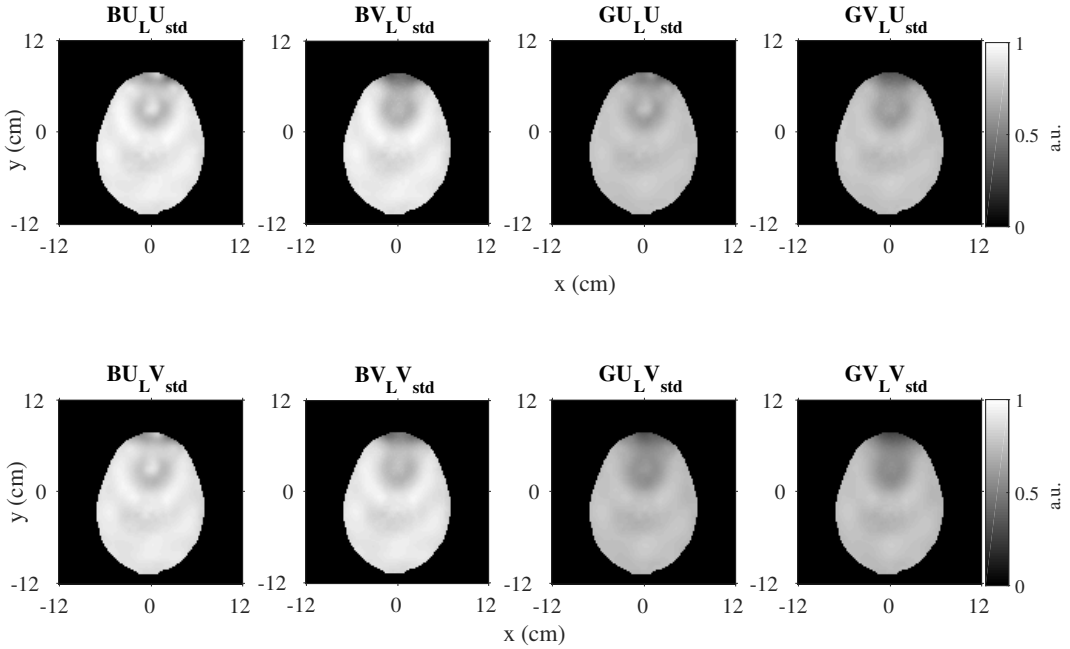

Figure A.2: Simulated magnitude images for all possible design weighting matrix and simulation combinations presented in Table A.1

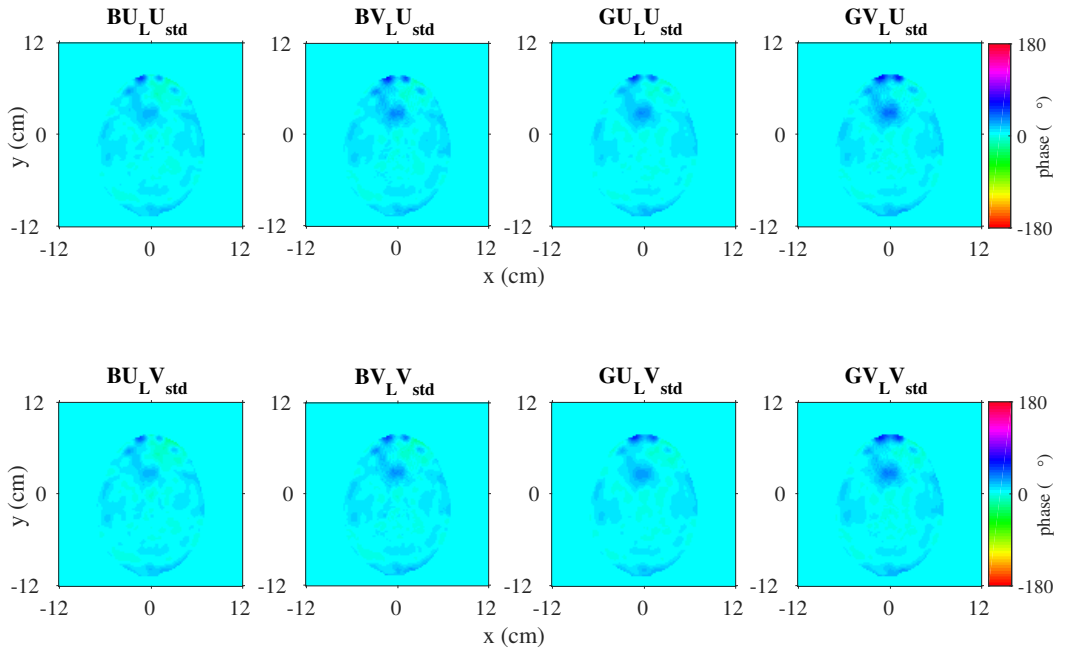

Figure A.3: Simulated phase images for all possible design weighting matrix and simulation combinations presented in Table A.1

tionality between off-resonance and through-plane gradient using references such as [4] and ii) varying the weights of the design weighting matrix to be Gaussian rather than binary. We also went further and investigated simulation methods where we varied the standard deviation of the Gaussian intravoxel spread of frequencies to be spatially varying with off-resonance. After testing all possible combinations, we saw only small changes in simulation performance metrics. It is possible that with higher spatial resolution excitation k-space trajectories we might see greater gains with these modifications. However, this would also mean a longer RF pulse, so the potential advantages of these changes is unclear.

A.2 Hard pulse simulation and prewinding pulse performance over one frequency and one spatial dimension

In [9] we compare spectral and spectral-spatial prewinding pulses, building on previous work in [15] and [55]. In this section of Appendix A, we also compare these to the performance of a non-prewinding pulse. In this case, we simulate a simple 500 μs hard rect pulse that has the same TE and flip angle as our human spectral and spectral-spatial RF pulse designs (3.648 ms/ 16°). Table A.3 below reports performance metrics (Eq. 4.13-4.17 in Chapter 4) for this hard pulse and the spectral and spectral-spatial pulses. As expected, the hard pulse has a uniform magnetization appearance but does not reach the target magnitude (% magnitude standard deviation, magnitude NRMSE) and fails to acheive a flat phase profile since no prewinding has occured (phase RMSE, excitation NRMSE).

Table A.3: Performance metrics defined in [3] (Chapter 4 Eq. 4.13-4.17) for a simulated hard pulse in comparison to purely spectral and spectral-spatial prewinding pulses. The **bold** values represent the best performance.

Pulse	Excitation NRMSE	Phase RMSE (°)	Mean Magnitude	% Magnitude St. Dev.	Magnitude NRMSE
Hard pulse	0.64	43.5	**0.24**	**0.1**	**0.13**
Purely spectral pulse	0.54	25.2	0.17	19.6	0.39
Spectral-spatial pulse	**0.18**	**7.0**	**0.24**	7.7	0.15

In addition to the performance metrics provided, we have created plots to demonstrate the performance of prewinding pulses as a function of one spatial dimension and frequency before summation using Gaussian weights. To do this, we selected a particular "y" location in the 2D in vivo field map and drew a line profile spanning all "x" through it. We then examined the magnetization of both purely spectral and spectral-spatial pulses across this line profile for all frequencies included in Bloch simulation. Finally, we repeated this same process for one "x" location and the corresponding "y" line profile.

Figure A.4 shows the magnetization simulations for one spatial dimension and all simulation frequencies for the hard pulse. The simulations are presented in terms of relative complex error ($|\frac{m_{xy}}{\sin\alpha} - 1|$), absolute phase error ($|\angle m_{xy}|$), and relative magnitude error ($|\frac{|m_{xy}|}{\sin\alpha} - 1|$). This diagram also shows the 2D human field map, simulated magnitude, and simulated phase over all combined frequencies using a Gaussian distribution with σ =25 Hz as described in Chapter 4. Figures A.5 and A.6 repeat these plots for the purely spectral and spectral-spatial pulse, respectively.

The hard pulse plots in Fig. A.4 agree with the performance metrics in Supporting Table A.3 in that the pulse performs poorly with large absolute phase error and relative magnitude and complex error across all space. As anticipated, the spectral-spatial pulse in Fig. A.6 tracks the spatially varying off-resonance while the purely spectral pulse in Fig. A.5 does not. The purely spectral pulse has low phase error values for some spatial locations, but with varying off-resonance it cannot enforce low relative complex at all frequencies. Meanwhile, the spectral-spatial pulse maintains particularly low relative complex error with spatial variation. We therefore conclude that both effective magnitude *and*

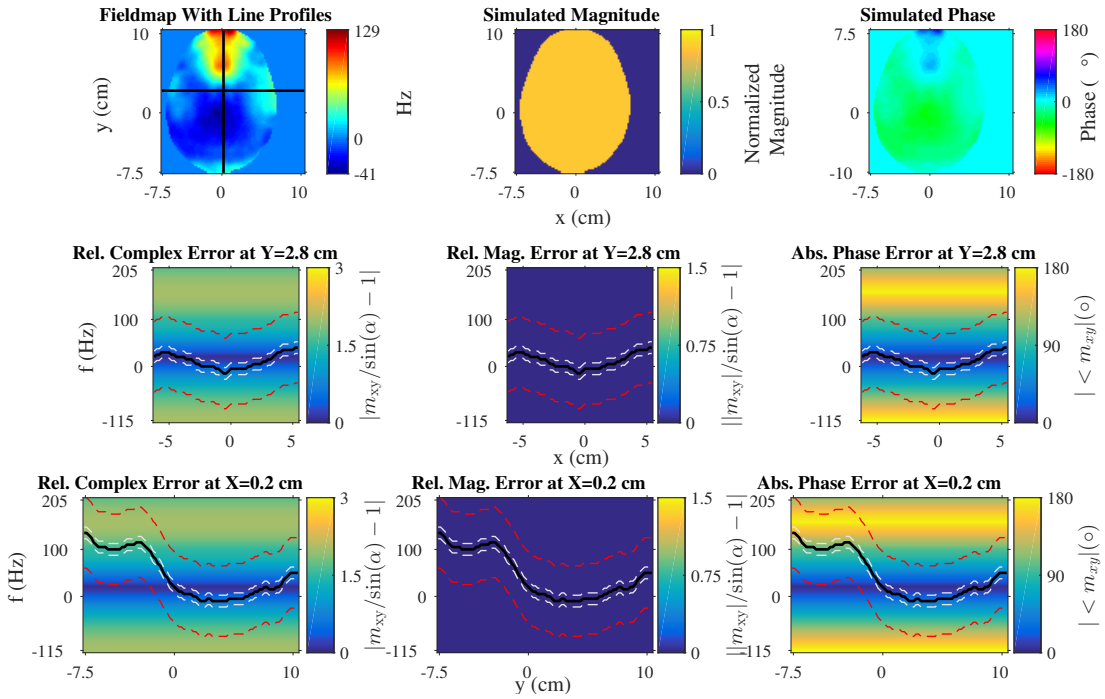

Figure A.4: Hard pulse simulation results. Top row: 2D field map (left), simulated magnitude (center), and simulated phase (right). Middle row: relative complex error, relative magnitude error, and absolute phase error for the 1D line profile magnitude across all x at y =2.8 cm. Bottom row: relative complex error, relative magnitude error, and absolute phase error for profile across all y at y =0.2 cm. The dashed white lines represent the L =25 Hz used as the local bandwidth for the spectral spatial pulse, and the dashed red lines represent the $\pm 3\sigma$ = 75 Hz bandwidth used in Bloch simulation. These plots are repeated for the spectral and spectral-spatial pulses in Fig. A.5 and Fig. A.6.

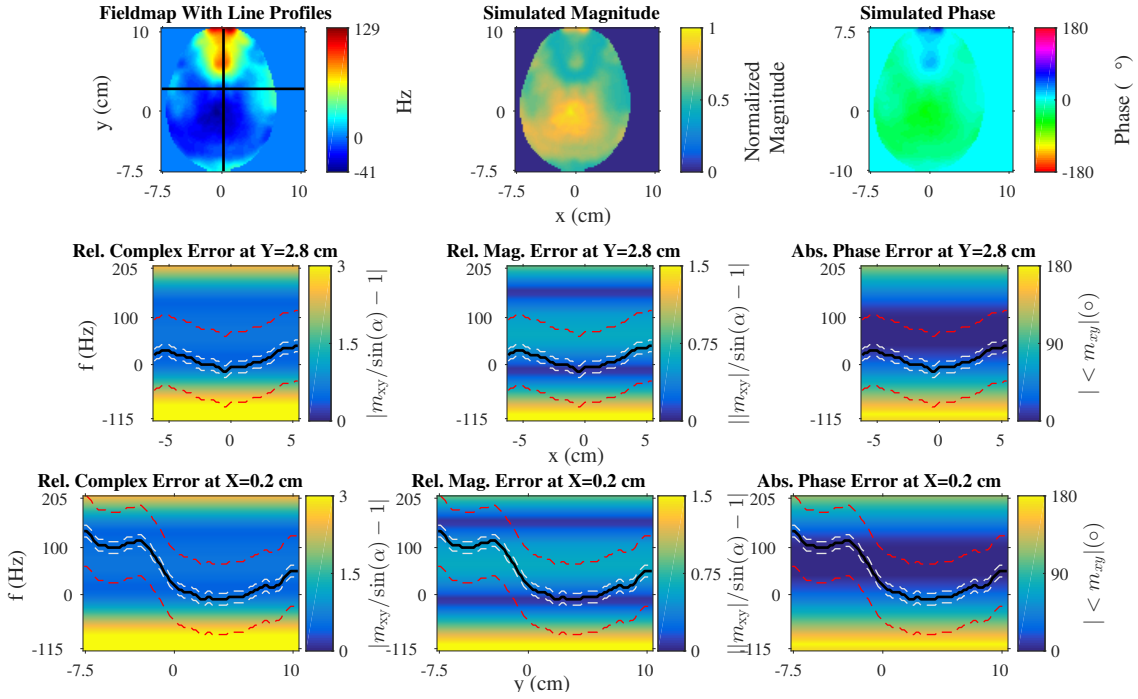

Figure A.5: Purely spectral pulse simulation results. Compare with Fig. A.4 and Fig. A.6.

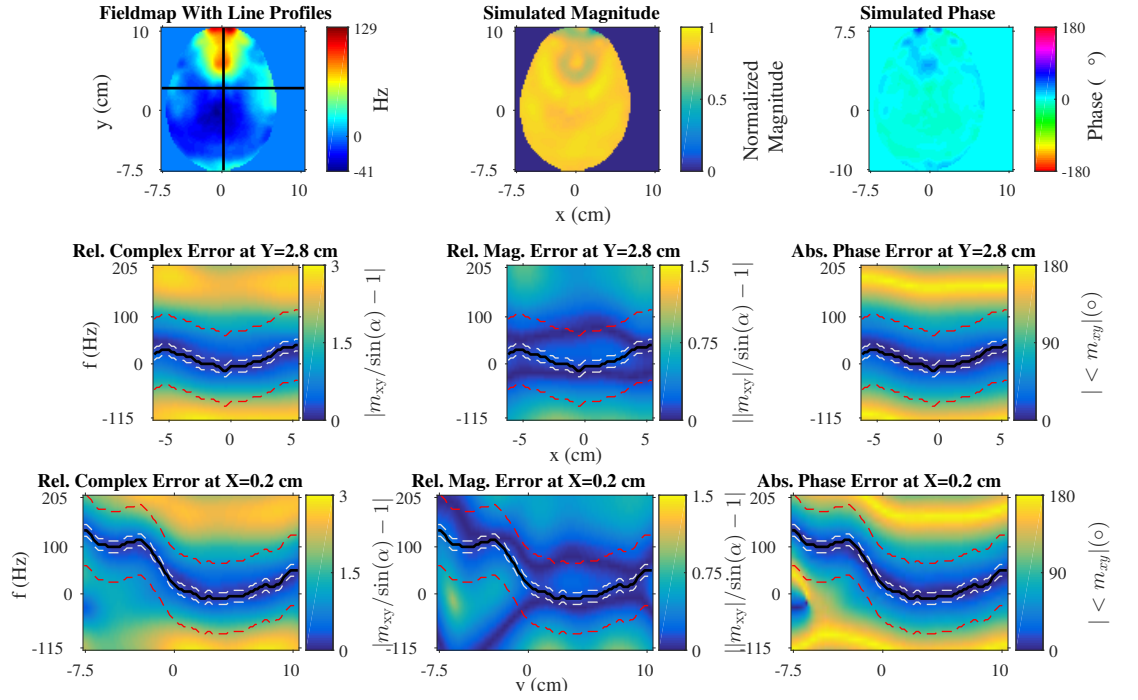

Figure A.6: Spectral-spatial pulse simulation results. Compare with Fig. A.4 and Fig. A.5.

phase performance (in other words, the relative complex error) is what leads to effective prewinding. The summed frequency simulation of these three pulses in the 2D simulated magnitude and phase images are consistent with these performance differences as well.

Additional intuition about pulse performance can be gained by plotting "error" as a function of spatial location. Figure 7 in [9] shows excitation and phase root squared error combined across all simulated frequencies as a function of spatial location for the purely spectral pulse and spectral-spatial pulse. There, we can easily see that the hard pulse performs very poorly, the spectral pulse performs moderately well, and the spectral-spatial pulse performs has the lowest phase errors.

APPENDIX B

Supporting Information for Slab-Selective Prewinding Pulses

This Appendix provides additional information about spectral slab-selective pulses that support the findings reported in Chapter 5.

B.1 Intermediate Flip Angle Simulations

Our initial attempts for solving STA spectral slab-selective pulses yielded results that performed poorly in Bloch simulation (in terms of NRMSE and residual tip-up magnetization magnitude in a tip-down + tip-up pair of STFR). It was ultimately determined that, despite a small target RF flip angle much less than 90°, the RF pulse exceeded the STA regime at intermediate time points along the length of the ∼3.5 ms RF pulse. This violation led to the need for LTA-based designs using OC. Figures B.1 and B.2 show the Bloch simulation of intermediate flip angle for a spectral slab-selective pulse that breaks the STA approximation at spin locations within the excited slab.

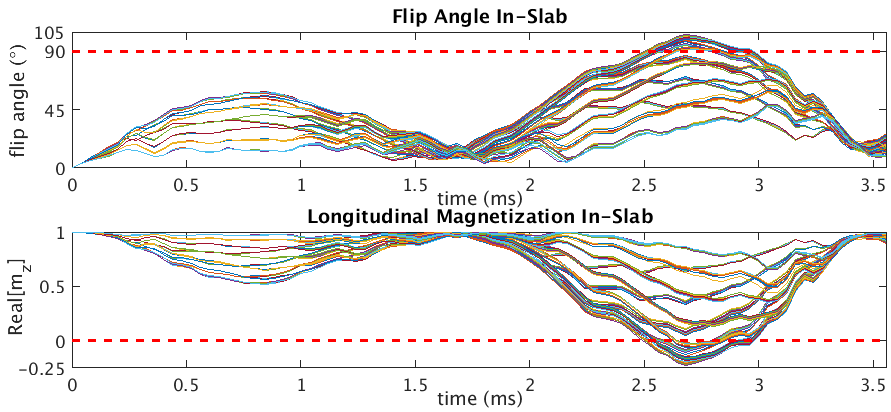

Figure B.1: Intermediate flip angle (top) and longitudinal magnetization mz for a subset of within-slab spins along the length of a spectral slab-selective RF pulse excitation designed under the small-tip angle approximation. Although the pulse lands around a small target flip angle of 16°, the spins surpass 90° (red dotted line) at intermediate time points indicating that the STA approximation is invalidated. Meanwhile, the longitudinal magnetization even goes below m_z =0, suggesting that inversion is even occurring.

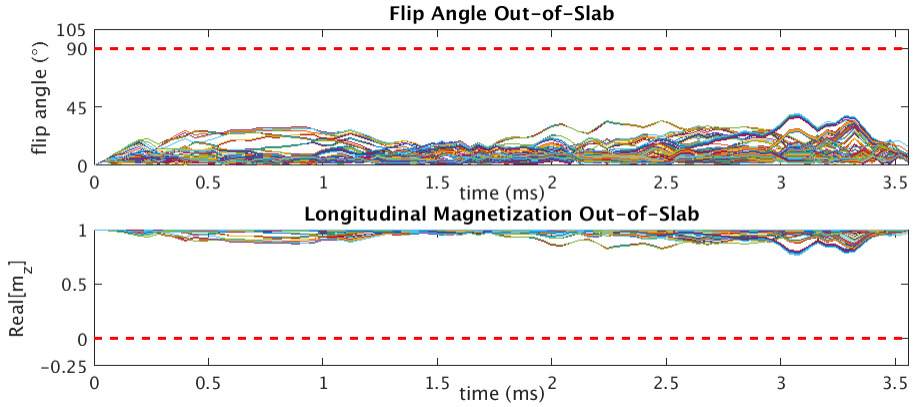

Figure B.2: Intermediate flip angle (top) and longitudinal magnetization m_z for a subset of out-of-slab spins from the same spectral slab-selective pulse simulated in Figure B.1. Here, there should be very little transverse excitation (flip angle $\sim$0°, m_z $\sim$1)

B.2 Inherent and Linear Coil Phase Estimates in a Silicone Phantom

Chapter 5 Sections 5.3.3 and 5.3.6 describe the method for which the coil-combined phase images were produced for spectral prewinding pulses in STFR. After complex coil

combination using Roemer's coil combination with reference sensitivity maps [76], an inherent object phase was computed by removing off-resonance phase contributions and a residual linear phase plus constant offset. This linear phase plus constant offset term was computed using a reference scan on a Silicone phantom. The Silicone phantom has very low conductivity so provides a uniform signal intensity across the center of the phantom. This is in contrast to the FBIRN phantom, which mimics conductivity properties in the human brain. The FBIRN phantom conductivity creates varying signal intensity (particularly, a bright center) that impairs the linear phase estimate. In Figure B.3 we show the original field map of the silicone phantom in the shimmed B0 field, the TE=0 ms phase image of the silicone phantom with the contribution of field map phase removed, the estimated magnitude-weighted least-squares fit of the linear phase plus constant offset term from the TE=0 ms image, and a comparative spin echo image with that estimated linear phase remove. The spin echo image, by definition, should have near-zero phase after all processing, which it does.

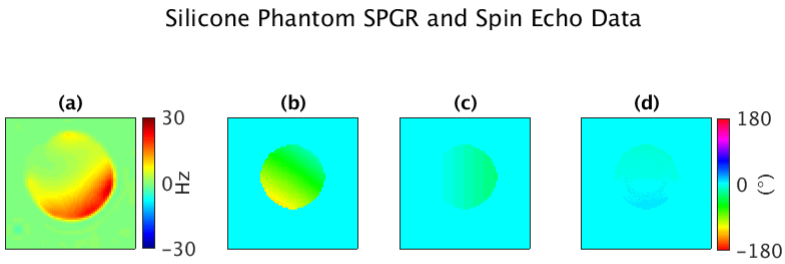

Figure B.3: Experimental data from reference silicone phantom scan at the center slice (isocenter). (a): Field map for shimmed magnetic field, (b): TE=0 ms phase image (inherent object phase) from SPGR acquisition with off-resonance accumulation removed, (c): the least-squares fit (weighted by magnitude image) of the residual linear phase plus constant offset term seen in the TE=0 ms image that is eventually removed, and (d): spin echo phase image with inherent object phase and linear phase removed.

B.3 Additional Phantom Simulation and Experimental Data

Figures B.4 and B.5 show the simulated magnetization magnitude and phase images for the various trajectories explored in slab-selective spectral pulse design, 6, 8, and 10 k_z sweeps. These simulations correspond to the experimental images shown in Fig. 5.4 and

Fig. 5.5 in Chapter 5.

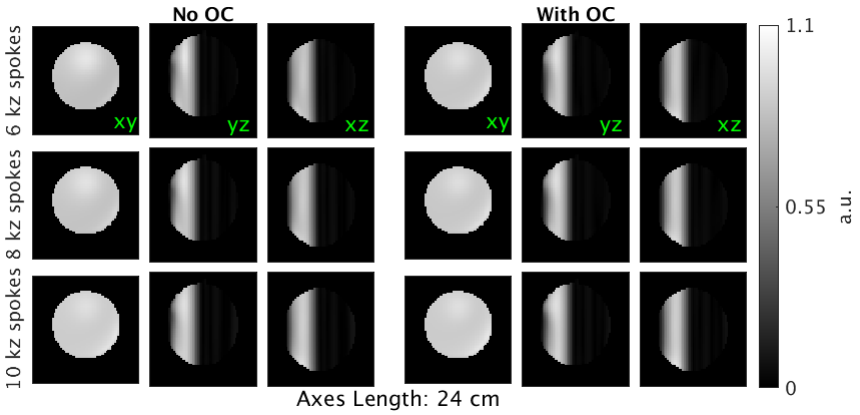

Figure B.4: Simulation magnetization magnitude at TE normalized to the target flip angle θ=16° for the FBIRN phantom with susceptibility artifact. (top): spectral slab-selective pulses for 3 k_z trajectories without OC, (bottom): spectral slab-selective pulses for 3 k_z trajectories with OC.

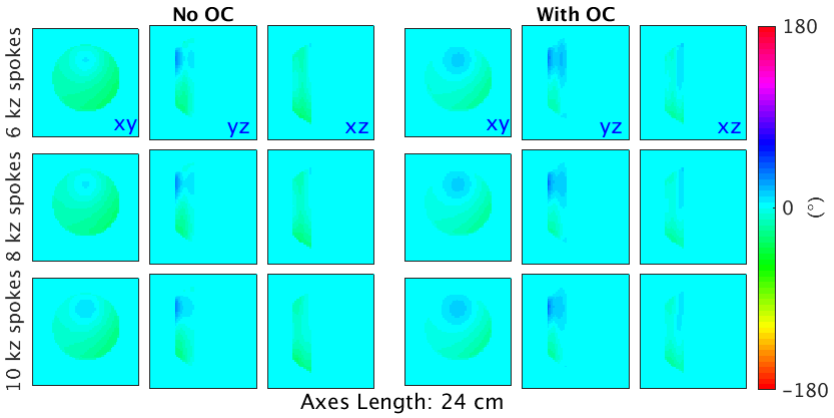

Figure B.5: Simulation magnetization phase at TE for the FBIRN phantom with susceptibility artifact. (top): spectral slab-selective pulses for 3 k_z trajectories without OC, (bottom): spectral slab-selective pulses for 3 k_z trajectories with OC.

Furthermore, Figures B.6 and B.7 show the simulated X and Y profile for the same phantom studies (varying k-space trajectory design for spectral slab-selection) in both simulation and experimental STFR.

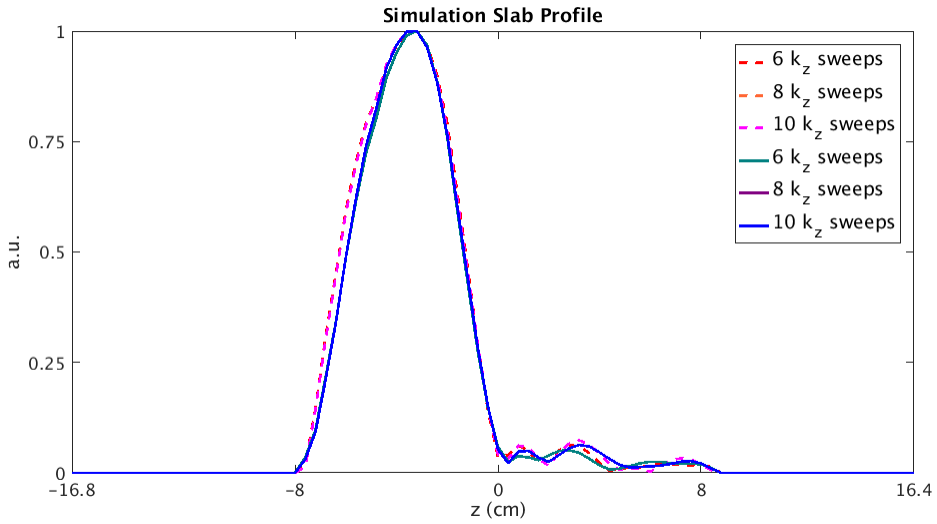

Figure B.6: Slab profiles across for simulated magnetization magnitude of prewinding pulses for the FBIRN phantom. Pulses designed with optimal control are plotted in solid lines and those designed without are plotted in dotted lines.

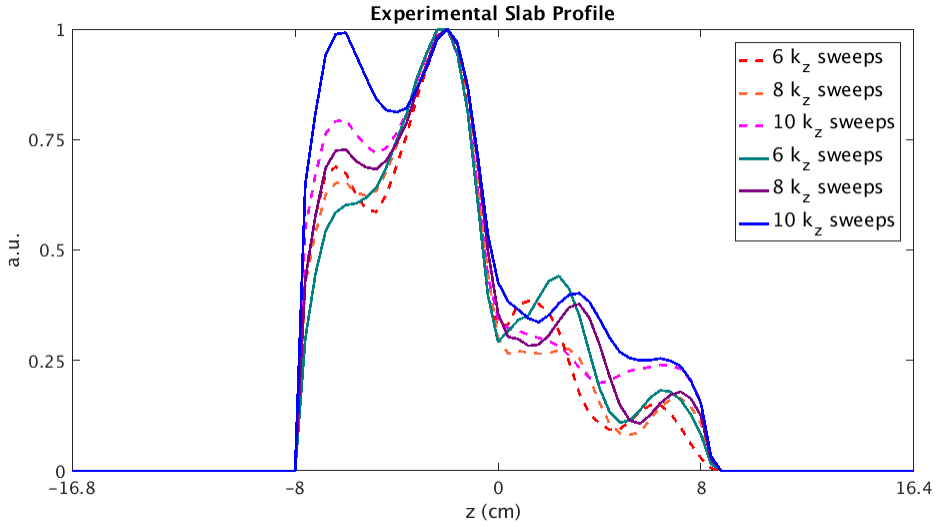

Figure B.7: Slab profiles for experimental magnitude images acquired with prewinding pulses in STFR in the FBIRN phantom. Pulses designed with optimal control are plotted in solid lines and those designed without are plotted in dotted lines.

B.4 Peak-Constrained Spectral Slab-Selective Pulse for Very Small Flip Angles

In this section, we investigate a spectral slab-selective RF pulse design for a lower flip angle of 3.5° where the peak amplitude constraint is dominant. As was seen with the power-constrained pulses in Chapter 5, pulse performance is improved greatly when using OC.

Table B.1: Design comparison for in vivo slab-selective prewinding pulses for a flip angle of 3.5° and with peak amplitude RF constraint, with and without additional optimal control perturbation updates. The best performance for each measure is in **bold** font.

RF Pulse Design	Design Time (min:sec)	Mag. NRMSE	Phase RMSE (°)	Excitation NRMSE	Residual $\lvert M_{xy,\mathrm{tip-up}}\rvert$
Spectral, 8 kz sweeps, no OC	**0:24**	0.29	22.8	0.46	0.19
Spectral, 8 kz sweeps, with OC	0:55	**0.19**	**11.4**	**0.26**	**0.03**

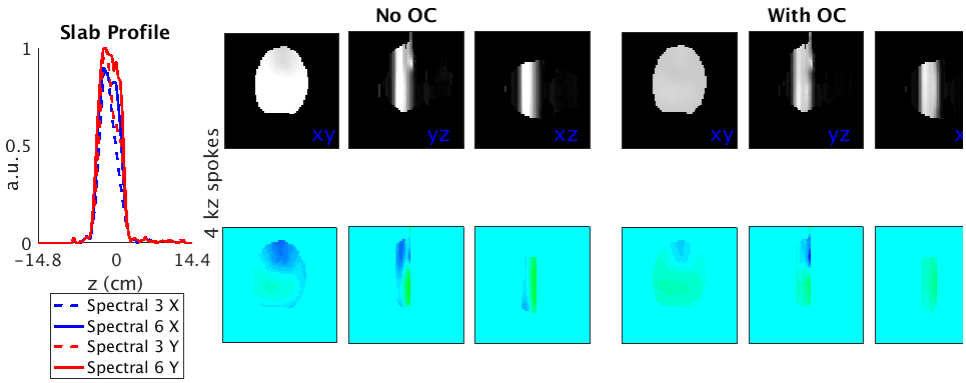

Figure B.8: In vivo Bloch simulation echo time magnetization magnitude (top row), phase (bottom row), and mean slab profile in the x and y dimensions (left plot) for the two spectral slab-selective pulse designs using an 8 k_z sweep trajectory. For the slab profile plot, the dotted lines indicate pulses designed without OC (just STA approximation), and solid lines indicate with OC. Simulated magnetization is shown for all three imaging planes xy, yz, and xz. The magnetization magnitude images are normalized to the target flip angle, meaning that the target magnitude is uniform and equal to 1. The target phase is zero at TE. The OC-based pulse designs (right-most columns) show less over-tipping in the magnitude image and flatter, near-zero phase in the phase image.

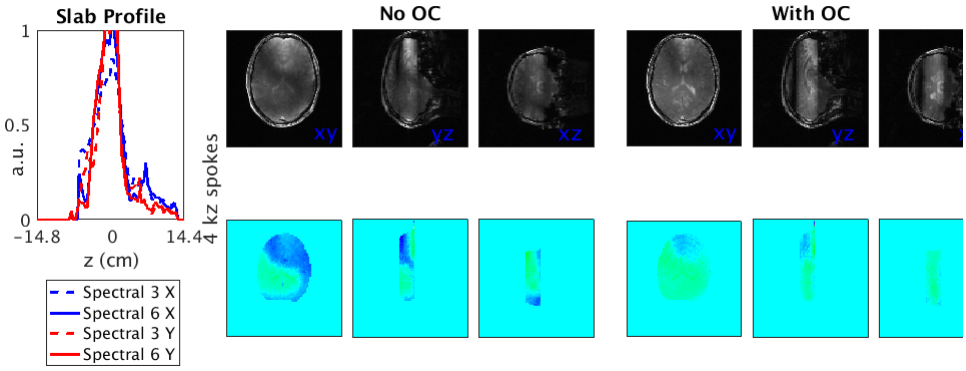

Figure B.9: In Vivo STFR magnitude images (top row), phase images (bottom row), and mean magnitude slab profiles in the x and y dimensions (left plot) for the two spectral slab-selective pulse designs using an 8 k_z sweep trajectory. For the slab profile plot, the dotted lines indicate pulses designed without OC (just STA approximation), and solid lines indicate with OC. Simulated magnetization is shown for all three imaging planes xy, yz, and xz. The magnetization magnitude images are normalized to the target flip angle, meaning that the target magnitude is uniform and equal to 1. The target phase is zero at TE. The OC-based pulse designs (right-most columns) show less over-tipping in the magnitude image and flatter, near-zero phase in the phase image.

APPENDIX C

Spectral-spatial Slab-Selective Prewinding Pulses

Slab-selective prewinding pulses were introduced in Chapter 5 for a 2D pulse design spanning the z,f space. In this Appendix, we expand the slab-selective prewinding to a spectral-spatial pulse that covers x,y,z,f. The motivation is drawn from Chapter 4, in that we expect a spectral-spatial variant to leverage a larger effective rephasing bandwidth. In this proof-of-concept work, we show that spectral-spatial slab-selective pulses do have small performance gains, but are also limited by computation costs for 4D designs. This work was presented at the 2018 ISMRM Annual Meeting in Paris [17].

C.1 Theory

For the spectral-spatial pulses, we solve a peak-constrained STA problem (Eq. (3.2)) by replicating the slab-selective prewinding target pattern in Equation 5.1 over x and y to 4D

$$d(x,y,z,f) = p(z)\mathrm{e}^{2\pi i \mathrm{TE} f} \tag{C.1}$$

with associated matrix $\mathbf{W}$ formed by sampling a function extended from Eq. (5.2),

$$w(x,y,z,f) = \begin{cases} 1, & \Delta f(x,y,z) - \frac{L}{2} \leq f \leq \Delta f(x,y,z) + \frac{L}{2} \text{ and } z \in z_{\text{in}} \bigcup z_{\text{out}} \\ 0, & \text{otherwise.} \end{cases} \tag{C.2}$$

As done previously, we define L as an additional bandwidth acounting for the intravoxel spread of spins, and z_{in} and z_{out} are the in-slab and out-of-slab regions, respectively.

C.2 Methods

C.2.1 Excitation K-Space

For the original case of spectral-spatial prewinding pulses [Chapter 4],[9], variable density spiral trajectories were used to encode the spatially-varying recovery bandwidth in the transverse k_x-k_y plane. Empirically, it was shown that repeating the spiral a few times during the excitation pulse was beneficial to prewinding performance. Some intuition behind these pulses is that the spectral prewinding behavior occurs when the pulse is passing through the center of k-space, and then time outside of the center provides the spatial information. However, by repeating trajectories, less time is available to attain further k_{xy} extent which determines in-plane resolution. In the transverse plane, it was assumed that the field map was smoothly varying, so minimal (0.1-0.2 $\frac{\text{cycles}}{\text{cm}}$) k-space extent was sufficient.

As mentioned in Chapter 5, there is an apparent competing need between slab-selectivity and spectral prewinding with the k_z trajectory. This challenge is even greater when needing to cover k_{xy} as well. We chose to use spokes excitation trajectories [65] as a means of meeting the spectral-spatial slab-selective needs. Spokes locations and overall trajectory design remains an open and challenging problem, especially when done jointly with RF pulse design (see Chapter 6 Section 6.4). In this Appendix, we used spokes that were longer in the k_z dimension and sparsely covered the $k_{x,y}$ plane through 5 spokes, with the initial spoke at k-space center, (k_x, k_y)=(0,0). We tried variations of the other 4 spoke locations, either at (k_x, k_y)=$(\pm k_{xy,\max}, 0)$ and (k_x, k_y)=$(0, \pm k_{xy,\max})$ or at (k_x, k_y)=$(\pm k_{xy,\max}, \pm k_{xy,\max})$ where $k_{xy,\max}$=$0.11\frac{\text{cycles}}{\text{cm}}$, or an in-plane resolution of $\sim$9 cm. For all variations, the spokes trajectories were repeated two times during the single RF excitation pulse, leading to a total RF pulse length of 5.04 ms. We compared to a purely spectral slab-selective pulse (Chapter 5), where only the k_z component of the spokes trajectories (consisting of multiple sweeps) was used. Figure C.1 shows a plot of these spokes excitation trajectories in 3D, along with the gradient and k-space waveforms. These trajectories were parameterized to meet gradient amplitude and slew-rate constraints by solving a B-splines basis function parameterization described in [7] with the an efficient constrained optimization problem in CVX software [35].

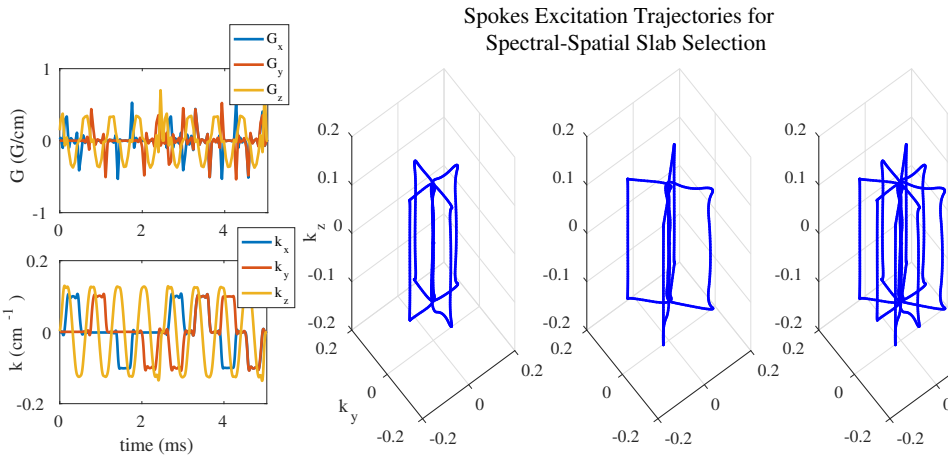

Figure C.1: Spokes trajectory variations used during excitation for the spectral-spatial slab selective pulse. The left-hand plots show the gradient and k-space waveforms vs time, and the center and right-hand plots show the spokes trajectories in 3D k-space. The first (Spokes^1) and second (Spokes^2) trajectories repeat the same spokes pattern twice, while the third (Spokes^3) trajectory plays out one of each.

C.2.2 RF Pulse Design and Experiments

The spectral-spatial slab-selective pulses were designed with peak amplitude constraints (Eq. (3.2)) for all three spokes variants (Fig. C.1) and compared to same-length spectral slab-selective pulses with just the G_z gradient of the spokes trajectory. Similar to Appendix B Section B.4, these pulses were designed for a low flip angle of 3.5° where peak amplitude is unequivocally the dominant RF constraint. Due to computational costs, the OC-based design for spectral-spatial pulses (Algorithm 2) was not implemented online during in vivo experiments, only offline in simulation. This is because computation time for these pulses is on the order of 30-60+ min, which is prohibitively long. This is even with coarse sampling (16x16) in the transverse xy plane. In fact, computation time is a major limiting factor with spectral-spatial slab-selective pulses.

The same general imaging protocol described in Chapter 5 was followed for comparing slab-selective spectral and spectral-spatial pulses. A few design variants (i.e., different spokes trajectories) were tested in the phantom with susceptibility artifact, and one was tested in vivo.

C.3 Results

Table C.1 reports simulated performance metrics for comparative spectral and spectral-spatial slab-selective designs for the phantom with susceptibility artifact. The spectral-spatial slab-selective pulses have better excitation NRMSE and phase RMSE behavior while the spectral slab-selective pulses perform better in terms of magnitude NRMSE, residual magnetization after tip-up, and total design time.

Table C.1: Design comparison for spectral and spectral-spatial prewinding pulses designed for the phantom with and without the additional optimal control perturbation updates. Metrics shown include: total design time, magnitude NRMSE, phase RMSE, excitation NRMSE, and mean residual transverse magnetization magnitude after tip-up. The "best" performance for each measure is in **bold** font.

Slab Selective RF Pulse Design	Design Time (min:sec)	Mag. NRMSE	Phase RMSE (°)	Excitation NRMSE	Residual $\lvert M_{xy,\text{tip-up}}\rvert$
Spectral, no OC	**0:40**	0.63	66.2	1.38	0.23
Spectral, with OC	1:17	**0.23**	12.0	0.30	**0.04**
Spectral-spatial, no OC, Spokes[1]	8:50	0.24	9.5	0.29	0.09
Spectral-spatial, no OC, Spokes[2]	8:40	0.25	8.9	0.28	0.09
Spectral-spatial, no OC, Spokes[3]	8:33	0.25	9.8	0.30	0.10
Spectral-spatial, with OC, Spokes[2]	37:23	**0.23**	**6.7**	**0.25**	0.09

Spokes[1]= spokes at (k_x, k_y)=$(\pm k_{xy,\max}, 0)$ and (k_x, k_y)=$(0, \pm k_{xy,\max})$
Spokes[2]= spokes at (k_x, k_y)=$(\pm k_{xy,\max}, \pm k_{xy,\max})$
Spokes[3]= spokes at (k_x, k_y)=$(\pm k_{xy,\max}, 0)$
and (k_x, k_y)=$(0, \pm k_{xy,\max})$
and (k_x, k_y)=$(\pm k_{xy,\max}, \pm k_{xy,\max})$

Figure C.2 shows the experimental magnitude and phase images for the phantom study. Here, the Spokes[2] (see Table C.1) is shown. Both spectral and spectral-spatial pulses were scanned with pulses designed without and with an OC-based design. The experimental images are visually similar, and it is harder to see the difference in magnitude and phase performance as evaluated in simulation in Table C.1.

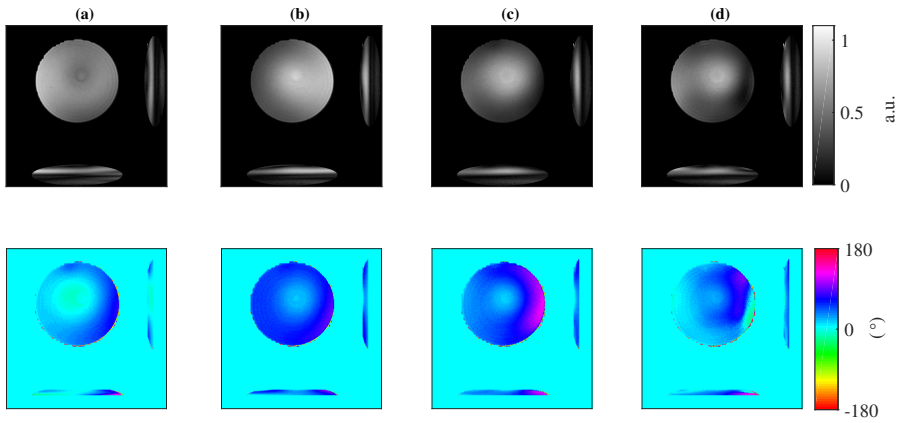

Figure C.2: Experimental magnitude (top row) and phase (bottom row) images from coil-combined 8-channel STFR acquisition. (a): Spectral slab-selective pulse without OC, (b): Spectral slab-selective pulse with OC, (c): Spectral-spatial slab-selective pulse without OC, and (d): Spectral-spatial slab-selective pulse with OC.

Table C.2 reports simulated performance metrics for comparative slab-selective spectral and spectral-spatial designs for the in vivo experiment. Spectral slab-selective pulses without and with OC and spectral-spatial pulses without OC were realized in experiments, the spectral-spatial with OC pulses were designed and simulated after the fact. Interestingly, the spectral slab-selective pulse with OC out performed both spectral-spatial designs (with and without OC) for every metric other than phase RMSE.

Table C.2: Design comparison for spectral and spectral-spatial prewinding pulses designed for the human volunteer with and without the additional optimal control perturbation updates. Only the spectral pulse with OC and spectral-spatial pulse without OC were used in experiments, the other pulses were designed and simulated later. Metrics shown include: total design time, magnitude NRMSE, phase RMSE, excitation NRMSE, and mean residual transverse magnetization magnitude after tip-up. The "best" performance for each measure is in **bold** font.

RF Pulse Design	Design Time (min:sec)	Mag. NRMSE	Phase RMSE (°)	Excitation NRMSE	Residual $\lvert M_{xy,\mathrm{tip-up}}\rvert$
Spectral, no OC	**0:26**	0.37	29.7	0.56	0.19
Spectral, with OC	0:55	**0.22**	12.3	**0.29**	**0.03**
Spectral-spatial, no OC, Spokes^2	13:16	0.27	11.1	0.31	0.11
Spectral-spatial, with OC, Spokes^2	72:23	0.28	**8.7**	0.30	0.12

Figure C.3 shows the simulated magnetization magnitude and phase as well as the experimental magnitude and phase images for spectral slab-selective pulse designed without OC for the human volunteer. Dotted lines on the magnitude images delineate the design slab region.

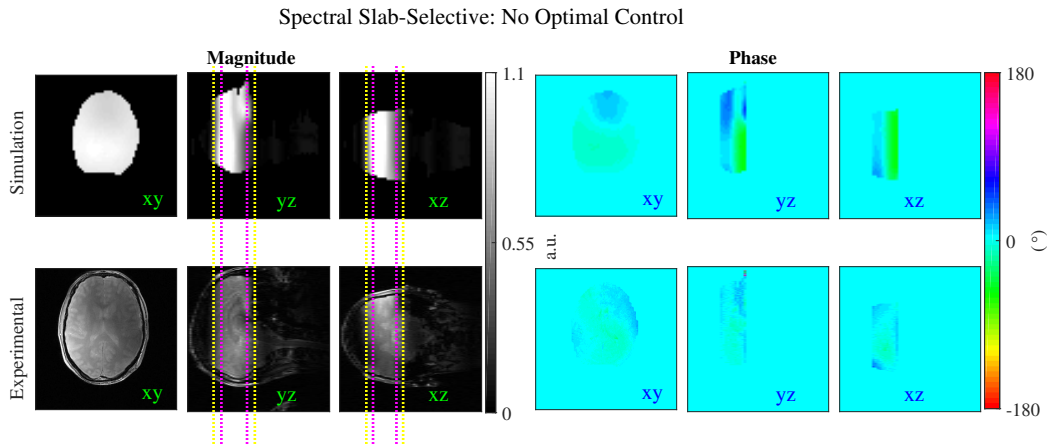

Figure C.3: Bloch simulated magnitude and phase (top row) and experimental magnitude and phase images from coil-combined 8-channel STFR acquisition (bottom row) for the spectral slab-selective pulse designed without OC. Dotted purple lines show the slab region, while yellow dotted lines show the "don't care" transition region between in-slab and out-of-slab.

Figure C.4 shows the simulated magnetization magnitude and phase as well as the experimental magnitude and phase images for spectral slab-selective pulse designed with OC for the human volunteer. Again, the lines show the design slab region.

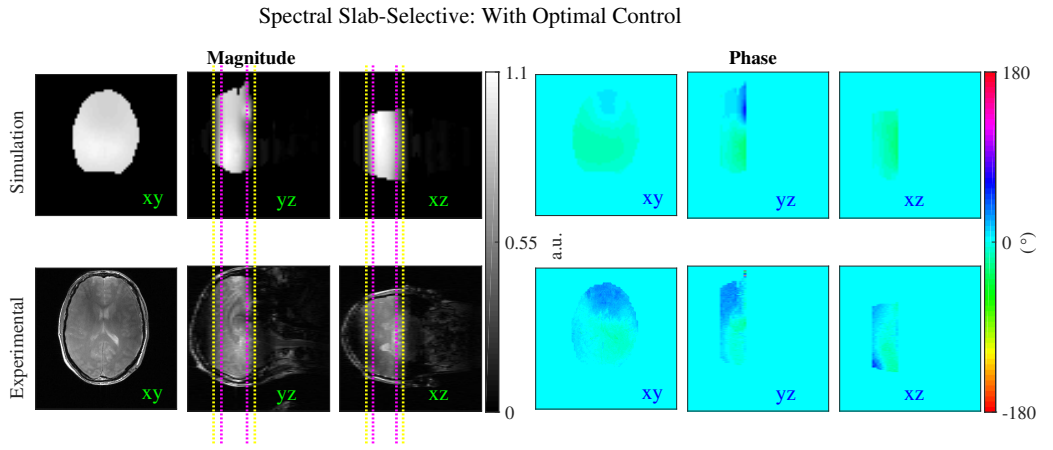

Figure C.4: Bloch simulated magnitude and phase (top row) and experimental magnitude and phase images from coil-combined 8-channel STFR acquisition (bottom row) for the spectral slab-selective pulse designed with OC. Dotted purple lines show the slab region, while yellow dotted lines show the "don't care" transition region between in-slab and out-of-slab.

Figure C.5 shows the simulated magnetization magnitude and phase as well as the experimental magnitude and phase images for spectral slab-selective pulse designed with OC for the human volunteer.

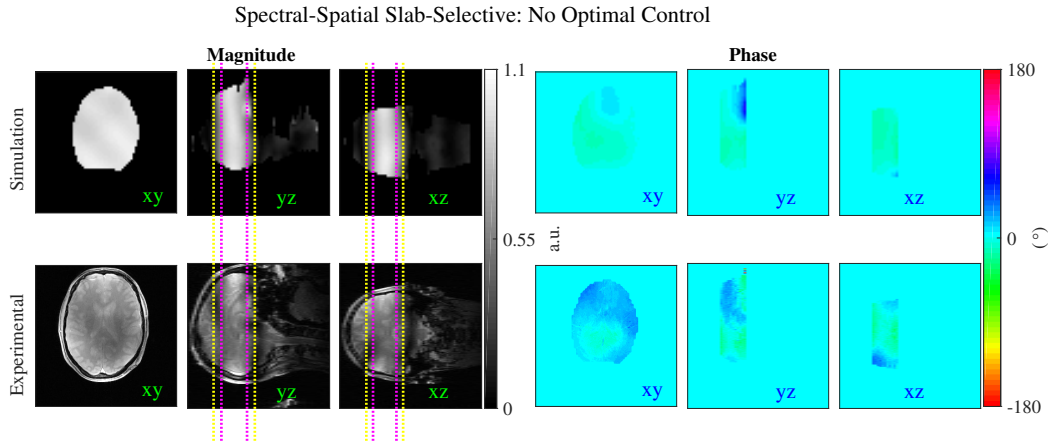

Figure C.5: Bloch simulated magnitude and phase (top row) and experimental magnitude and phase images from coil-combined 8-channel STFR acquisition (bottom row) for the spectral-spatial slab-selective pulse designed without OC. Dotted purple lines show the slab region, while yellow dotted lines show the "don't care" transition region between in-slab and out-of-slab.

Figure C.6 shows the simulated magnetization magnitude and experimental magnitude slab profiles for both the spectral and spectral-spatial slab-selective pulses used in the in vivo experiment.

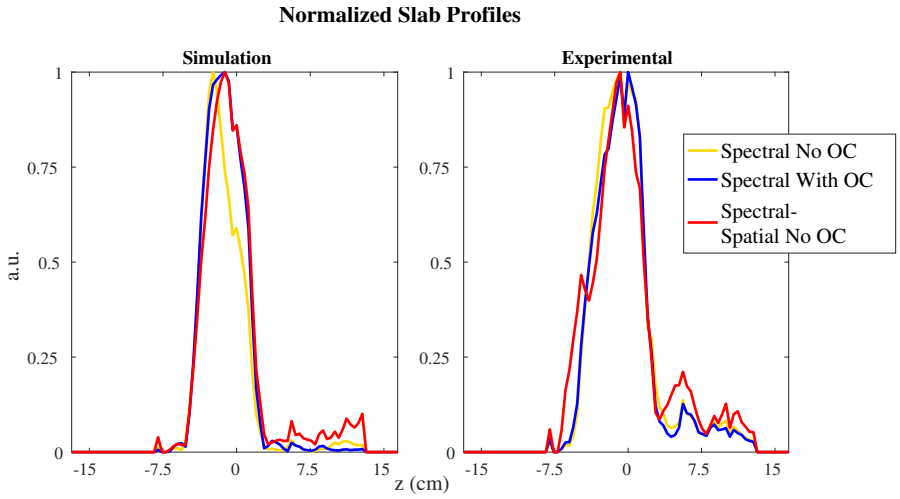

Figure C.6: Simulated (left) and experimental (right) magnitude slab profiles for the spectral and spectral-spatial slab-selective pulses used in the in vivo experiment.

C.4 Discussion and Conclusion

In the phantom experiments comparing spectral and spectral-spatial slab-selective pulses (Table C.1 and Figure C.2), we see that the spectral-spatial pulses only provide moderate improvement over the spectral slab-selective pulse designed with OC. This is mostly in terms of phase RMSE, which suggests that the prewinding behavior is improved with spectral-spatial designs. Interestingly the spectral slab-selective pulse with OC seems to outperform the spectral-spatial slab-selective pulses in terms of magnitude NRMSE and residual magnetization after tip-up. Spectral-spatial pulses with OC can only begin to match this at the expense of nearly 40 min of computation time. The experimental phantom images are slightly inconclusive, yet we can say that the phase images seem to flatten with spectral-spatial pulses designed using optimal control.

A similar trend is seen with the in vivo experimental results. Interestingly the spectral slab-selective pulse designed with OC outperforms spectral-spatial pulses *with OC* in every metric other than phase RMSE. Furthermore, the in vivo results for spectral-spatial pulses (Fig. C.3-C.5) show more out-of-slab excitation than even the spectral slab-selective pulse designed without OC. We especially note this in the slab profile plots (Fig. C.6).

In concordance with somewhat lackluster experimental results, we also discuss the significant computation cost of spectral-spatial slab-selective pulses compared to their spectral counterparts. The spectral-spatial slab-selective pulses designed without the benefits of OC updates took at times an order of magnitude longer to design compared to the spectral slab-

selective pulses designed with OC. In general, there is no "maximum" design time for a tailored RF pulse to be feasible for in vivo scanning. Rather, it should be as short as possible. However, it is a reasonable assertion to say that the shortest spectral-spatial pulse design time (8 minutes 33 seconds in the phantom experiment) is still far too long. Therefore, substantial improvements in pulse design computation time should be made to make spectral-spatial slab-selective pulses viable.

Perhaps one reason why the spectral-spatial slab-selective pulses did not outperform their spectral counterparts (as was expected from [Chapter 4],[9]) could be a the selection of a suboptimal k-space trajectory. We chose spokes trajectories as the class of explored trajectories based on some inuition of spectral and slab-selective pulses. Due to the noted computation cost of spectral-spatial slab-selective pulses, it was challenging to test many other excitation trajectory designs. As was emphasized in Chapters 5 and 6, a joint design of the gradient waveform could be a major benefit for spectral-spatial slab-selective design (and for prewinding pulses with a spatial component in general.)

Spectral-spatial slab-selective pulses combine efforts of Chapters 4 and 5 to create a prewinding pulse in 4D. These pulses showed modest performance games but faced increased technical challenges in terms of design choices such as excitation trjaectory as well as computation expense. Further investigation could determine the clinical feasibility of this pulse design.

APPENDIX D

How-to Guide and Practical Considerations for RF Pulse Design Experiments

This appendix provides a brief guide for conducting RF pulse design experiments in the University of Michigan fMRI Lab on either of the two 3T GE Scanners. It also points to specific code that provides interested users the ability to reproduce the work from this dissertation.

In general all RF pulse design work was conducted in MATLAB (The Mathworks, Inc., MA R2016a). Furthermore, pulse sequence "programming" was done in the TOPPE platform [88] and image reconstruction and analysis was also done with MATLAB. Comparing some other common RF pulse programming groups (such as King's College London, Graz Institute of Medical Engineering, Vanderbilt University, and Stanford University), we find that MATLAB is the dominant programming language for RF pulse design, although other languages might be appropriate should the user have strong inclinations.

D.1 Using TOPPE

After designing an RF pulse waveform, the TOPPE platform can be used to playout the pulse in any desired pulse sequence. It is advisable to review the TOPPE user manual variable at the platform site https://toppemri.github.io/ maintained by Dr. Jon-Fredrik Nielsen for thorough details on TOPPE usage. All TOPPE MATLAB functions can be found there, as long with some working examples. In this section we will only give a brief overview.

First, the MATLAB-based RF and associated excitation gradient waveforms must be written to an interpretable form, a "`.mod`" file. This is done with the "`mat2mod.m`" MATLAB function. Additional waveforms for data acquisition (readout gradients) and any gradient crusher modules must all be generated with their own associated module. Next, a "`scanloop.txt`" file must be created that contains all lines of the pulse sequence

modules in the correct order with correct RF/gradient scalings for the desired sequence. These can be done through a loop-based MATLAB script, typically called something like "`write****loop.m`" where **** might be SPGR, STFR, or another sequence. Finally, a "`modules.txt`" file must contain a list of all relevant modules for one full TR of the pulse sequence to be scanned (e.g. "`tipdown.mod`","`readout.mod`","`tipup.mod`", "`spoiler.mod`" for STFR) along with any associated timing and data acquisition requirements for each module. To verify the design of a pulse sequence in TOPPE, the "`dispseq.m`" function can be used to plot a nominal number of TR's of the sequence. Some of the TOPPE files used for experiments in this thesis are found in my Github respository https://github.com/sydneynw/TOPPEforGEScanning.

D.2 Using the MRI Scanner

The current version of TOPPE is integrated into the DV26 GE software environment, although the bulk of this dissertation was conducted on DV25 or earlier versions. Nevertheless, we will describe the process of conducting experiments for the most recent software version.

After following the appropriate training safety protocol and setting up the scanner with desired coil, phantom or human volunteer, and isocenter localization, the user much choose an imaging protocol to begin scanning. I have created a generic protocol under "UM GE Research" $\rightarrow$ "Other" $\rightarrow$ "syd_toppev2" that can be used for a starting reference (shown in Figure D.1). Should the user want to create their own protocol, it is advisable to copy a 3D localizer scan from another GE research sequence such as my own. To load the TOPPE sequence, the user must select it from the "Imaging Options" button the lower left corner. After that, select "More", set the Plane to "Axial" the Mode "2D", the Family to "Gradient Echo", the Pulse to "GRE", and then type in the PSD Name below as "toppev2". Figure D.2 shows these selections. After pressing "Accept", the TOPPE PSD file shold be loaded unto the scanner (assuming the TOPPE `.e` file has already been compiled).

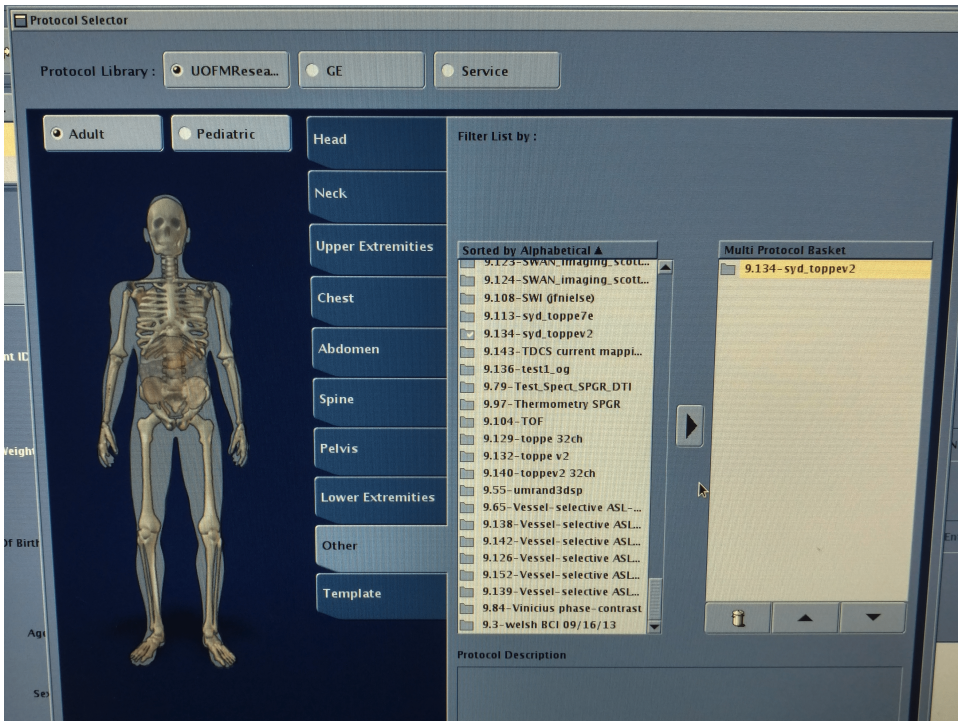

Figure D.1: The location of my TOPPE imaging protocol, which also includes a 3D localizer scan.

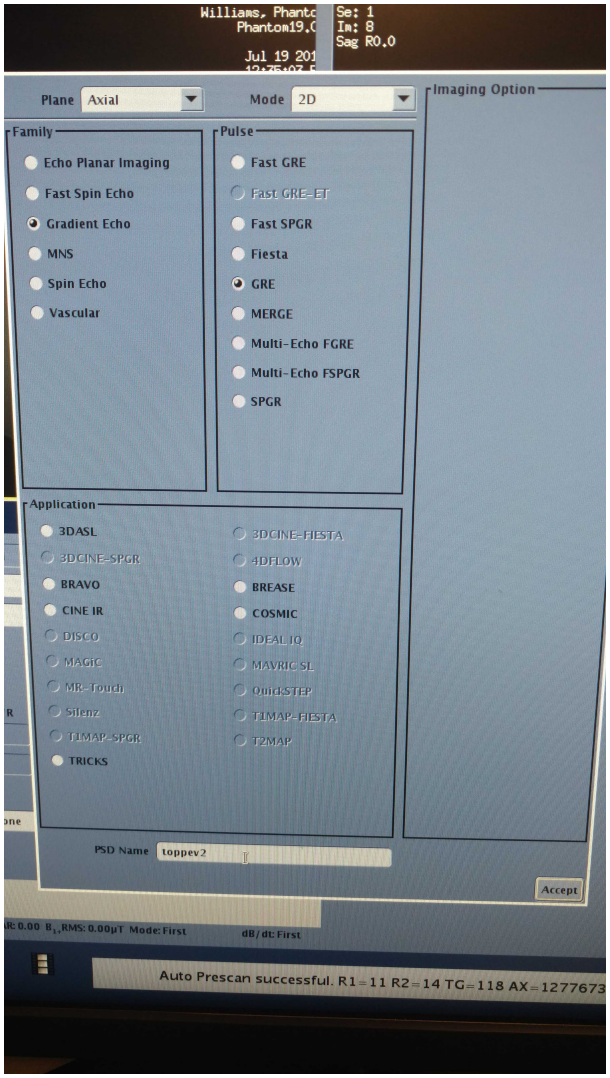

Figure D.2: Method for selecting the TOPPE sequence from the scanner if creating a new protocol.

After the required DV26 SAR Scout and 3D localizer scans, very little must be done with the user interface for the TOPPE sequence, as most of the scan settings are set based on the prescription listed in the "`scanloop.txt`". Typically, only a few dummy slices must be prescribed on the console and then the sequence can be saved. All TOPPE files ("`scanloop.txt`","`modules.txt`", and all necessary "`.mod`" files for the desired sequence) must be placed in the `/usr/g/bin` folder on the scanner. Next, the files must be downloaded by pressing the side arrow next to the "Scan" button and then the "Download" option. Figure D.3 shows a prescribed example of TOPPE on the scanner. After that, the "Manual Prescan" button must be opened and, if desired, the receive gain can be slightly reduced to reduce over-saturation of the analog-to-digital converter which causes data clip-

ping. Regardless of any changes, a manual prescan must be conducted for each new pulse sequence in order to prevent the scanner from running an auto prescan that could potentially change the RF calibration and be detrimental for comparing various TOPPE scans. After that, the "Scan" button can be pressed. Pending no errors within the TOPPE files, the sequence should run. Note, the sequence run time counter on the top right of the user interface will not display TOPPE pulse sequence durations, so the user must try to estimate their acquisition time based on their programmed sequence parameters (i.e., TR, number of phase encodes, etc.).

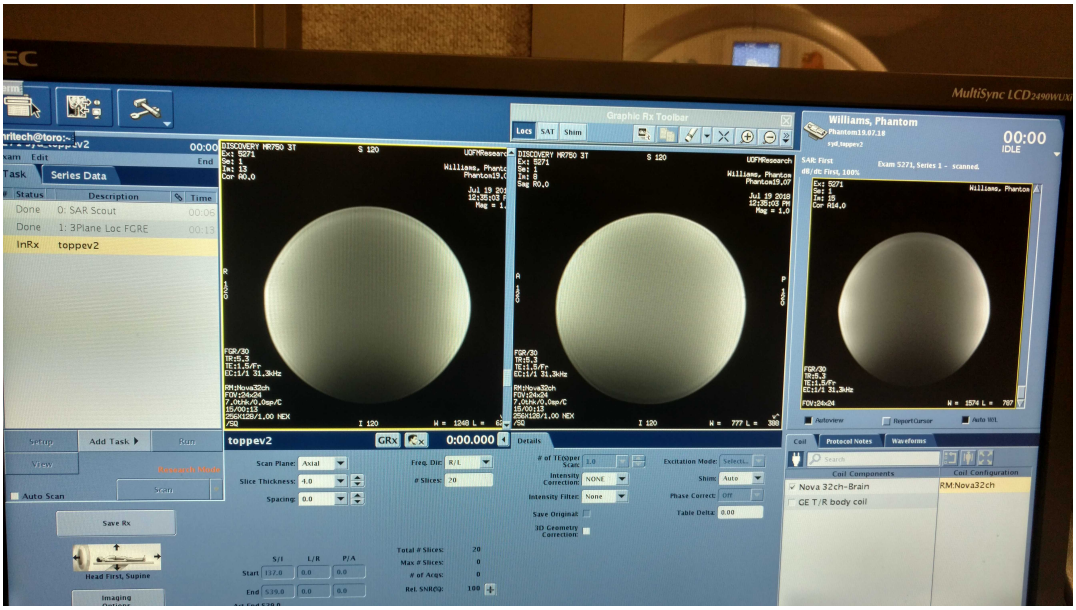

Figure D.3: Example of a saved TOPPE prescription on the scanner user interface.

During scanning, the user can roughly validate that the sequence plays out as intended by using the oscilloscope which has a G_x, G_y,G_z, and RF channel (Figure **??** shows example of an oscilloscope reading). By default, the RF channel is typically set to show the magnitude, but the user can change that channel to display phase by changing the RF switch in the back control room of the scanner (ask current lab member about this). "Scoping out" the pulse sequence will provide real-time information to the user if there are major issues with the pulse sequence but RF/gradient delays or gradient imperfections could be missed and should be validated in separate experiments.

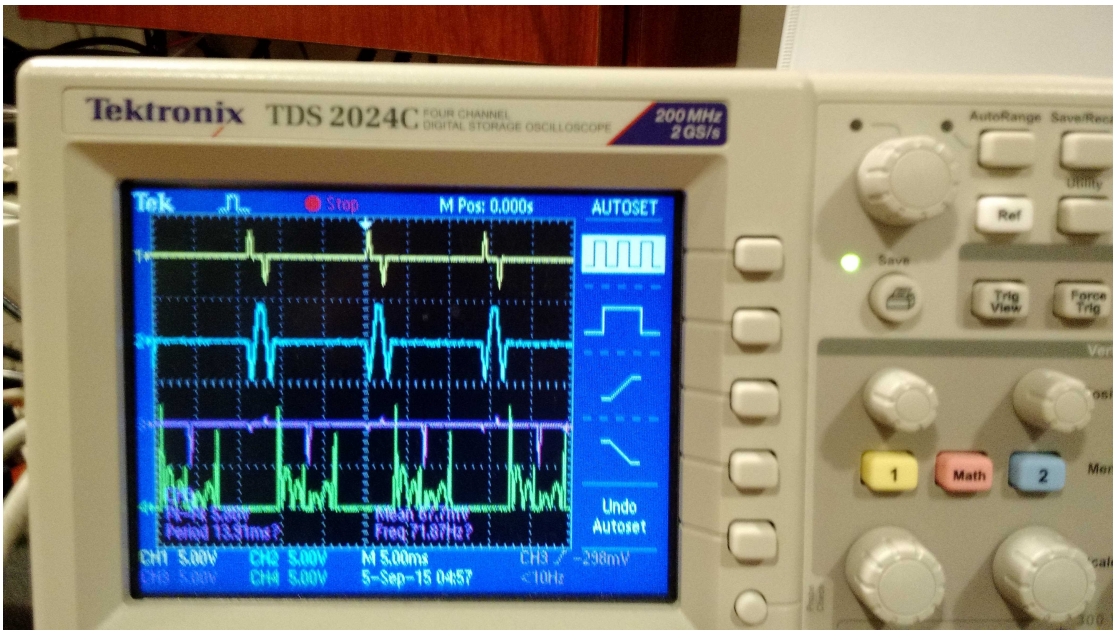

Figure D.4: Reading of the scanner oscilloscope with a spectral STFR pulse sequence playing out. The top yellow channel is G_x, cyan chanel is G_y, purple channel is G_z, and the bottom lime channel is RF magnitude.

To design and generate custom RF pulse module files online, the user can also open MATLAB from a remote machine on the scanner cancel. This requires the user to ssh into the desired machine using the "-Y" command. Sometimes there can be problems with ssh-keys or Xauthority permissions, but a typical safe account to log into is "`fmrilab@romero`".

D.3 Exporting/Reconstructing/Analyzing Data

After scanning, a so-called "P-file" (of the form P*****.7) will be generated in the `/usr/g/mrraw` directory for each acquisition. These P-files can then be copied over to the user's local lab machine, in my case "`affleck.engin.umich.edu`". With the exception of field map generation, all of my image reconstruction was typically done offline after the fact.

To reconstruct an image from P-file data, I generated a script "`recon_syd.m`" that was inspired by Jon-Fredrik Nielsen's recon code. This reconstruction produced complex multichannel images, the combined sum-of-squares image, and the raw k-space data. For complex coil combination of images, the reference scans from multichannel and body coil images were used to estimate the sensitivity maps with Dr. Jeff Fessler's "`ir_mri_coil_combine.m`" routine [31]. Sensitivity map estimation was done on a

slice-by-slice basis, although faster methods might be possible for 3D sensitivity map generation using works methods involving ADMM [92]. Logical support masks of the object were done with magnitude image thresholding and a few built-in MATLAB morphological operations ("`imclose.m`" and "`imerode.m`"). Field maps were estimated in 3D with Funai's regularized method [73]. When acquring multichannel data, the sensitivity map estimation and image reconstruction can be quite expensive for the average fMRI lab machine. Therefore, a lot of these processes were pushed to Dr. Fessler's `ire` servers, which need permission to access. It might also be possible to utilize fMRI lab servers in off-hours, but only after conversation with Dr. Scott Peltier and Krisanne Litinas.

Additional image analysis was done to evaluate pulse performance, as discussed in the Body Chapters of this dissertation. This included a 4D Bloch simulation in x,y,z,f, computing a few NRMSE and RMSE performance metrics, and estimating an inherent and linear object phase, to name a few. A variety of these functions can be found in my Github respository: https://github.com/sydneynw/MRIAnalysis.

D.4 Github and Online Software

As alluded to above, my personal Github (https://github.com/sydneynw/) has a variety of code available for reproducing my work. All simulations, and analysis, and figures from Chapter 4 [9] can be replicated from the "SpectralSpatial" repository. However, code for Chapter 3 [13],[14] and Chapter 5 [17] is not posted because journal publication for these works is still pending. To access this work for internal UM use, I have put some relevant code on `fmrilab@romero:~/sydney/Code/SMS` and `fmrilab@romero:~/sydney/Code/SpectralSlab`.

A lot of this work would not be possible without the help of software contributed from others. I am very grateful for the open-source, sharing environment of the RF pulse design research community. The following works were especially used in this dissertation and often required for a majority of my scripts and functions:

- Dr. Jeff Fessler's Michigan Image Reconstruction Toolbox [31]
  http://web.eecs.umich.edu/~fessler/code/index.html
- Dr. John Pauly's RF Tools for SLR Pulses [24]
  http://rsl.stanford.edu/download/pauly/
- Drs. Michael Grant and Steven Boyd's CVX software
  http://cvxr.com/cvx/download/

- Dr. Brian Hargreaves variable density spiral [93], VERSE [68]
  http://mrsrl.stanford.edu/∼brian/mritools.html
- Dr. Hao Sun's C-based Bloch Simulator (adapted from Dr. Brian Hargreaves)
  http://www-personal.umich.edu/∼sunhao/
- Dr. Jon-Fredrik Nielsen's reconstruction code and TOPPE [88]
  https://toppemri.github.io/
- Dr. Will Grissom's OC perturbation updates for LTA designs [28], [26]
  www.vuiis.vanderbilt.edu/∼grissowa/optimalcontrol.zip
- ... and potentially many others!

If interested users have any challenges using or following my code, or if there are any bugs or missing files, I am happy to help sort these issues out and will be responsive via emaill: `sydneynw_at_umich_dot_edu`.

BIBLIOGRAPHY

[1] Yip, C., Fessler, J. A., and Noll, D. C., "Iterative RF pulse design for multidimensional, small-tip-angle selective excitation," *Mag. Res. Med.*, Vol. 54, No. 4, Oct. 2005, pp. 908–17.

[2] Yip, C., Fessler, J. A., and Noll, D. C., "Advanced three-dimensional tailored RF pulse for signal recovery in T_2^*-weighted functional magnetic resonance imaging," *Mag. Res. Med.*, Vol. 56, No. 5, Nov. 2006, pp. 1050–9.

[3] Yip, C.-Y., Lee, S., Grissom, W., Fessler, J. A., and Noll, D. C., "Spectral-spatial pulse design for signal recovery in T2*-weighted BOLD functional MRI," *Proc. Intl. Soc. Mag. Res. Med.*, 2008, p. 2453.

[4] Yip, C., Yoon, D., Olafsson, V., Lee, S., Grissom, W. A., Fessler, J. A., and Noll, D. C., "Spectral-spatial pulse design for through-plane phase precompensatory slice selection in T2*-weighted functional MRI," *Mag. Res. Med.*, Vol. 61, No. 5, May 2009, pp. 1137–47.

[5] Yoon, D., Fessler, J. A., Gilbert, A. C., and Noll, D. C., "Fast joint design method for parallel excitation RF pulse and gradient waveforms considering off-resonance," *Mag. Res. Med.*, Vol. 68, No. 1, July 2012, pp. 278–85.

[6] Nielsen, J.-F., Yoon, D., and Noll, D. C., "Small-tip fast recovery imaging using non-slice-selective tailored tip-up pulses and radiofrequency-spoiling," *Mag. Res. Med.*, Vol. 69, No. 3, March 2013, pp. 657–66.

[7] Sun, H., Fessler, J. A., Noll, D. C., and Nielsen, J.-F., "Joint design of excitation k-space trajectory and RF pulse for small-tip 3D tailored excitation in MRI," *IEEE Trans. Med. Imag.*, Vol. 35, No. 2, Feb. 2016, pp. 468–79.

[8] Sun, H., Fessler, J. A., Noll, D. C., and Nielsen, J.-F., "Rapid inner-volume imaging in the steady-state with 3D selective excitation and small-tip fast recovery (STFR) imaging," *Mag. Res. Med.*, Vol. 76, No. 4, Oct. 2016, pp. 1217–23.

[9] Williams, S. N., Nielsen, J.-F., Fessler, J. A., and Noll, D. C., "Design of spectral-spatial phase prewinding pulses and their use in small-tip fast recovery steady-state imaging," *Mag. Res. Med.*, Vol. 79, No. 3, March 2018, pp. 1377–86.

[10] Srinivasan, S. and Ennis, D. B., "Variable flip angle balanced steady-state free precession for lower SAR or higher contrast cardiac cine imaging," *Mag. Res. Med.*, Vol. 71, No. 3, March 2014, pp. 1035–43.

[11] Herborn, C., Vogt, F., Lauenstein, T. C., Goyen, M., Debatin, J. F., and Ruehm, S. G., "MRI of the liver: can true FISP replace HASTE?" *J Magn Reson Imaging*, Vol. 17, 2003, pp. 190–196.

[12] Jou, T., Patterson, S., Pauly, J. M., and Bowen, C. V., "Fat-suppressed alternating-SSFP for whole-brain fMRI using breath-hold and visual stimulus paradigms," *Mag. Res. Med.*, Vol. 75, No. 5, 2016, pp. 1978–88.

[13] Williams, S. N., Noll, D. C., and Fessler, J. A., "Improved simultaneous multislice pulse design directly constraining peak RF amplitude," *Proc. Intl. Soc. Mag. Res. Med.*, April 2017, p. 3854.

[14] Williams, S. N., Fessler, J. A., and Noll, D. C., "Minimum out-of-slice error SMS RF pules design with direct peak, power, and in-slice error constraints," *Proc. Eur. Soc. Mag. Res. Med. B*, October, 2017, p. 681.

[15] Assländer, J., Glaser, S. J., and Hennig, J., "Spin echoes in the regime of weak dephasing," *Mag. Res. Med.*, Vol. 75, No. 1, Jan. 2016, pp. 150–60.

[16] Williams, S. N., Sun, H., Nielsen, J.-F., Fessler, J. A., and Noll, D. C., "A spectral-spatial pulse for improved inhomogeneity signal loss in the small-tip fast recovery (STFR) sequence," *Proc. Intl. Soc. Mag. Res. Med.*, 2015, p. 919.

[17] Williams, S. N., Nielsen, J.-F., Fessler, J. A., and Noll, D. C., "Slab-selective spectral and spectral-spatial prewinding RF pulses," *Proc. Intl. Soc. Mag. Res. Med.*, June 2018.

[18] Nishimura, D. G., "Principles of magnetic resonance imaging," 1996, Unpublished textbook.

[19] Finlay, C. C., Maus, S., Beggan, C. D., Bondar, T. N., Chambodut, A., Chernova, T. A., Chulliat, A., and et al., V. P. G., "International geomagnetic reference field: the eleventh generation," *Geophysical J. International*, Vol. 183, No. 3, December 2010, pp. 1216–1230.

[20] Bloch, F., "Nuclear induction," *Phys. Rev.*, Vol. 70, No. 7-8, Oct. 1946, pp. 460–74.

[21] Bernstein, M. A., King, K. F., and Zhou, X. J., *Handbook of MRI pulse sequences*, Elsevier, 2004.

[22] Pauly, J., Nishimura, D., and Macovski, A., "A k-space analysis of small-tip-angle excitation," *J. Mag. Res.*, Vol. 81, No. 1, Jan. 1989, pp. 43–56.

[23] Börnert, P. and Aldefeld, B., "On spatially selective RF excitation and its analogy with spiral MR image acquisition," *Mag. Res. Mat. in Phys. Bio. Med.*, Vol. 7, No. 166-178, 1998.

[24] Pauly, J., Le Roux, P., Nishimura, D., and Macovski, A., "Parameter relations for the Shinnar-Le Roux selective excitation pulse design algorithm," *IEEE Trans. Med. Imag.*, Vol. 10, No. 1, March 1991, pp. 53–65.

[25] Goldstein, H., *Classical Mechanics*, Vol. 4-5, chap. The Cayley-Klein parameters and related quantities, Addison-Wesley, Reading, MA, 2nd ed., 1980, pp. 148–158.

[26] Cao, Z., Donahue, M. J., Ma, J., and Grissom, W. A., "Joint design of large-tip-angle parallel RF pulses and blipped gradient trajectories," *Mag. Res. Med.*, Vol. 75, No. 3, March 2016, pp. 1198–208.

[27] Conolly, S., Nishimura, D., and Macovski, A., "Optimal control solutions to the magnetic resonance selective excitation problem," *IEEE Trans. Med. Imag.*, Vol. 5, No. 2, June 1986, pp. 106–15.

[28] Grissom, W. A., Xu, D., Kerr, A. B., Fessler, J. A., and Noll, D. C., "Fast large-tip-angle multidimensional and parallel RF pulse design in MRI," *IEEE Trans. Med. Imag.*, Vol. 28, No. 10, Oct. 2009, pp. 1548–59.

[29] Fessler, J. A., *Image reconstruction: Algorithms and analysis*, ., 2006, Book in preparation.

[30] Sutton, B. P., Noll, D. C., and Fessler, J. A., "Fast, iterative image reconstruction for MRI in the presence of field inhomogeneities," *IEEE Trans. Med. Imag.*, Vol. 22, No. 2, Feb. 2003, pp. 178–88.

[31] Fessler, J. A., "Michigan image reconstruction toolbox (MIRT) for Matlab," 2016, Available from http://web.eecs.umich.edu/∼fessler/.

[32] Beck, A. and Teboulle, M., "A fast iterative shrinkage-thresholding algorithm for linear inverse problems," *SIAM J. Imaging Sci.*, Vol. 2, No. 1, 2009, pp. 183–202.

[33] Saad, Y., *Numerical methods for large eigenvalue problems*, Soc. Indust. Appl. Math., 2nd ed., 2011.

[34] Bauschke, H., Goebel, R., Lucet, Y., and Wang, X., "The proximal average: basic theory," *SIAM J. Optim.*, Vol. 19, No. 2, 2008, pp. 766–85.

[35] Grant, M. and Boyd, S., "CVX: Matlab software for disciplined convex programming, version 2.1," March 2014.

[36] Boyd, S., Parikh, N., Chu, E., Peleato, B., and Eckstein, J., "Distributed optimization and statistical learning via the alternating direction method of multipliers," *Found. & Trends in Machine Learning*, Vol. 3, No. 1, 2010, pp. 1–122.

[37] Scheffler, K., "A pictorial description of steady-states in rapid magnetic resonance imaging," *Concepts in Magnetic Resonance*, Vol. 11, No. 5, 1999, pp. 291–304.

[38] Sun, H., Fessler, J. A., Noll, D. C., and Nielsen, J.-F., "Strategies for improved small-tip fast recovery (STFR) imaging," *Proc. Intl. Soc. Mag. Res. Med.*, 2013, p. 2362, ISMRM Magna Cum Laude award.

[39] Sun, H., Fessler, J. A., Noll, D. C., and Nielsen, J.-F., "Steady-state functional MRI using spoiled small-tip fast recovery (STFR) imaging," *Mag. Res. Med.*, Vol. 73, No. 2, Feb. 2015, pp. 536–43.

[40] Malik, S. J. and Hajnal, J. V., "Phase relaxed localized excitation pulses for inner volume fast spin echo imaging," *Mag. Res. Med.*, Vol. 76, 2016, pp. 848–861.

[41] Davids, M., Schad, L. R., Wald, L. L., and Güerin, B., "Fast three-dimensional inner volume excitations using parallel transmission and optimized k-space trajectories," *Mag. Res. Med.*, Vol. 76, No. 4, Oct. 2016, pp. 1170–82.

[42] Barth, M., Breuer, F., Koopmans, P. J., Norris, D. G., and Poser, B. A., "Simultaneous multislice (SMS) imaging techniques," *Mag. Res. Med.*, Vol. 75, No. 1, Jan. 2016, pp. 63–81.

[43] Müller, S., "Multifrequency selective RF pulses for multislice MR imaging," *Mag. Res. Med.*, Vol. 6, 1988, pp. 364–371.

[44] Wong, E., "Optimized phase schedules for minimizing peak RF power in simultaneous multi-slice RF excitation pulses," *Proc. Intl. Soc. Mag. Res. Med.*, 2012, p. 2209.

[45] Sharma, A., Lustig, M., and Grissom, W. A., "Root-flipped multiband refocusing pulses," *Mag. Res. Med.*, Vol. 75, No. 1, Jan. 2016, pp. 227–37.

[46] Aigner, C. S., Clason, C., Rund, A., and Stollberger, R., "Efficient high-resolution RF pulse design applied to simultaneous multi-slice excitation," *J. Mag. Res.*, Vol. 263, 2016, pp. 33–44.

[47] Norris, D. G., Koopmans, P. J., Boyacioglu, R., and Barth, M., "Power independent of number of slices (PINS) radiofrequency pulses for low-power simultaneous multislice excitation," *Mag. Res. Med.*, Vol. 66, No. 5, Nov. 2011, pp. 1234–40.

[48] Rund, A., Aigner, C. S., Kunisch, K., and Stollberger, R., "Magnetic resonance RF pulse design by optimal control with physical constraints," *IEEE Trans. Med. Imag.*, Vol. 37, No. 2, February 2018, pp. 461–472.

[49] Todd Constable, R. and Spencer, D. D., "Repetition time in echo planar functional MRI," *Mag. Res. Med.*, Vol. 46, 2001, pp. 748–755.

[50] Friedman, L. and Glover, G. H., "Report on a multicenter fMRI quality assurance protocol," *J. Mag. Res. Im.*, Vol. 23, No. 6, June 2006, pp. 827–39.

[51] Setsompop, K., Wald, L. L., Alagappan, V., Gagoski, B. A., and Adalsteinsson, E., "Magnitude least squares optimization for parallel radio frequency excitation design demonstrated at 7 Tesla with eight channels," *Mag. Res. Med.*, Vol. 59, No. 4, April 2008, pp. 908–15.

[52] Breuer, F. A., Blaimer, M., Heidemann, R. M., Mueller, M. F., Griswold, M. A., and Jakob, P. M., "Controlled aliasing in parallel imaging results in higher acceleration (CAIPIRINHA) for multi-slice imaging," *Mag. Res. Med.*, Vol. 53, No. 3, March 2005, pp. 684–91.

[53] Setsompop, K., Gagoski, B. A., Polimeni, J. R., Witzel, T., Wedeen, V. J., and Wald, L. L., "Blipped-controlled aliasing in parallel imaging for simultaneous multislice echo planar imaging with reduced g-factor penalty," *Mag. Res. Med.*, Vol. 67, No. 5, May 2012, pp. 1210–24.

[54] Hargreaves, B., "Rapid Gradient-Echo Imaging," *J Magn Reson Imaging*, Vol. 36, No. 6, December 2012, pp. 1300–1313.

[55] Sun, H., Fessler, J. A., Noll, D. C., and Nielsen, J.-F., "Balanced SSFP-like steady-state imaging using small-tip fast recovery sequence with a spectral pre-winding pulse," *Mag. Res. Med.*, Vol. 75, No. 2, Feb. 2016, pp. 839–44.

[56] Sun, H., Fessler, J. A., Noll, D. C., and Nielsen, J.-F., "Strategies for improved 3D small-tip fast recovery (STFR) imaging," *Mag. Res. Med.*, Vol. 72, No. 2, Aug. 2014, pp. 389–98.

[57] Bieri, O. and Scheffler, K., "SSFP signal with finite RF pulses," *Mag. Res. Med.*, Vol. 62, No. 5, Nov. 2009, pp. 1232–41.

[58] Çukur, T., Shimakawa, A., Yu, H., Hargreaves, B. A., Hu, B. S., Nishimura, D. G., and Brittain, J. H., "Magnetization-Prepared IDEAL bSSFP: A Flow-Independent Technique for Nonctrast-Enhanced Periperhal Angiography," *J Magn Reson Imaging*, Vol. 33, No. 2, April 2011, pp. 931–939.

[59] Fessler, J. A. and Sutton, B. P., "Nonuniform fast Fourier transforms using min-max interpolation," *IEEE Trans. Sig. Proc.*, Vol. 51, No. 2, Feb. 2003, pp. 560–74.

[60] Allison, M. J. and Fessler, J. A., "Accelerated computation of regularized field map estimates," *Proc. Intl. Soc. Mag. Res. Med.*, 2012, p. 0413.

[61] Mulkern, R. V., Balasubramanian, M., and Mitsouras, D., "On the Lorentzian versus Gaussian character of time-domain spin-echo signals from the brain as sampled by means of gradient-echoes: Implications for quantitative transverse relaxation studies," *Mag. Res. Med.*, Vol. 74, No. 1, July 2015, pp. 51–62.

[62] Olafsson, V. T., Noll, D. C., and Fessler, J. A., "Fast joint reconstruction of dynamic R_2^* and field maps in functional MRI," *IEEE Trans. Med. Imag.*, Vol. 27, No. 9, Sept. 2008, pp. 1177–88.

[63] Dahnke, H. and Schaeffter, T., "Limits of detection of SPIO at 3.0 T using T2* relaxometry," *Mag. Res. Med.*, Vol. 53, 2005, pp. 1202–1206.

[64] Saekho, S., Yip, C., Noll, D. C., Boada, F. E., and Andrew Stenger, V., "Fast-k_z three-dimensional tailored radiofrequency pulse for reduced B_1 inhomogeneity," *Mag. Res. Med.*, Vol. 55, No. 4, April 2006, pp. 719–24.

[65] Zelinski, A. C., Wald, L. L., Setsompop, K., Goyal, V. K., and Adalsteinsson, E., "Sparsity-enforced slice-selective MRI RF excitation pulse design," *IEEE Trans. Med. Imag.*, Vol. 27, No. 9, Sept. 2008, pp. 1213–29.

[66] Harkins, K. D., Does, M. D., and Grissom, W. A., "Iterative method for predistortion of MRI gradient waveforms," *IEEE Trans. Med. Imag.*, Vol. 33, No. 8, Aug. 2014, pp. 1641–7.

[67] Duyn, J. H., Yang, Y., Frank, J. A., and van der Veen, J. W., "Simple correction method for k-space trajectory deviations in MRI," *J. Mag. Res.*, Vol. 132, No. 1, May 1998, pp. 150–3.

[68] Hargreaves, B. A., Cunningham, C. H., Nishimura, D. G., and Conolly, S. M., "Variable-rate selective excitation for rapid MRI sequences," *Mag. Res. Med.*, Vol. 52, No. 3, Sept. 2004, pp. 590–7.

[69] Saekho, S., Boada, F. E., Noll, D. C., and Stenger, V. A., "Small tip angle three-dimensional tailored radiofrequency slab-select pulse for reduced B_1 inhomogeneity at 3 T," *Mag. Res. Med.*, Vol. 53, No. 2, Feb. 2005, pp. 479–84.

[70] Setsompop, K., Alagappan, V., Gagoski, B. A., Potthast, A., Hebrank, F., Fontius, U., Schmitt, F., Wald, L. L., and Adalsteinsson, E., "Broadband slab selection with B1+ mitigation at 7T via parallel spectral-spatial excitation," *Mag. Res. Med.*, Vol. 61, No. 2, Feb. 2009, pp. 493–500.

[71] Zhao, F., Nielsen, J.-F., Swanson, S. D., Fessler, J. A., and Noll, D. C., "Simultaneous fat saturation and magnetization transfer contrast imaging with steady-state incoherent sequences," *Mag. Res. Med.*, Vol. 74, No. 3, Sept. 2015, pp. 739–46.

[72] Conolly, S., Nishimura, D., Macovski, A., and Glover, G. H., "Variable-rate selective excitation," *J. Mag. Res.*, Vol. 78, No. 3, July 1988, pp. 440–58.

[73] Funai, A. K., Fessler, J. A., Yeo, D. T. B., Olafsson, V. T., and Noll, D. C., "Regularized field map estimation in MRI," *IEEE Trans. Med. Imag.*, Vol. 27, No. 10, Oct. 2008, pp. 1484–94.

[74] Kim, Y., Fessler, J. A., and Noll, D. C., "Smoothing effect of sensitivity map on fMRI data using a novel regularized self-calibrated estimation method," *Proc. Intl. Soc. Mag. Res. Med.*, 2008, p. 1267.

[75] Wansapura, J. P., Holland, S. K., Dunn, R. S., and Ball, W. S., "NMR relaxation times in the human brain at 3.0 Tesla," *J. Mag. Res.*, Vol. 9, No. 4, April 1999, pp. 531–8.

[76] Roemer, P. B., Edelstein, W. A., Hayes, C. E., Souza, S. P., and Mueller, O. M., "The NMR phased array," *Mag. Res. Med.*, Vol. 16, No. 2, Nov. 1990, pp. 192–225.

[77] Pruessmann, K. P., Weiger, M., Scheidegger, M. B., and Boesiger, P., "SENSE: sensitivity encoding for fast MRI," *Mag. Res. Med.*, Vol. 42, No. 5, Nov. 1999, pp. 952–62.

[78] Bley, T. A., Wieben, O., , C. J., Brittain, J. H., and Reeder, S. B., "Fat and water magnetic resonance imaging," *J. Mag. Res. Im.*, Vol. 31, No. 1, Jan. 2010, pp. 4–18.

[79] Zhao, F., Swanson, S. D., Nielsen, J.-F., Fessler, J. A., and Noll, D. C., "Simultaneous fat saturation and magnetization transfer preparation with 2D small-tip fast recovery imaging," *Proc. Intl. Soc. Mag. Res. Med.*, 2013, p. 2507.

[80] Aigner, C. S., Rund, A., Seada, S. A., Malik, S., Hajnal, J. V., Kunisch, K., and Stollberger, R., "Time-optimal control based RF pulse design under gradient imperfections," *Proc. Intl. Soc. Mag. Res. Med.*, June 2018.

[81] Addy, N. O., Wu, H. H., and Nishimura, D. G., "Simple method of MR gradient system characterization and k-space estimation," *Mag. Res. Med.*, Vol. 68, No. 1, 2012, pp. 120–129.

[82] Zhu, Y., "Parallel excitation with an array of transmit coils," *Mag. Res. Med.*, Vol. 51, No. 4, April 2004, pp. 775–84.

[83] Hoyos-Idrobo, A., Weiss, P., Massire, A., Amadon, A., and Boulant, N., "On variant strategies to solve the magnitude least squares optimization problem in parallel transmission pulse design and under strict SAR and power constraints," *IEEE Trans. Med. Imag.*, Vol. 33, No. 3, March 2014, pp. 739–48.

[84] Güerin, B., Gebhardt, M., Cauley, S., Adalsteinsson, E., and Wald, L. L., "Local specific absorption rate (SAR), global SAR, transmitter power, and excitation accuracy trade-offs in low flip-angle parallel transmit pulse design," *Mag. Res. Med.*, Vol. 71, No. 4, April 2014, pp. 1446–57.

[85] Güerin, B., Setsompop, K., Ye, H., Poser, B. A., Stenger, A. V., and Wald, L. L., "Design of parallel transmission pulses for simultaneous multislice with explicit control for peak power and local specific absorption rate," *Mag. Res. Med.*, Vol. 73, No. 5, May 2015, pp. 1946–53.

[86] Cloos, M. A., Boulant, N., Luong, M., Ferrand, G., Giacomini, E., Le Bihan, D., and Amadon, A., "kT-points: Short three-dimensional tailored RF pulses for flip-angle homogenization over an extended volume," *Mag. Res. Med.*, Vol. 67, No. 1, Jan. 2012, pp. 72–80.

[87] Boulant, N., Massire, A., Amadon, A., and Vignaud, A., "Radiofrequency pulse design in parallel transmission under strict temperature constraints," *Mag. Res. Med.*, Vol. 72, No. 3, Sept. 2014, pp. 679–88.

[88] Nielsen, J.-F. and Noll, D. C., "TOPPE: A framework for rapid prototyping of MR pulse sequences," *Mag. Res. Med.*, 2018.

[89] Gras, V., Vignaud, A., Amadon, A., Bihan, D. L., and Boulant, N., "Universal pulses: A new concept for calibration-free parallel transmission," *Mag. Res. Med.*, Vol. 77, No. 2, Feb. 2017, pp. 635–43.

[90] Shao, T., Xia, L., Tao, G., Chi, J., Liu, F., and Crozier, S., "Advanced three-dimensional tailored RF pulse design in volume selective parallel excitation," *IEEE Trans. Med. Imag.*, Vol. 31, No. 5, 2012, pp. 997–1007.

[91] Malik, S. J., Keihaninejad, S., Hammers, A., and Hajnal, J. V., "Tailored excitation in 3D with spiral nonselective (SPINS) RF pulses," *Mag. Res. Med.*, Vol. 67, No. 5, 2012, pp. 1303–15.

[92] Allison, M. J., Ramani, S., and Fessler, J. A., "Accelerated regularized estimation of MR coil sensitivities using augmented Lagrangian methods," *IEEE Trans. Med. Imag.*, Vol. 32, No. 3, March 2013, pp. 556–64.

[93] Meyer, C. H., Hu, B. S., Nishimura, D. G., and Macovski, A., "Fast spiral coronary artery imaging," *Mag. Res. Med.*, Vol. 28, No. 2, Dec. 1992, pp. 202–13.